

**INTERFACIAL RHEOLOGY AND THE CONTROLLED FABRICATION  
AND DISRUPTION OF STABILIZED EMULSIONS**

by

**Jerome Jamal Nash**

**A Dissertation**

*Submitted to the Faculty of Purdue University*

*In Partial Fulfillment of the Requirements for the degree of*

**Doctor of Philosophy**



School of Materials Engineering

West Lafayette, Indiana

May 2019

**THE PURDUE UNIVERSITY GRADUATE SCHOOL  
STATEMENT OF COMMITTEE APPROVAL**

Dr. Kendra A. Erk, Chair

School of Materials Engineering

Dr. John A. Howarter

School of Materials Engineering

Dr. Carlos J. Martinez

School of Materials Engineering

Dr. Elliott B. Slamovich

School of Materials Engineering

**Approved by:**

Dr. David F. Bahr

Head of the Graduate Program

*To Tonya Renee*

## ACKNOWLEDGMENTS

I am indebted to my adviser, Kendra A. Erk. She graciously introduced me to many opportunities that allowed me to expand my skills as a scientist. She pushed me into areas which were initially intimidating and encouraged me through both my successes and my failures. Prof. Erk permitted me to set my own goals, which enabled me to become a self-reliant researcher early in my graduate career. It was through Prof. Erk's adaptability and flexibility that my creativity and critical thinking were allowed to flourish. I am also deeply grateful for each of the interactions that I shared with past and present members of the Erk group, as well as with members of the Soft-Materials Core Research Labs. The collaborative environment established by this community of scientists was vital to my sense of belonging during the early years of my graduate career.

Additionally, I would like to thank the members of my thesis committee, Professors John A. Howarter, Carlos J. Martinez, and Elliott B. Slamovich. Every interaction we shared improved my understanding of fundamental materials science concepts and regularly illuminated compelling research paths. Moreover, these individuals instructed three undergraduate courses which were monumental in developing my passion for materials science. Prof. Slamovich was my instructor for MSE 23000: Structure and Properties of Materials, which introduced me to structure-property-processing-performance relationships that facilitate appropriate materials selection. Prof. Howarter was my teacher for MSE 33500: Materials Characterization Laboratory, where the principles of various analytical methods for the characterization of materials were presented in a lucid and hands-on manner. Lastly, Prof. Martinez was my instructor for MSE 597: Introduction to Soft Materials, where the structure and properties of soft materials, as well as how to characterize these physical properties, were presented. This course was instrumental in my decision to conduct research on soft materials during my PhD.

Furthermore, I would like to thank each of the mentors that I collected during my time at Purdue University. Specifically, I would like to acknowledge Dr. Logan Kearney, Dr. Lisa Nielsen, Dr. Veronica Rodriguez Martinez, Dr. Anna Walter, Dr. Lisa Rueschhoff, Prof. David Bahr, Prof. Rodney Trice, Prof. Jeffrey Youngblood, and Dr. Kai Gao for their helpful conversations which often served as vital affirmations that obtaining my PhD was, indeed, possible. I was also extremely fortunate to meet several highly talented mentors outside of my home institution including Prof. Patrick Spicer, Dr. Jeffrey Martin, Dr. Vincent Poulichet, and Mr. Seth Lindberg. These individuals expertly demonstrated how to merge creative ideation with high quality research.

I am also deeply indebted to the faculty, staff, and alumni of the School of Materials Engineering at Purdue University. Both my fondness for materials science and my development as a researcher largely stem from the support that I received from those within this community. Over the course of my undergraduate and graduate career at Purdue University, the School of Materials Engineering grew to become my family. Words cannot adequately express the depth of my appreciation for this group of Boilermakers.

I am also indebted to the countless others who have supported me along my path – teachers, family, and friends. Additionally, I am deeply grateful to my companion, Breanne Wright, who has kept me motivated to succeed each day and who has encouraged me when I needed it most. I look forward to what the future holds for us. Lastly, above all, I owe everything that I've achieved to the unending love and support of my mother, Tonya Renee Turner. She fought significant odds to ensure that I received a good education in an environment that presented considerable barriers to this noble aim. She gave me strength at times when I felt defeated, and her words of encouragement remain unparalleled.

## TABLE OF CONTENTS

LIST OF TABLES .....	9
LIST OF FIGURES .....	10
ABSTRACT .....	18
CHAPTER 1 INTRODUCTION .....	20
1.1 Interfacial Rheology.....	20
1.2 Deformation and Mechanics of Immiscible Fluid Interfaces .....	22
1.2.1 Static Pendant Drop Tensiometry .....	25
1.2.2 Oscillating Pendant Drop Tensiometry .....	25
1.3 Viscoelastic Behavior of Single- and Multi-Component Liquid Interfaces .....	26
1.3.1 Low Molecular Weight Surfactants.....	27
1.3.2 Surface-Active Particles .....	29
1.3.3 Connecting Interfacial Mechanics to the Stability of Emulsions and Foams .....	31
1.4 Mechanisms of Emulsion Destabilization and Their Characterization.....	32
1.4.1 Gravitational Phase Separation.....	32
1.4.2 Droplet Flocculation and Coalescence .....	33
1.5 Particle Size Characterization .....	34
1.6 Particle Surface Charge Characterization .....	35
1.7 References.....	37
CHAPTER 2 STABILITY AND INTERFACIAL VISCOELASTICITY OF OIL-WATER NANOEMULSIONS STABILIZED BY SOY LECITHIN AND TWEEN 20 FOR THE ENCAPSULATION OF BIOACTIVE CARVACROL .....	44
2.1 Introduction.....	44
2.2 Experimental Methods .....	47
2.2.1 Materials and Reagents.....	47
2.2.2 Determination of Minimum Nanoemulsion Surfactant Concentration .....	47
2.2.3 Nanoemulsion Preparation.....	51
2.2.4 Nanoemulsion Droplet Size Measurements.....	52
2.3 Results and Discussion .....	52

2.3.1	Effect of Oil Phase Composition and Surfactant Concentration on Initial Nanoemulsion Stability .....	52
2.3.2	Effect of Surfactant Concentration on Interfacial Viscoelasticity .....	55
2.3.3	Effect of pH on Interfacial Viscoelasticity .....	57
2.3.4	Correlation Between Dilatational Viscoelasticity and Nanoemulsion Stability .....	62
2.4	Summary .....	68
2.5	References .....	70
<b>CHAPTER 3 ADSORPTION, DILATATIONAL RHEOLOGY, AND EMULSION STABILIZATION OF SiO<sub>2</sub>-DPPC COMPLEXES AT THE OIL-WATER INTERFACE .....</b>		
<b>74</b>		
3.1	Introduction .....	74
3.2	Experimental Methods .....	77
3.2.1	Materials and Reagents .....	77
3.2.2	Preparation of Aqueous Dispersions and Bulk Oil-in-Water Emulsions .....	78
3.2.3	Phase Separation Stability and Morphology Characterization .....	79
3.3	Results and Discussion .....	80
3.3.1	Effect of Bare SiO <sub>2</sub> on Oil-Water Interfacial Properties .....	80
3.3.2	Effect of DPPC Alone on Oil-Water Interfacial Properties .....	81
3.3.3	Physical Association of DPPC and SiO <sub>2</sub> in Water .....	84
3.3.4	Interfacial Rheology of Mixed SiO <sub>2</sub> -DPPC Systems .....	89
3.3.5	Bulk Emulsion Stability and Morphology .....	91
3.4	Summary .....	101
3.5	References .....	103
<b>CHAPTER 4 GRAVITATIONAL PHASE SEPARATION OF OIL-IN-WATER EMULSIONS BY SiO<sub>2</sub> NANOPARTICLE-INDUCED FLOCCULATION .....</b>		
<b>107</b>		
4.1	Introduction .....	107
4.2	Experimental Methods .....	110
4.2.1	Materials .....	110
4.2.2	Preparation of Model Oil-in-Water Bilge Emulsions .....	113
4.2.3	Preparation of Aqueous SiO <sub>2</sub> Nanoparticle Suspensions .....	115
4.2.4	Emulsion Stability Characterization .....	116
4.3	Results and Discussion .....	117

4.3.1	Emulsion Destabilization – Effect of Vortex Mixing and Order of Addition .....	117
4.3.2	Morphology of Flocculated Oil Droplets .....	120
4.3.3	Light Scattering Analysis of Droplet-Depleted Aqueous Regions.....	123
4.4	Summary .....	126
4.5	References.....	128
<b>CHAPTER 5 CONTROLLABLE INTERNAL MIXING BETWEEN COALESCING</b>		
<b>DROPLETS INDUCED BY THE SOLUTAL MARANGONI CONVECTION OF</b>		
<b>SURFACTANTS WITH DISTINCT HEADGROUP ARCHITECTURES .....</b>		
		<b>132</b>
5.1	Introduction.....	132
5.2	Materials and Experimental Methods .....	136
5.2.1	Materials .....	136
5.2.2	Visualizing Rapid Binary Drop Coalescence .....	136
5.2.3	Determination of Interfacial Adsorptive Properties at the Oil-Water Interface .....	138
5.2.4	Determination of Surfactant-Induced Interfacial Spreading Velocity, $U_s$ .....	141
5.3	Results and Discussion .....	144
5.3.1	Effect of Surfactant Type on Bridge Expansion and Internal Mixing.....	144
5.3.2	Influence of Surfactant Type on the Development of Bulk Fluid Jetting.....	148
5.3.3	Comparison of ALS and CTAB Adsorption at the Oil-Water Interface .....	152
5.3.4	Surfactant Interfacial Spreading Under an Induced Concentration Gradient .....	154
5.4	Summary .....	156
5.5	References.....	159
<b>CHAPTER 6 CONCLUSIONS.....</b>		
		<b>163</b>
6.1	Summary of Projects.....	163
6.2	Future Work and Outlook .....	164
<b>VITA.....</b>		
		<b>166</b>

## LIST OF TABLES

- Table 2-1** Z-Ave oil droplet diameters collected on Day 1 and Day 30 for lecithin and Tween 20 nanoemulsions at pH 7 and 3. Each system had a dispersed oil phase that contained 10 wt.% carvacrol in MCT oil (0.05 wt.% carvacrol overall). Data are reported for nanoemulsions with lecithin or Tween 20 concentrations less than and greater than  $C_a$ . Values are reported as averages  $\pm$  1 standard deviation ( $n > 3$ ). ..... 61
- Table 2-2** Zeta ( $\zeta$ ) potential measurements collected on Day 1 and Day 30 for lecithin and Tween 20 nanoemulsions at pH 7 and 3. Each system had a dispersed oil phase that contained 10 wt.% carvacrol in MCT oil (0.05 wt.% carvacrol overall). Data are reported for nanoemulsions with lecithin or Tween 20 concentrations less than and greater than  $C_a$ . Values are reported as averages  $\pm$  1 standard deviation ( $n > 3$ ). ..... 65
- Table 3-1** Average hydrodynamic diameters of particles/agglomerates in aqueous mixtures containing 2.5 wt.% SiO<sub>2</sub> and various DPPC concentrations. Measurements were taken within 48 hours of sample preparation..... 88
- Table 5-1** Surface excess concentrations and minimum molecular areas calculated for ALS and CTAB at 23 °C at the triglyceride oil-water interface..... 141

## LIST OF FIGURES

- Figure 1-1** Various deformation modes of an interfacial element. Adapted from Danov et al.<sup>10</sup>  
 ..... 20
- Figure 1-2** Illustrations of experimental interfacial rheometric devices including the (a) biconical disk geometry, (b) pendant drop apparatus, and (c) the Langmuir-Blodgett trough with Wilhelmy plate.<sup>29</sup> ..... 24
- Figure 1-3** Illustration of the history dependent linear viscoelasticity of dipalmitoylphosphatidylcholine (DPPC) at the air-water interface analyzed with a Ferromagnetic ‘microbutton’ probe. Note the relative magnitudes of  $G'$  and  $G''$  in (a) and (c), as well as the transition from  $G' > G''$  to  $G'' > G'$  upon yielding. The micrographs in (b) and (d) illustrate the formation of a shear plane, given by the arrow (scale bar, 20  $\mu\text{m}$ ).<sup>41</sup> ..... 28
- Figure 1-4** (a) Elastic (closed) and viscous (open) shear moduli at  $1 \text{ rad s}^{-1}$  for 3  $\mu\text{m}$  polystyrene particles at 79% coverage at an air-water interface with 0.4 M NaCl (circles), 0.004 M NaCl (diamonds), and 0 M NaCl (squares). (b) corresponding micrographs for these systems at 0.002% and 20% interfacial strain.<sup>46,47</sup> ..... 31
- Figure 2-1** Interfacial tension isotherms for (a) 0.35 wt.% lecithin stabilized interfaces and (b) 1 wt.% Tween 20 stabilized interfaces. The aqueous continuous phase contained the surfactant and citrate-phosphate buffer at pH 7. The oil droplet phase contained 10 wt.% carvacrol in MCT oil..... 49
- Figure 2-2** Interfacial tension as a function of bulk surfactant concentration ( $\text{mol L}^{-1}$ ) for lecithin (blue/circles) and Tween 20 (green/triangles). Error bars represent  $\pm 1$  standard deviation. Surfactants were dispersed in a pH 7 citrate-phosphate buffer solution and the oil phase consisted of 10% (v/v) carvacrol in MCT oil. The lines are best fits of the Gibbs adsorption isotherm. .... 50

- Figure 2-3** Photographs taken 24 h after emulsification for oil-in-water nanoemulsions at pH 7 stabilized by (a) 0.25 wt.% Tween 20, (b) 1 wt.% Tween 20, (c) 0.25 wt.% lecithin or (d) 0.25 wt.% lecithin. Each emulsion contains 5 wt.% dispersed oil phase, with increasing amounts of carvacrol in MCT oil from left to right (0 (control), 5, 10, 20, 40, 60, 80 wt.% carvacrol). ..... 53
- Figure 2-4** Evolution of the viscoelastic moduli,  $E'$  and  $E''$ , over 24 h for 0.25 wt.% Lecithin and 0.25 wt.% Tween 20 stabilized O/W interfaces at (a) pH 7 and (b) pH 3. The aqueous phase contained the emulsifier, while the oil phase had a composition of 10 wt.% carvacrol in MCT oil. Oscillations were conducted at a frequency of 0.01 Hz. Lines simply connect data points to aid the eye. .... 56
- Figure 2-5** Evolution of the viscoelastic moduli,  $E'$  and  $E''$ , over 24 h for 0.35 wt.% Lecithin and 1 wt.% Tween 20 stabilized O/W interfaces at (a) pH 7 and (b) pH 3. The aqueous phase contained the emulsifier, while the oil phase had a composition of 10 wt.% carvacrol in MCT oil. Oscillations were conducted at a frequency of 0.01 Hz. Lines simply connect data points to aid the eye. .... 56
- Figure 2-6** Intensity size distributions over 30 days for oil-in-water emulsions that contained 5 wt.% oil (10 wt.% carvacrol in MCT oil) stabilized by (a) 0.25 wt.% Tween 20, (b) 1 wt.% Tween 20, (c) 0.25 wt.% lecithin or (d) 0.35 wt.% lecithin at pH 7. Data were offset from zero to illustrate size distribution changes over time. .... 63
- Figure 2-7** Intensity size distributions over 30 days for oil-in-water emulsions that contained 5 wt.% oil (10 wt.% carvacrol in MCT oil) stabilized by (a) 0.25 wt.% Tween 20, (b) 1 wt.% Tween 20, (c) 0.25 wt.% lecithin or (d) 0.35 wt.% lecithin at pH 3. Data were offset from zero to illustrate size distribution changes over time. .... 64
- Figure 2-8** Visualization of the % change in droplet Z-Ave diameter over 30 days for Tween 20 and lecithin stabilized nanoemulsions at surfactant concentrations (a) below and (b) above their corresponding  $C_a$  values. The oil phase made up 5 wt.% of the total nanoemulsion (10 wt.% carvacrol in MCT oil). Lines simply connect data points to aid the eye. .... 66

- Figure 3-1** Chemical structure of 1,2-dipalmitoyl-sn-glycero-3-phosphocholine, or DPPC. .... 77
- Figure 3-2** Equilibrium interfacial tensions versus DPPC concentration for oil-water interfaces containing DPPC alone and DPPC in the presence of a fixed SiO<sub>2</sub> concentration (2.5 wt.%). Measurements were obtained 1.5 hours after interface formation. The solid line represents the best fit of the Langmuir adsorption isotherm..... 82
- Figure 3-3** Dilatational storage and loss moduli for oil-water interfaces laden with various concentrations of DPPC alone. Measurements were taken following an interface equilibration period of 1.5 hours. Solid lines are aids for the eye. .... 83
- Figure 3-4** Calculations of DPPC molecule-to-SiO<sub>2</sub> nanoparticle ratio plotted as a function of bulk DPPC concentration. These data assume complete, irreversible adsorption of DPPC molecules onto the available surfaces of SiO<sub>2</sub> in the bulk aqueous phase..... 85
- Figure 3-5** Influence of bulk DPPC concentration on the average zeta potential of SiO<sub>2</sub> nanoparticles in an aqueous suspension at pH 7, as quantified by dynamic light scattering measurements at 25 °C. Each aqueous dispersion contained 2.5 wt.% SiO<sub>2</sub> nanoparticles and measurements were taken within 48 hours of sample preparation. Error bars represent  $\pm 1$  standard deviation. .... 87
- Figure 3-6** Dilatational storage and loss moduli for oil-water interfaces laden with DPPC-SiO<sub>2</sub> nanoparticle complexes as a function of deformation frequency. Data are shown for increasing concentrations of DPPC in the presence of a fixed SiO<sub>2</sub> nanoparticle concentration (2.5 wt.%). Measurements were taken following an interface equilibration period of 1.5 hours. Solid lines are aids for the eye. .... 90
- Figure 3-7** Bulk oil-water mixtures containing initial concentrations of bare SiO<sub>2</sub> nanoparticles ranging from 0.05-20 wt.% in the aqueous phase. This image was taken after emulsification and the 24-hour equilibration period. The transparent upper fluid in each system was the less-dense oil-rich layer and the turbid lower layer fluid is the water-rich SiO<sub>2</sub> nanoparticle suspension. No middle emulsified layer was formed in any of these mixtures. .... 91

**Figure 3-8** Oil-water mixtures containing initial concentrations of DPPC ranging from 0.01–1 mM in the aqueous phase. The image was taken after emulsification and the 24-hour equilibration period. The translucent upper fluid in each system was the less-dense oil-rich layer and the turbid lower layer was comprised of the water-rich DPPC dispersions. An emulsified layer was formed only in mixtures containing  $\geq 0.5$  mM DPPC. The dashed (red) arrow indicates the location of a semi-stable emulsified layer and solid (green) arrow indicates a stable emulsified layer. .... 92

**Figure 3-9** (a) Gravitational phase separation analysis of bulk oil-water mixtures containing a fixed 2.5 wt.% SiO<sub>2</sub> concentration and a varying concentration of DPPC in the aqueous phase. This image was taken after the 24-hour equilibration period following initial emulsification. Dashed (red) arrows indicate the location of semi-stable emulsified layers and solid (green) arrows indicate stable emulsified layers. (b) Separation Index (SI) values for the lower, water-rich layer (closed circles) and the upper, oil-rich layer in each oil-water mixture. Lower SI values correspond to greater stability to phase separation and coalescence. .... 94

**Figure 3-10** Optical micrographs of the emulsified layers sampled from bulk emulsions obtained after the 24-hour equilibration period. These images correspond to bulk emulsions that contained a fixed 2.5 wt.% SiO<sub>2</sub> concentration and 0.2 mM DPPC (a-1, a-2), 0.5 mM DPPC (b-1, b-2), and 1 mM DPPC (c-1, c-2) in the aqueous dispersion prior to emulsification. Each emulsion was oil-in-water, as determined by dilution measurements. The scale bar in each image is 100  $\mu$ m. .... 96

**Figure 3-11** (a) Gravitational phase separation analysis of bulk oil-water mixtures containing a fixed DPPC concentration (0.1 mM) and a varying SiO<sub>2</sub> concentration (0.5-20 wt.%). This image was taken after the 24-hour equilibration period following initial emulsification. Dashed (red) arrows indicate the location of semi-stable emulsified layers and solid (green) arrows indicate stable emulsified layers. (b) Separation Index (SI) values for the lower, water-rich layer (closed circles) and the upper, oil-rich layer in each oil-water mixture. Lower SI values correspond to greater stability to phase separation and coalescence. .... 98

- Figure 3-12** Optical micrographs of the emulsified layers sampled from bulk emulsions obtained after the 24-hour equilibration period. These images correspond to bulk emulsions that contained a fixed 0.1 mM DPPC concentration and 2.5 wt.% SiO<sub>2</sub> (a-1, a-2), 10 wt.% SiO<sub>2</sub> (b-1, b-2), or 20 wt.% SiO<sub>2</sub> (c-1, c-2) in the aqueous dispersion prior to emulsification. Each emulsion was oil-in-water, as determined by dilution measurements. The scale bar in each image is 100 μm. .... 100
- Figure 4-1** Particle size distribution for a 1 wt.% Ludox CL nanoparticle aqueous suspension at pH 7.1, as determined by dynamic light scattering measurements using a Malvern Zetasizer Nano ZS instrument. The corresponding ζ potential for the nanoparticles in this suspension was measured to be + 26.5 ± 2.1 mV. .... 112
- Figure 4-2** Photograph of the neat model emulsion partitioned into scintillation vials, 24 hours after initial emulsification. The emulsion in each of these vials comprises 25,000 ppm of dispersed oil and 2500 ppm SLES surfactant in deionized water. .... 113
- Figure 4-3** (a) Particle size distribution, as determined by dynamic light scattering measurements using a Malvern Zetasizer Nano ZS instrument, and (b) corresponding micrograph of the neat, oil-in-water model emulsion. The emulsion used in each analysis comprised ~12,500 ppm of dispersed oil. .... 114
- Figure 4-4** Photographs of bulk oil-in-water emulsions following dilution with positively charged SiO<sub>2</sub> nanoparticles for a final nanoparticle concentration of 0, 0.1, 0.2, 0.5, 0.75, 1, or 2 wt.% SiO<sub>2</sub>. The images illustrate systems which were not vortex mixed (a and c) and those that were vortex mixed (b and d) for 30 seconds at 2500 rpm immediately following dilution. Destabilization behavior is shown for the mixtures after a 30-minute (a and b) and 24-hour (c and d) equilibration interval. The opaque regions in each mixture illustrate flocculated, oil-rich regions and the translucent/slightly turbid regions correspond to the droplet-depleted, water-rich regions of the mixture. .... 117
- Figure 4-5** Photographs of bulk oil-in-water emulsions following dilution, where positively charged SiO<sub>2</sub> nanoparticles were added to the neat model emulsion (a and c) or vice-

versa (b and d). Each of these mixtures was vortex mixed for 30 seconds at 2500 rpm immediately following dilution. The final SiO<sub>2</sub> concentrations in each set of experiments was 0, 0.1, 0.2, 0.5, 0.75, 1, or 2 wt.% SiO<sub>2</sub>. Destabilization behavior is shown for the mixtures after a 30-minute (a and b) and 24-hour (c and d) equilibration interval. The opaque regions in each mixture illustrate flocculated, oil-rich regions and the translucent/slightly turbid regions correspond to the droplet-depleted, water-rich regions of the mixture. .... 119

**Figure 4-6** Optical micrographs of aggregates formed within nanoparticle-emulsion mixtures with aqueous SiO<sub>2</sub> nanoparticle concentrations of 0.1 (a), 1 (b), and 2 wt.% (c) SiO<sub>2</sub> nanoparticles. Images were taken following the addition of SiO<sub>2</sub> nanoparticles to the neat emulsion, subsequent vortex mixing for 30 seconds at 2500 rpm, and a 24-hour equilibration period. Red circles highlight small and medium-sized aggregates. .... 121

**Figure 4-7** Particle size distributions for the droplet-depleted, water-rich regions of nanoparticle-emulsion mixtures that contained (a) 0.2, (b) 0.75, and (c) 2 wt.% SiO<sub>2</sub>. Size distributions are shown for three mixing procedures: (1) where aqueous SiO<sub>2</sub> suspensions were added to the emulsion, followed by vortex mixing (black squares), (2) where the model emulsion was added to aqueous SiO<sub>2</sub> suspensions, followed by vortex mixing (red circles), and (3) where aqueous SiO<sub>2</sub> suspensions were added to the emulsion, but were not subjected to vortex mixing (blue triangles). .... 124

**Figure 5-1** An illustration of the experimental setup used to study coalescence between binary aqueous droplets in a surrounding oil. The leftmost aqueous droplet was laden with surfactant and the rightmost droplet was surfactant-free, yet contained a small concentration of dye to aid in flow visualization. .... 137

**Figure 5-2** Interfacial tension,  $\gamma$ , versus log of surfactant concentration,  $c$ , in aqueous solution at 23 °C at the triglyceride oil-water interface measured by the drop shape analysis technique. Lines represent best-fitting straight lines of the data in the low and high surfactant concentration regimes for each surfactant. The slope value of the best-fitting line in the low surfactant concentration regime was used in the determination of the surface excess concentration,  $\Gamma_m$ , for ALS and CTAB. .... 140

**Figure 5-3** Schematic representation of the experimental setup used to quantify interfacial spreading velocities,  $U_s$ , under an induced interfacial tension gradient at the triglyceride oil-water interface. A side view depicting the introduction of a surfactant loaded water droplet at the surfactant-free, oil-water interface (containing tracer particles) is shown in (a) and an illustration of the surfactant diffusion mechanism, quantified by measuring the rate of displacement for tracer particles attached to the interface, is shown in (b)... 142

**Figure 5-4** Kinetics of expansion for the connective bridge separating spherical droplets with an equivalent initial diameter,  $2R$  ( $= 2$  mm). The data represent the increase in the connective bridge diameter,  $D_b$ , relative to  $2R$ , as a function of the square-root-of-time,  $t^{1/2}$ , succeeding the onset of droplet coalescence. .... 145

**Figure 5-5** Temporal shape profiles of equally sized water droplets coalescing in triglyceride oil. The leftmost droplet in each image contained either (a) no surfactant, (b)  $2.5 \times 10^{-3}$  mol L<sup>-1</sup> ALS, or (c)  $2.5 \times 10^{-3}$  mol L<sup>-1</sup> CTAB, while the rightmost droplet in each image was surfactant-free, with dye added for flow visualization. The absence or presence of opposing flows at the interface and within the bulk of the merging droplets illustrate the effect of interfacially adsorbed surfactant molecules. Differences in the curvature of the jetted fluid following coalescence in (b) and (c) demonstrate the influence of surfactant headgroup architecture on the relative magnitude of these induced flows. The scale bars in each image are 0.5 mm in length. .... 147

**Figure 5-6** Flow profiles depicting the formation of fluid jets of different sizes for asymmetrically sized water droplets coalescing in triglyceride oil. The leftmost droplet in each image contained either (a) no surfactant, (b)  $2.5 \times 10^{-3}$  mol L<sup>-1</sup> ALS, or (c)  $2.5 \times 10^{-3}$  mol L<sup>-1</sup> CTAB, while the rightmost droplet in each image was surfactant-free, with dye added for flow visualization. The scale bars in each image are 0.5 mm in length..... 149

**Figure 5-7** Displacement of the jetted fluid apex,  $\Delta S_{jet}$ , originating from the surfactant-free droplet into the surfactant-laden droplet as a function of time,  $t$ , succeeding droplet contact for asymmetrically sized droplet systems. Micrograph insets depict the position

of the fluid jets 17.2 ms after the onset of coalescence. The scale bars in each image are 0.5 mm in length. .... 151

**Figure 5-8** Seeded tracer particle displacement,  $\Delta_{\text{particle}}$ , versus time,  $t$ , following the introduction of a  $2.5 \times 10^{-3} \text{ mol L}^{-1}$  aqueous droplet solution of anionic ALS or cationic CTAB surfactant at a planar triglyceride oil-water interface. Motion of the interfacially seeded tracer particles resulted directly from the induced surfactant concentration gradient of either ALS or CTAB. Data are shown for fully developed particle displacement rates, 6.5 milliseconds after initial contact between the surfactant-laden drop and the planar oil water interface. .... 154

## ABSTRACT

Author: Nash, Jerome, J. PhD

Institution: Purdue University

Degree Received: May 2019

Title: Interfacial Rheology and the Controlled Fabrication and Disruption of Stabilized Emulsions

Committee Chair: Kendra A. Erk

Fluid interfaces stabilized by surface-active species (e.g., surfactants, polymers, and particles) have rheological properties that are vital to the kinetic stability of emulsions. Many practical applications of emulsions necessitate superb stability during storage, such as in emulsion-based therapeutic delivery systems. While in other cases, stabilized systems are entirely unwanted (e.g., separating oil and aqueous phases in enhanced oil recovery and bilge water applications). Techniques for modulating emulsion phase separation processes are highly desired and are largely determined by the mechanics of interfacially trapped species which preserve the overall stability of bulk emulsions. However, the utility of these techniques is often limited by difficulties in measuring and interpreting the rheological properties of complex fluid interfaces. Lack of control over interface formation during emulsification magnifies this problem, further obscuring relationships between interfacial rheology and bulk emulsion stability. Therefore, the objectives of this thesis were to (1) elucidate fundamental relationships between the mechanics of complex fluid interfaces and the anticipated stability of the bulk emulsions they comprise through interfacial rheological measurements, and (2) present innovative methodologies for modulating the kinetic stability of model oil-in-water emulsions using physical chemistry principles.

The introductory chapter of this thesis will provide a detailed overview of contemporary experimental tools used to probe the rheology of single- and multi-component complex fluid interfaces. Additionally, this chapter will include a discussion on the role of interfacial rheology

in an emulsion's susceptibility to the key destabilization mechanisms that dominate its performance (e.g., coalescence, flocculation, and gravitational phase separation).

The second and third chapters of this thesis focus on experimental methods that can be utilized to characterize an oil-in-water emulsion's stability to droplet coalescence based on the interfacial adsorption and dilatational rheological characteristics of the stabilizing emulsifiers. In Chapter 2, a criterion for inhibiting the susceptibility to droplet coalescence of dilute oil-in-water emulsions based on the rheological properties of the surfactant-stabilized interfaces is presented. Chapter 3 details how droplet coalescence in concentrated oil-in-water emulsions can be inhibited by the interfacial steric hinderance of SiO<sub>2</sub>-surfactant complexes.

The fourth and fifth chapters of this work focus on how physical chemistry principles can be used to control emulsion droplet destabilization and produce desirable physical outcomes within bulk emulsions. Chapter 4 details an investigation of how the gravitational phase separation of dilute, electrostatically stabilized oil-in-water emulsions can be induced by a complex coacervation mechanism. Here, attractive electrostatic interactions between the interface-stabilizing anionic surfactant sodium lauryl ether sulfate (SLES) and positively charged silicon dioxide (SiO<sub>2</sub>) nanoparticles can be used to encourage droplet flocculation in model oil-in-water emulsions. Chapter 5 outlines an innovative methodology for encouraging tightly controlled internal mixing between coalescing water droplets via interfacial rheological methods. The methods established in this study have direct application in the development of micro-droplet reactors, which necessitate controlled mixing in microliter volumes.

The knowledge garnered from this body of work is highly relevant to academic and industrial emulsion formulators who seek inexpensive, yet robust methods for predicting, characterizing and tailoring the extended kinetic stability of oil-in-water emulsions.

## CHAPTER 1 INTRODUCTION

### 1.1 Interfacial Rheology

Soft materials with high surface area-to-volume ratios are ubiquitous both in nature and technological applications. Easily recognized examples of such systems include food emulsions and foams,<sup>1,2</sup> lipid vesicles,<sup>3,4</sup> lung alveoli,<sup>5</sup> polymersomes<sup>6</sup> and core-shell microcapsules.<sup>7-9</sup> The dominating presence of interfaces within such soft colloids suggests that interfacial mechanics are non-negligible to the overall physical behavior of the bulk. This is because each of these systems experience one or more complex interfacial deformation modes (e.g., shear, dilatation, bending, or extensional (Figure 1-1)<sup>10</sup>) either during the formation, stabilization, or degradation of the bulk material.

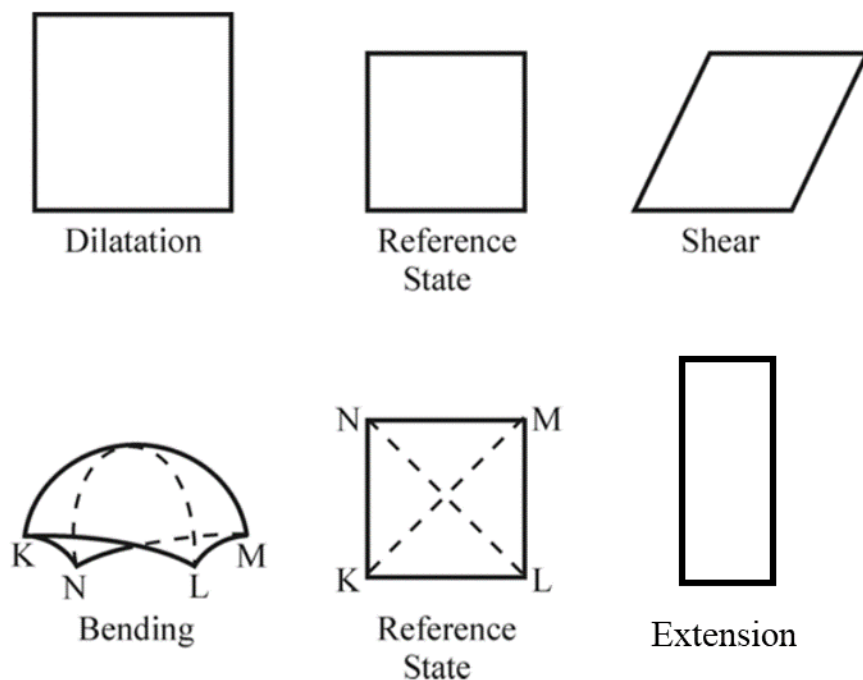


**Figure 1-1** Various deformation modes of an interfacial element. Adapted from Danov et al.<sup>10</sup>

While the interfaces between pure and simple fluids can be wholly characterized by their equilibrium interfacial tension,  $\gamma$ , compound interfaces laden with surface-active species (such as low molecular weight surfactants, particles, synthetic- or bio-macromolecules) routinely exhibit nonlinear viscoelastic behavior in response to complex deformation modes. As such, interfacial tension alone is no longer a comprehensive descriptor of the behavior observed within these compound interfacial layers. Interfacial rheology probes the fluid motion and deformation of vapor-liquid (e.g., air-water) and liquid-liquid (e.g., oil-water) interfaces in the presence of amphiphilic species.<sup>11,12</sup> In many instances, mass and momentum transfer in two dimensions can be considered analogous to transport problems in three-dimensional bulk systems.<sup>11,13,14</sup> Two important factors distinguish these two categories: (1) interfacial and bulk flows are coupled because mass and momentum can be transported between the interface and the surrounding bulk fluids, (2) interfacial monolayers are highly compressible, and thus the rate-dependent dilatational properties of interfaces are considerably more consequential to the developed flows in two dimensions than those in three dimensions.<sup>11</sup>

Interfacial rheology is routinely studied within the context of the kinematics of the applied deformation mode, i.e., through dilatational, shear, or extensional rheometry. Dilatational measurements invoke uniform area compressions and/or expansions of an interfacial element, while conserving its shape,<sup>15</sup> whereas shear and extensional rheometry experiments utilize shearing and extensional interfacial deformations, respectively, at constant area.<sup>16</sup> It is often presumed in the scientific literature that dilatational deformations are expected to be important in the kinetic stabilization of foams and emulsions,<sup>17,18</sup> while shear and extensional interfacial deformations are vital to the formation processes of complex fluids.<sup>19,20</sup>

Interfacial shear and dilatational studies of complex fluid interfaces appear to have dominated the recent literature due to the ease of probing well-defined mass and momentum transport modes at liquid interfaces with widely available rheometric tools. However, two key issues remain toward fully understanding the relevance of interfacial rheology in practical systems. The first is that many of the available interfacial rheometry tools struggle to quantify the mechanical properties of complex interfaces resulting from isolated deformation modes, as the imposed flows often contain both shear and dilatational components.<sup>21,22</sup> The second issue is that direct translation of the properties obtained from interfacial rheological measurements to the anticipated mechanical behavior of bulk complex fluid systems is non-trivial and dependent upon specific physiochemical characteristics of the system. Thus, this thesis seeks to provide a critical review of best practices in experimental interfacial rheology, as well as insight on the possible contributions of interfacial rheology in the practical applications of oil-in-water emulsions.

## 1.2 Deformation and Mechanics of Immiscible Fluid Interfaces

The rate of deformation directly impacts the stress that develops within an immiscible fluid interface. An interfacial stress tensor  $\mathbf{T}_s$  and deformation rate tensor  $\mathbf{D}_s$  are more comprehensive descriptors of these properties as compared to a single interfacial tension value.<sup>23,24</sup> The total stress at a fluid interface, given by  $-\pi\mathbf{I}_s + \mathbf{T}_s$ , can be described as the sum of the isotropic portion of the surface stress  $\pi\mathbf{I}_s$  and the excess surface stress,  $\mathbf{T}_s$ . Here,  $\pi = \gamma_0 - \gamma$  represents the surface pressure, which is given by the difference between the interfacial tension of the pure fluids in the absence of adsorbed species,  $\gamma_0$ , and the equilibrium interfacial tension,  $\gamma$ . Experimentally,  $\mathbf{D}_s$  becomes a scalar quantity equivalent to the applied strain rate in rheometric measurements. In interfacial dilatational measurements, the strain ( $\Delta A/A_0$ ) is typically defined as the ratio of an incremental change in the interfacial area,  $\Delta A$ , to the initial interfacial area,  $A_0$ . Often, the strain is

modulated over time, and the dilatational strain rate is given by the time derivative of the applied strain,  $\frac{d}{dt} \left( \frac{\Delta A}{A_0} \right)$ . In interfacial shear measurements, the shear rate can be determined directly from angular velocity of a rotating geometry, as is the case when biconical disk and ring geometries are coupled with a conventional rheometer.

The generalized Boussinesq-Scriven surface stress tensor<sup>25,26</sup> for the surface of an arbitrary Newtonian fluid is given by  $\mathbf{T}_s = [(\kappa - \eta) \text{div}_s \mathbf{v}_s] \mathbf{Q} + 2\eta \mathbf{D}_s$ , where  $\kappa$  corresponds to the interfacial dilatational viscosity,  $\eta$  is the interfacial shear viscosity,  $\text{div}_s$  is the divergence operator, and  $\mathbf{Q}$  is a surface projection tensor which transforms each component into their corresponding component tangential to the fluid surface.<sup>24</sup> Complex notation is often used instead of  $\kappa$  and  $\eta$  to represent the complex shear and dilatational viscosities,  $\kappa^*$  and  $\eta^*$ , respectively. Also, most interfacial rheology studies in the literature instead use complex modulus notation to describe interfacial mechanics, where  $G^* = G' + iG''$  represents the complex shear modulus of the interface and  $E^* = E' + iE''$  corresponds to the complex dilatational modulus of the interface. Here, the magnitude of the elastic contributions to the complex moduli are given by the values of  $G'$  and  $E'$ , while the viscous contributions are given by  $G''$  and  $E''$ .

Generally, studies which investigate dilatational moduli utilize isotropic measurements of the dynamic interfacial tension, determined by a static force balance and fitting the shape profile of a hanging pendant drop to the Young-Laplace equation. With this technique, the quantities obtained therefore represent effective measurements of the dilatational moduli, rather than intrinsic moduli such as  $\kappa$  in the Boussinesq-Scriven surface stress tensor. However, this discrepancy is usually negligible and only becomes problematic when an interface is subjected to highly non-uniform deformation fields and interfacial shear rigidity dominates over dilatational rigidity.<sup>27</sup> While shear and dilatational are not the only modes of deformation at fluid interfaces (bending and

extension have been shown to significantly influence the behavior of lipid bilayers for example<sup>28</sup>), these two modes are the most relevant to droplet break-up and stabilization in most high surface area-to-volume, oil-water and gas-water systems.

Numerous techniques are available to probe the mechanics of interfacial monolayers. Several reviews have summarized the different apparatuses for measuring shear and dilatational interfacial deformations.<sup>29</sup> To study interfacial shear rheology, existing flow measurement systems can be used with specially designed geometries, as has been done with the biconical disk geometry (Figure 1-2a). To investigate interfacial dilatational rheology, most studies utilize either the pendant drop (Figure 1-2b) or Langmuir-Blodgett trough (Figure 1-2c) technique because of their ease of use and commercial availability. Additionally, microfluidic apparatuses have been developed to probe the dilatational deformation mechanics of complex interfaces.<sup>30</sup>

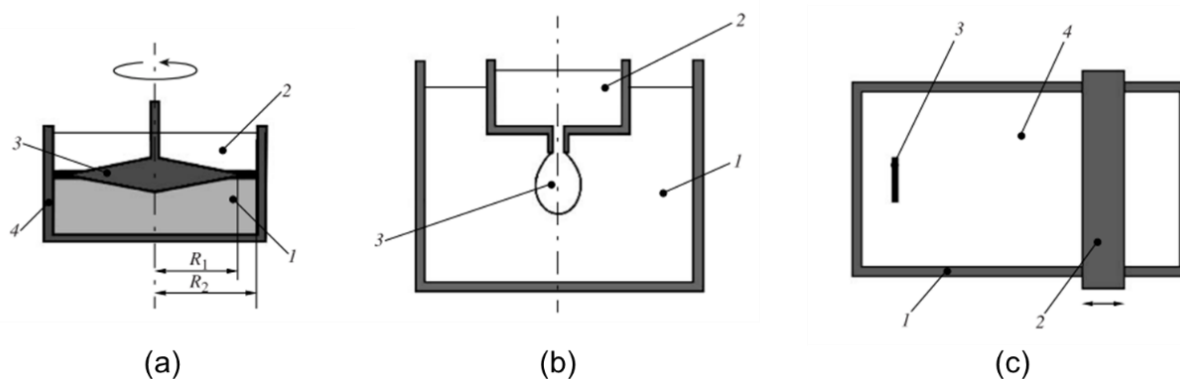


**Figure 1-2** Illustrations of experimental interfacial rheometric devices including the (a) biconical disk geometry, (b) pendant drop apparatus, and (c) the Langmuir-Blodgett trough with Wilhelmy plate.<sup>29</sup>

### 1.2.1 Static Pendant Drop Tensiometry

The pendant drop method was used for all interfacial tension and dilatational rheological measurements performed throughout this thesis. Extensive details on this experimental technique are provided in the literature.<sup>23–26</sup> In brief, the interfacial tension of an oil-water interface was determined by fitting the Young-Laplace equation, given by  $\gamma \left( \frac{1}{R_1} + \frac{1}{R_2} \right) = \Delta P$ , where  $R_1$  and  $R_2$  are the principle radii of curvature, and  $\Delta P$  is the Laplace pressure across the curved interface. For each of the pendant drop experiments performed in this thesis, this equation was fit to the profile of an axisymmetric oil droplet ( $V \approx 30 \mu\text{L}$  to  $32 \mu\text{L}$ ) formed at the tip of a 20-gauge stainless steel needle (0.584 mm i.d.). The oil droplet was immersed in 5 mL of the aqueous surfactant solution in a rectangular glass cuvette. The dimensionless shape factor,  $\beta$ , exceeded the minimum value ( $|\beta| > 0.1$ ) for accurate measurement of the interfacial tension for each system ( $|\beta| > 0.18$ ).<sup>27</sup> These measurements were performed using a contact goniometer/tensiometer (Model 500) manufactured by Ramé-Hart, Inc. (Succasunna, New Jersey, USA). The instrument was supplied with an automated drop volume dispensing system, a motor-driven oscillator, and a halogen fiber optic illuminator. The software used to control the instrument was DROPimage Advanced. This experimental setup was used for both static and oscillating pendant drop tensiometry.

### 1.2.2 Oscillating Pendant Drop Tensiometry

The viscoelasticity of complex oil-water interfaces throughout this thesis was measured by harmonically oscillating the initial interfacial area ( $A_0$ ) at a small dilatational strain ( $\Delta A/A_0 \leq 0.025$ ) and a low frequency ( $\omega$ ), (i.e., between  $5 \times 10^{-3}$  and  $10^{-1}$  Hz) by increasing and decreasing the droplet volume using an in-line mechanical plunger. The interfacial strain and oscillation frequency used in this analysis fell below critical limits defined in the literature, allowing interfaces to be considered at mechanical equilibrium.<sup>28</sup> Frequently referred to as oscillating pendant drop

tensiometry, this technique has been applied to study the conformation of proteins,<sup>29–31</sup> as well as the viscoelasticity of phospholipids,<sup>32</sup> low molecular weight surfactants,<sup>27,33–36</sup> and mixed surfactant/polymer solutions<sup>37</sup> at oil-water and air-water interfaces. In this technique, the apparent complex viscoelastic modulus ( $E^*$ ) is determined by measuring the response in interfacial tension variation ( $\Delta\gamma$ ) resulting from a small, harmonically applied strain ( $\Delta A/A_0$ ), as well as the phase angle ( $\delta$ ) between the periodic interfacial tension and strain curves of an interfacial element.<sup>25</sup> The magnitude of  $E^*$  is given by  $E = \frac{\Delta\gamma}{\Delta A/A_0} = E' + iE''$ .

This modulus is primarily a measure of the system's response to dilatational deformation (although, there is some evidence to suggest that shear contributions may be present in mm-scale oscillating droplet measurements as well<sup>38,39</sup>) and quantifies the elastic storage modulus ( $E'$ ) and the viscous loss modulus ( $E''$ ), both dependent on the oscillation frequency. For the oscillating drop measurements conducted in Chapter 2, the rheological behavior of surfactant adsorbed interfaces was monitored over 24 hours and area oscillations were imposed every 60 minutes. The first oscillatory measurement occurred 1 hour after the formation of a fresh oil drop at the tip of the inverted needle. Experiments were performed in a standard laboratory environment ( $T = 23^\circ\text{C}$ ).

### 1.3 Viscoelastic Behavior of Single- and Multi-Component Liquid Interfaces

Numerous interesting questions remain in the study of interfacial rheology. One of which is what types of single- and multi-component interfacial layers can be probed with interfacial rheological measurements? Another is whether shear or dilatational measurements are more useful for practical applications of foams and emulsions? Several important classes of surface-active compounds have been studied in interfacial rheological investigations. However, depending on various physicochemical aspects of the adsorbed species, the properties that can be obtained from

experimental investigations can vary widely. For example, relaxation rates for low molecular weight surfactants can be orders of magnitude shorter than those of solid, interfacially adsorbed particles<sup>31</sup> and techniques capable of probing these rapid relaxation dynamics remain scarce.

### 1.3.1 Low Molecular Weight Surfactants

Interfacial rheology has been applied extensively to the study of low molecular weight surfactants adsorbed to immiscible fluid interfaces, both under shear and dilatational deformations. Most commercial low molecular weight surfactants do not generally produce significant shear or dilatational responses when solely adsorbed to fluid interfaces; however, their response to shear deformation has been shown to become quite significant when co-adsorbed with other species (e.g., SDS/chitosan complexes,<sup>32</sup> or C<sub>12</sub>TAB/polystyrene sulfonate<sup>33</sup>). Diffusional relaxation is most often presumed to be the mechanism responsible for the viscoelastic response of interfaces laden with low-molecular weight surfactants and, in general, larger, slow-diffusing species adsorbed to interfaces produce more substantial viscoelastic responses. In a similar manner, interfaces containing surfactant concentrations below saturation result in higher rheological responses because interfacial tension gradients have longer relaxation times under these conditions, whereas tension gradients within interfaces laden with rapidly diffusing soluble surfactants at saturation are shorter-lived and dilatational stresses are less important.<sup>34</sup>

Phospholipids are highly relevant to the morphology and mechanical behavior of biological membranes, and as such, their interfacial rheological behavior has been studied extensively in the literature.<sup>35–38</sup> In contrast to the rheological behavior of most soluble surfactants, phospholipids are insoluble in most bulk liquids and can exhibit substantial dilatational elasticity at fluid interfaces ( $E' \sim 10^{-1} \text{ N m}^{-1}$ ).<sup>39,40</sup> However, the rheological response of these molecules to shear (Figure 1-3)<sup>41</sup> has been shown to be several orders of magnitude lower ( $G' \sim 10^{-6} \text{ N m}^{-1}$ ).<sup>41,42</sup> The

discrepancy between the magnitudes of the dilatational and shear moduli suggests that phospholipid monolayers readily undergo shear if such modes are available, but yield outstanding mechanical performance under predominately dilatational deformations, as with lung alveoli.<sup>43,44</sup> As such, the dilatational rheology of the phospholipid dipalmitoyl phosphatidylcholine (DPPC) was studied extensively in Chapter 2 and Chapter 3 of this thesis.

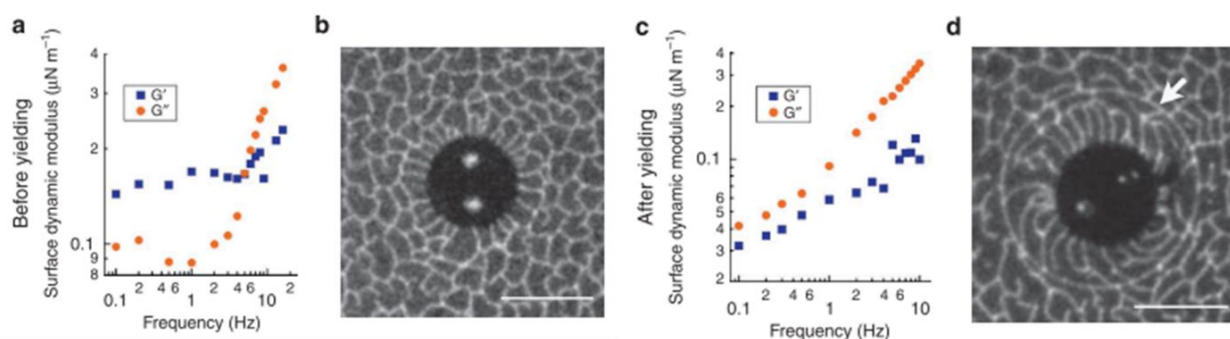


**Figure 1-3** Illustration of the history dependent linear viscoelasticity of dipalmitoylphosphatidylcholine (DPPC) at the air-water interface analyzed with a Ferromagnetic ‘microbutton’ probe. Note the relative magnitudes of  $G'$  and  $G''$  in (a) and (c), as well as the transition from  $G' > G''$  to  $G'' > G'$  upon yielding. The micrographs in (b) and (d) illustrate the formation of a shear plane, given by the arrow (scale bar, 20  $\mu\text{m}$ ).<sup>41</sup>

### 1.3.2 Surface-Active Particles

In many regards, particles behave much like surfactant molecules when adsorbed to immiscible fluid interfaces. Detailed reviews which outline the adsorptive and stabilizing properties of particles (as compared to common surfactant molecules) at the fluid-fluid interfaces can be found in the literature.<sup>45,46</sup> For interface adsorbing particles, one of the most important parameters for predicting their potential effect on the stabilizing behavior of the interface is the contact angle,  $\theta$ , it forms with the interface. Hydrophilic particles, e.g. iron oxide, tend to adopt a contact angle (measured through the aqueous phase)  $< 90^\circ$ , whereas hydrophobic particle, e.g. asphaltenes and polystyrene latexes, usually take on contact angles  $> 90^\circ$ . Analogous to surfactants with relatively high HLB values, particle monolayer predominantly comprised of particles with  $\theta < 90^\circ$  will tend to form oil-in-water emulsions, and vice-versa for particle interfacial monolayers primarily containing particles with  $\theta > 90^\circ$ .

A vital difference between the adsorption of surfactants and particles is that particles can irreversibly attach to fluid-fluid interfaces. For sufficiently small spherical particles (usually less than  $\sim 10$  microns in diameter) such that gravitational effects can be considered negligible, the detachment energy per particle,  $\Delta G$ , can be quantitatively described by  $\Delta G = \pi r^2 \gamma (1 - |\cos \theta|)^2$ , where  $r$  is the particle radius of the particle and  $\gamma$  is the interfacial tension between the bulk phases.<sup>47</sup> The attachment energy for a  $1 \mu\text{m}$  radius particle at an oil-water interface with  $\gamma = 50 \text{ mN m}^{-1}$  and  $\theta = 75^\circ$  can be  $\sim 2 \cdot 10^7 \text{ k}_B\text{T}$ , suggesting that particles are unlikely leave the interface without a substantial driving energy.<sup>46</sup> The mechanical properties of high-interface materials such as oil-water emulsions are often significantly dependent on the mechanical behavior of the interfaces themselves.<sup>48</sup>

The three-phase contact angle that a particle adopts at the interface of two fluid describes its relative affinity for either fluid phase and can control the morphology and interfacial curvature between the bulk phases. Jamming between particles within an interfacial layer has been proposed as the primary contributing mechanism to the observed non-Newtonian rheological behavior, and both nanoscale and microscale particles have been studied for their possible interfacial contributions.<sup>45</sup> The interfacial rheological behavior of particles has been studied most widely through shear measurements, and adsorbed particles are known to produce substantial interfacial shear rigidity when they undergo aggregation (Figure 1-4).<sup>46,49</sup> Adsorbed particles consistently produce high dilatational and shear moduli<sup>50</sup> and they are of special interest for further investigations because of their potential applications in bi-continuous Pickering emulsions.<sup>46</sup> Due to the known contribution to dilatational viscoelasticity and interfacial stabilization of adsorbed particles, SiO<sub>2</sub> nanoparticle-surfactant complexes were emphasized in Chapter 3 of this thesis.

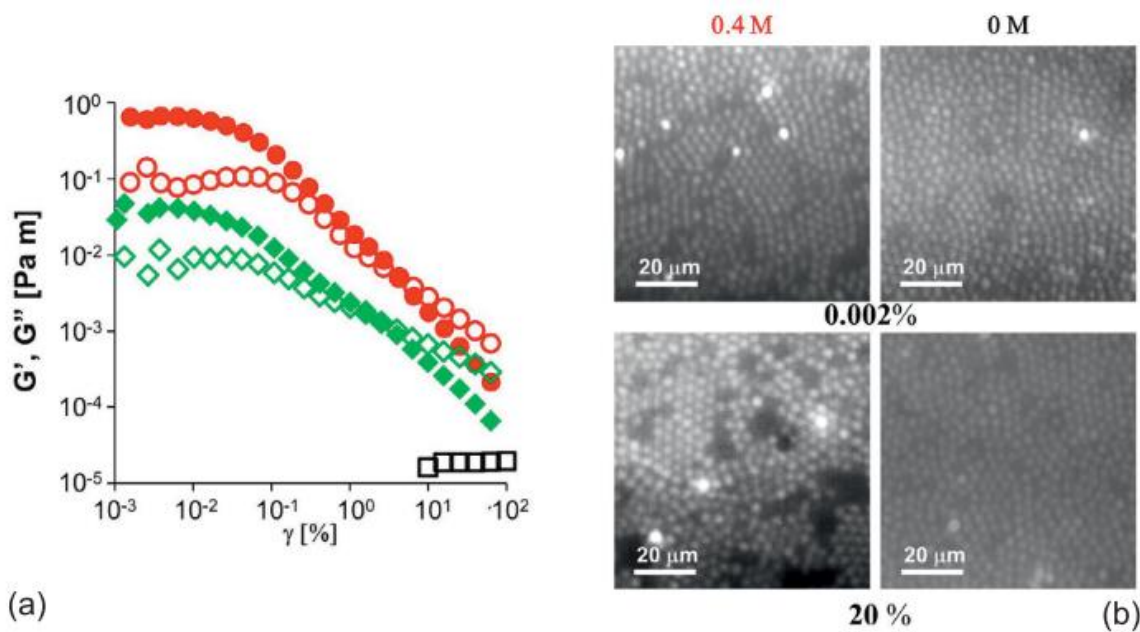


**Figure 1-4** (a) Elastic (closed) and viscous (open) shear moduli at  $1 \text{ rad s}^{-1}$  for  $3 \mu\text{m}$  polystyrene particles at 79% coverage at an air-water interface with 0.4 M NaCl (circles), 0.004 M NaCl (diamonds), and 0 M NaCl (squares). (b) corresponding micrographs for these systems at 0.002% and 20% interfacial strain.<sup>46,47</sup>

### 1.3.3 Connecting Interfacial Mechanics to the Stability of Emulsions and Foams

Links between the interfacial mechanics and bulk behavior of emulsions and foams have been observed by numerous authors. Interfacial rheological studies of proteins have shown that jammed, rigid interfaces provide considerable resilience to coalescence (droplet merging).<sup>18,48,51,52</sup> In addition to acting against droplet deformation, interfacial viscoelasticity can also lead to irregular droplet break-up during emulsification, and ultimately, high dispersity within a complex fluid system.<sup>53,54</sup> Thus, understanding the rheological parameters of interfacial layers within a complex system of immiscible fluids is vitally important.

## 1.4 Mechanisms of Emulsion Destabilization and Their Characterization

Emulsion stability refers to the tendency for the physical properties of the system to change over time under the influence of an internal or external force. Emulsion destabilization can be imposed by several physical mechanisms, the most dominant being coalescence, flocculation, and gravitational phase separation. In practice, emulsion destabilization typically occurs as two or more physical mechanisms transpire simultaneously. For example, an emulsion with rapidly flocculating droplets will subsequently lead to large aggregates that are strongly influenced by gravitational effects. This will in turn lead to faster rates of gravitational phase separation (i.e., creaming or sedimentation) of the aggregated droplets. Establishing effective strategies for modulating the stability of emulsified systems requires a deep understanding of how these destabilization mechanisms can be controlled.

In Chapter 2 of this work, a criterion for inhibiting the susceptibility to droplet coalescence of dilute oil-in-water emulsions based on the rheological properties of the surfactant-stabilized interfaces is presented. In Chapter 3, the impedance of droplet coalescence in concentrated oil-in-water emulsions by interfacially adsorbed nanoparticle-surfactant complexes is described. In Chapters 4 and 5, emulsion destabilization mechanisms are used to produce desirable physical behavior in bulk emulsions.

### 1.4.1 Gravitational Phase Separation

An emulsion's resilience to gravitational separation can be determined inexpensively through visual observation analyses, otherwise known as "oiling off" tests<sup>55</sup>. Oiling off tests are used extensively in Chapters 2, 3 and 4 of this work. This method consists of quantifying the amount of oil that forms as a distinct separate layer at the top of an oil-in-water emulsion over a certain period. The height of the serum layer,  $H_s$ , and the height of the emulsion layer,  $H_E$ , are

measured, and the relative extent of oiling off is given by  $\% \text{Oiling Off} = 100 \times \frac{H_S}{H_E}$ . This method can be applied to emulsions that have or have not been subjected to additional environmental stresses other than standard gravity. In a similar manner, the percent of oiling off can be measured by differential scanning calorimetry, where the volume fraction of oil that crystallizes at low versus high temperatures is correlated to the fraction of oiling off.<sup>56</sup>

### 1.4.2 Droplet Flocculation and Coalescence

Droplet flocculation is a colloidal aggregation phenomenon where individual droplets associate with one another but retain their individual integrities. This emulsion destabilization mechanism occurs when attractive colloidal interactions overcome long-range repulsive forces, but not short-range repulsive forces, thus complete droplet merging does not occur. For dilute emulsions, droplet flocculation results in an increase in particle size which accelerates the rate of gravitational separation.<sup>57</sup> Induced droplet flocculation can therefore be a viable route for reducing the kinetic stability of dilute, electrostatically stabilized oil-in-water emulsions.

Coalescence is an aggregation phenomenon where individual droplets merge to form a single larger droplet. Like flocculation, this destabilization mechanism causes dispersed liquid droplets to phase separate more rapidly due to enhanced gravitational effects resulting from increased droplet sizes. Coalescence is less likely to occur naturally in very dilute emulsions comprised of electrostatically stabilized interfaces due to the relatively low collision frequencies between dispersed droplets.<sup>20</sup> However, coalescence becomes a dominant destabilization mechanism in concentrated emulsions, where droplet interfaces remain in contact for extended periods. In the case of oil-in-water emulsions, a fully developed understanding of the system's susceptibility to coalescence will be highly relevant to the anticipated behavior of phase separated layers.

Coalescence and flocculation between dispersed droplets can be observed directly with optical microscopy. This process consists of placing an aliquot of an emulsion on a microscope slide and monitoring the change in the droplet size distribution as a function of time. The rate of sequential merging between the droplets provides insight on an emulsion's susceptibility/resistance to coalescence. Moreover, for droplets that do not merge completely but halt in an aggregated state, the size of the flocs and degree of flocculation can also be directly observed using microscopy. Optical microscopy is used extensively for characterizing the degree of flocculation and coalescence in Chapters 3, 4 and 5 of this thesis. Changes in an emulsion's droplet size distribution during storage can also be studied using more advanced forms of microscopy, such as confocal laser scanning microscopy.<sup>58,59</sup>

## **1.5 Particle Size Characterization**

The relative size of the droplets in an oil-water emulsion has a substantial impact on the overall stability of the system, specifically regarding the droplets' tendency toward gravitational phase separation, flocculation, and coalescence. Therefore, reliably measuring and specifying the size of emulsion droplets is vital. Particle size analyzers that incorporate light scattering are quite effective providing quantitative information on the size distributions of dispersed emulsion droplets. Some systems can provide size distribution information for droplets dispersed in a dilute emulsion ranging from 10 nm to 1 mm in diameter. These tools enable detailed analyses of various mechanisms that contribute to the stability of emulsions, such as coalescence and flocculation, by indirectly observing any changes in the system's size distribution with respect to time.

Dynamic light scattering (also known as photon correlation spectroscopy) is used extensively for this purpose in Chapters 2, 3, 4, and 5 of this work. A Malvern Zetasizer Nano ZS was used for each of these measurements. Determining particle size distributions with this tool is

performed by measuring the Brownian motion of the dispersed particles and relating it to their size. This is done by illuminating the particles with a laser and analyzing the intensity fluctuations of the scattered light. The underlying principle of this method is that small particles diffuse quickly by Brownian motion in a dispersion medium, scattering very little incident light as they move. Contrarily, large particles diffuse slowly, scattering a large amount of light as they move. These scattering characteristics are then correlated to the distribution of sizes of the dispersed particles.

## 1.6 Particle Surface Charge Characterization

The dispersed droplets in most emulsions have a considerable electrical charge. Given that the electrostatic interactions between similarly charged droplets is repulsive, droplet surface charge is often key to enhancing an emulsion's resistance to droplet flocculation and coalescence. Many of the common emulsifiers used to stabilize emulsions are anionic, cationic, or nonionic, depending on their molecular architectures and the prevailing environmental conditions (e.g., pH, ionic strength, and temperature). The magnitude and sign of the electrical charge at surface of dispersed emulsion droplets therefore depends on the type of emulsifier(s) present. The surface charge density ( $\sigma$ ) and the electrical surface potential ( $\Psi_0$ ) are two parameters often used to describe the electrical properties of a droplet interface, and properties of the fluid in which the droplets are dispersed can be described in terms of its ion concentration<sup>61</sup>. A useful mathematical expression known as the Poisson–Boltzmann equation relates the electrical potential in the immediate proximity of a charged surface to the concentration and valence of ions present in the surrounding electrolyte solution, and is given by  $\frac{d^2\Psi(x)}{dx^2} = -\frac{e}{\epsilon_0\epsilon_R} \sum_i z_i n_{0i} \exp\left(\frac{-z_i e\Psi(x)}{k_B T}\right)$ , where  $n_{0i}$  is the concentration of ionic species of type  $i$  in the bulk electrolyte solution (in molecule  $\text{m}^{-3}$ ),  $z_i$  is the valence of ionic species  $i$ ,  $e$  is the elementary charge ( $1.602 \times 10^{-19}$  C),  $\epsilon_0$  is the dielectric

constant of a vacuum,  $\epsilon_R$  is the relative dielectric constant of the medium, and  $\Psi(x)$  is the electrical potential at a distance  $x$  from the charged surface.

The effective charge of an emulsion droplet dispersed in a continuous fluid, known as the zeta ( $\xi$ ) potential, can be quantified with electrophoresis measurements. This technique was implemented extensively in Chapters 2 through 4 of this work using dynamic light scattering analysis with a Malvern Zetasizer Nano ZS. The measurement procedure consists of placing an aliquot of a dilute emulsion into a folded capillary cell. The emulsion (or particulate dispersion) rests between two electrodes and an alternating current is applied to the system. The rate at which the droplets oscillate within the applied electric field is directly correlated to the magnitude of the charge on the particles at the “shear-plane”, which essentially describes the charged ionic cloud that extends from the true surface of the drop (or particle) into the surrounding fluid media. In general, droplets with large magnitudes of the  $\xi$  potential are more resistant to coalescence and flocculation due to electrostatic repulsive forces. Therefore, having a detailed understanding of the  $\xi$  potential in real and model emulsions is of vital importance.

## 1.7 References

- (1) McClements, D. J. *Food Emulsions Principles, Practices, and Techniques*; CRC Press, 2005. <https://doi.org/10.1093/acprof:oso/9780195383607.003.0002>.
- (2) Dickinson, E. Food Emulsions and Foams: Stabilization by Particles. *Curr. Opin. Colloid Interface Sci.* **2010**, *15* (1–2), 40–49. <https://doi.org/10.1016/j.cocis.2009.11.001>.
- (3) Were, L. M.; Bruce, B. D.; Davidson, P. M.; Weiss, J. Size, Stability, and Entrapment Efficiency of Phospholipid Nanocapsules Containing Polypeptide Antimicrobials. *J. Agric. Food Chem.* **2003**, *51* (27), 8073–8079. <https://doi.org/10.1021/jf0348368>.
- (4) Pichot, R.; Watson, R. L.; Norton, I. T. Phospholipids at the Interface: Current Trends and Challenges. *Int. J. Mol. Sci.* **2013**, *14* (6), 11767–11794. <https://doi.org/10.3390/ijms140611767>.
- (5) Gil, J.; Bachofen, H.; Gehr, P.; Weibel, E. R. Alveolar Volume-Surface Area Relation in Air- and Saline-Filled Lungs Fixed by Vascular Perfusion. *J Appl Physiol* **1979**, *47* (5), 990–1001. <https://doi.org/10.1143/JPSJ.58.4643>.
- (6) Discher, B. M. Polymersomes: Tough Vesicles Made from Diblock Copolymers. *Science* (80-. ). **1999**, *284* (5417), 1143–1146. <https://doi.org/10.1126/science.284.5417.1143>.
- (7) Muhiddinov, Z.; Khalikov, D.; Speaker, T.; Fassihi, R. Development and Characterization of Different Low Methoxy Pectin Microcapsules by an Emulsion-Interface Reaction Technique. *J. Microencapsul.* **2004**, *21* (7), 729–741. <https://doi.org/10.1080/02652040400008507>.
- (8) Walter, A.; Rehage, H.; Leonhard, H. Shear Induced Deformation of Microcapsules: Shape Oscillations and Membrane Folding. *Colloids Surfaces A Physicochem. Eng. Asp.* **2001**, *183* (185), 123–132. [https://doi.org/10.1016/S0927-7757\(01\)00564-7](https://doi.org/10.1016/S0927-7757(01)00564-7).
- (9) Ma, J.; Wang, Y.; Liu, J. Biomaterials Meet Microfluidics: From Synthesis Technologies to Biological Applications. *Micromachines* **2017**, *8* (8). <https://doi.org/10.3390/mi8080255>.
- (10) Danov, K. D.; Kralchevsky, P. A.; Ivanov, I. B. Equilibrium and Dynamics of Surfactant Adsorption Monolayers and Thin Liquid Films Part 2. In *Handbook of Detergents*; Dekker, New York, 1999; pp 303–418.
- (11) Miller, R.; Wüstneck, R.; Krägel, J.; Kretschmar, G. Dilational and Shear Rheology of Adsorption Layers at Liquid Interfaces. *Colloids Surfaces A Physicochem. Eng. Asp.* **1996**, *111* (1–2), 75–118. [https://doi.org/10.1016/0927-7757\(95\)03492-7](https://doi.org/10.1016/0927-7757(95)03492-7).
- (12) Ravera, F.; Ferrari, M.; Santini, E.; Liggieri, L. Influence of Surface Processes on the Dilational Visco-Elasticity of Surfactant Solutions. *Adv. Colloid Interface Sci.* **2005**, *117* (1–3), 75–100. <https://doi.org/10.1016/j.cis.2005.06.002>.
- (13) Liggieri, L.; Miller, R. *Interfacial Rheology*; CRC Press, 2009.

- (14) Miller, R.; Ferri, J. K.; Javadi, A.; Krägel, J.; Mucic, N.; Wüstneck, R. Rheology of Interfacial Layers. *Colloid Polym. Sci.* **2010**, *288*, 937–950. <https://doi.org/10.1007/s00396-010-2227-5>.
- (15) Alvarez, N. J.; Walker, L. M.; Anna, S. L. Diffusion-Limited Adsorption to a Spherical Geometry: The Impact of Curvature and Competitive Time Scales. *Phys. Rev. E - Stat. Nonlinear, Soft Matter Phys.* **2010**, *82* (1), 1–8. <https://doi.org/10.1103/PhysRevE.82.011604>.
- (16) Krägel, J.; Derkatch, S. R. Interfacial Shear Rheology. *Curr. Opin. Colloid Interface Sci.* **2010**, *15* (4), 246–255. <https://doi.org/10.1016/j.cocis.2010.02.001>.
- (17) Georgieva, D.; Cagna, A.; Langevin, D. Link between Surface Elasticity and Foam Stability. *Soft Matter* **2009**, *5* (10), 2063–2071. <https://doi.org/10.1039/b822568k>.
- (18) Dicharry, C.; Arla, D.; Sinquin, A.; Graciaa, A.; Bouriat, P. Stability of Water/Crude Oil Emulsions Based on Interfacial Dilatational Rheology. *J. Colloid Interface Sci.* **2006**, *297* (2), 785–791. <https://doi.org/10.1016/j.jcis.2005.10.069>.
- (19) Hudson, S. D.; Jamieson, A. M.; Burkhart, B. E. The Effect of Surfactant on the Efficiency of Shear-Induced Drop Coalescence. *J. Colloid Interface Sci.* **2003**, *265* (2), 409–421. [https://doi.org/10.1016/S0021-9797\(03\)00396-5](https://doi.org/10.1016/S0021-9797(03)00396-5).
- (20) McClements, D. J. Critical Review of Techniques and Methodologies for Characterization of Emulsion Stability. *Crit. Rev. Food Sci. Nutr.* **2007**, *47* (7), 611–649. <https://doi.org/10.1080/10408390701289292>.
- (21) Fuller, G. G.; Vermant, J. Complex Fluid-Fluid Interfaces: Rheology and Structure. *Annu. Rev. Chem. Biomol. Eng.* **2012**, *3* (1), 519–543. <https://doi.org/10.1146/annurev-chembioeng-061010-114202>.
- (22) Verwijlen, T.; Moldenaers, P.; Vermant, J. A Fixture for Interfacial Dilatational Rheometry Using a Rotational Rheometer. *Eur. Phys. J. Spec. Top.* **2013**, *222* (1), 83–97. <https://doi.org/10.1140/epjst/e2013-01828-9>.
- (23) Schramm, L. L. *Emulsions, Foams, and Suspensions: Fundamentals and Applications*; 2005.
- (24) Slattery, J. C.; Sagis, L. M. C.; Oh, E.-S. *Interfacial Transport Phenomena*, 2nd ed.; Springer, 2007.
- (25) Boussinesq, M. J. Sur l'existence d'une Viscosité Superficielle, Dans La Mince Couche de Transition Séparant Un Liquide d'un Autre Fluide Contigu. *Ann. Chim. Phys* **1913**, *29*, 349–357.
- (26) Scriven, L. E. Dynamics of a Fluid Interface Equation of Motion for Newtonian Surface Fluids. *Chem. Eng. Sci.* **1960**, *12* (2), 98–108. [https://doi.org/10.1016/0009-2509\(60\)87003-0](https://doi.org/10.1016/0009-2509(60)87003-0).

- (27) Erni, P. Deformation Modes of Complex Fluid Interfaces. *Soft Matter* **2011**, 7 (17), 7586. <https://doi.org/10.1039/c1sm05263b>.
- (28) Evans, E.; Needham, D. Physical Properties of Surfactant Bilayer Membranes: Thermal Transitions, Elasticity, Rigidity, Cohesion, and Colloidal Interactions. *J. Phys. Chem.* **1987**, 91 (16), 4219–4228. <https://doi.org/10.1021/j100300a003>.
- (29) Derkach, S. R.; Krägel, J.; Miller, R. Methods of Measuring Rheological Properties of Interfacial Layers (Experimental Methods of 2D Rheology). *Colloid J.* **2009**, 71 (1), 1–17. <https://doi.org/10.1134/S1061933X09010013>.
- (30) Erk, K. A.; Martin, J. D.; Schwalbe, J. T.; Phelan, F. R.; Hudson, S. D. Shear and Dilational Interfacial Rheology of Surfactant-Stabilized Droplets. *J. Colloid Interface Sci.* **2012**, 377 (1), 442–449. <https://doi.org/10.1016/j.jcis.2012.03.078>.
- (31) Rotenberg, Y.; Boruvka, L.; Neumann, A. . Determination of Surface Tension and Contact Angle from the Shapes of Axisymmetric Fluid Interfaces. *J. Colloid Interface Sci.* **1983**, 93 (1), 169–183. [https://doi.org/10.1016/0021-9797\(83\)90396-X](https://doi.org/10.1016/0021-9797(83)90396-X).
- (32) Chen, P.; Prokop, R. M.; Susnar, S. S.; Neumann, A. W. Interfacial Tensions of Protein Solutions Using Axisymmetric Drop Shape Analysis. *Stud. Interface Sci.* **1998**, 7 (C), 303–339. [https://doi.org/10.1016/S1383-7303\(98\)80055-0](https://doi.org/10.1016/S1383-7303(98)80055-0).
- (33) Benjamins, J.; Cagna, A.; Lucassen-Reynders, E. H. Viscoelastic Properties of Triacylglycerol/Water Interfaces Covered by Proteins. *Colloids Surfaces A Physicochem. Eng. Asp.* **1996**, 114, 245–254. [https://doi.org/10.1016/0927-7757\(96\)03533-9](https://doi.org/10.1016/0927-7757(96)03533-9).
- (34) Ravera, F.; Loglio, G.; Kovalchuk, V. I. Interfacial Dilational Rheology by Oscillating Bubble/Drop Methods. *Current Opinion in Colloid and Interface Science*. Elsevier Ltd 2010, pp 217–228. <https://doi.org/10.1016/j.cocis.2010.04.001>.
- (35) Leser, M. E.; Acquistapace, S.; Cagna, A.; Makievski, A. V.; Miller, R. Limits of Oscillation Frequencies in Drop and Bubble Shape Tensiometry. *Colloids Surfaces A Physicochem. Eng. Asp.* **2005**, 261 (1–3), 25–28. <https://doi.org/10.1016/j.colsurfa.2004.11.043>.
- (36) Wang, J. M.; Xia, N.; Yang, X. Q.; Yin, S. W.; Qi, J. R.; He, X. T.; Yuan, D. B.; Wang, L. J. Adsorption and Dilational Rheology of Heat-Treated Soy Protein at the Oil-Water Interface: Relationship to Structural Properties. *J. Agric. Food Chem.* **2012**, 60 (12), 3302–3310. <https://doi.org/10.1021/jf205128v>.
- (37) Wan, Z. L.; Wang, L. Y.; Wang, J. M.; Yuan, Y.; Yang, X. Q. Synergistic Foaming and Surface Properties of a Weakly Interacting Mixture of Soy Glycinin and Biosurfactant Stevioside. *J. Agric. Food Chem.* **2014**, 62 (28), 6834–6843. <https://doi.org/10.1021/jf502027u>.

- (38) Cascão Pereira, L. G.; Théodoly, O.; Blanch, H. W.; Radke, C. J. Dilatational Rheology of BSA Conformers at the Air/Water Interface. *Langmuir* **2003**, *19* (6), 2349–2356. <https://doi.org/10.1021/la020720e>.
- (39) Li, J. B.; Kretzschmar, G.; Miller, R.; Möhwald, H. Viscoelasticity of Phospholipid Layers at Different Fluid Interfaces. *Colloids Surfaces A Physicochem. Eng. Asp.* **1999**, *149* (1–3), 491–497. [https://doi.org/10.1016/S0927-7757\(98\)00729-8](https://doi.org/10.1016/S0927-7757(98)00729-8).
- (40) Georgieva, D.; Schmitt, V.; Leal-Calderon, F.; Langevin, D. On the Possible Role of Surface Elasticity in Emulsion Stability. *Langmuir* **2009**, *25* (10), 5565–5573. <https://doi.org/10.1021/la804240e>.
- (41) Duerr-Auster, N.; Gunde, R.; Windhab, E. J. Structure and Mechanical Properties of a Polyglycerol Ester at the Air - Water Surface. *Langmuir* **2008**, *24* (8), 12282–12289. <https://doi.org/10.1021/la8025733>.
- (42) Sharipova, A.; Aidarova, S.; Mucic, N.; Miller, R. Dilational Rheology of Polymer/Surfactant Mixtures at Water/Hexane Interface. *Colloids Surfaces A Physicochem. Eng. Asp.* **2011**, *391* (1–3), 130–134. <https://doi.org/10.1016/j.colsurfa.2011.04.035>.
- (43) Yeung, A.; Dabros, T.; Masliyah, J. Dissipative Interfaces and Departures from the Young-Laplace Equation. *Langmuir* **1997**, *13* (13), 6597–6606. <https://doi.org/10.1021/la9706835>.
- (44) Kotula, A. P.; Anna, S. L. Regular Perturbation Analysis of Small Amplitude Oscillatory Dilatation of an Interface in a Capillary Pressure Tensiometer. *J. Rheol. (N. Y. N. Y.)* **2015**, *59* (1), 85–117. <https://doi.org/10.1122/1.4902546>.
- (45) Reynaert, S.; Moldenaers, P.; Vermant, J. Interfacial Rheology of Stable and Weakly Aggregated Two-Dimensional Suspensions. *Phys. Chem. Chem. Phys.* **2007**, *9* (48), 6463–6475. <https://doi.org/10.1039/b710825g>.
- (46) Babak, V. G.; Desbrières, J.; Tikhonov, V. E. Dynamic Surface Tension and Dilational Viscoelasticity of Adsorption Layers of a Hydrophobically Modified Chitosan. *Colloids Surfaces A Physicochem. Eng. Asp.* **2005**, *255* (1–3), 119–130. <https://doi.org/10.1016/j.colsurfa.2004.12.029>.
- (47) Monteux, C.; Williams, C. E.; Meunier, J.; Anthony, O.; Bergeron, V. Adsorption of Oppositely Charged Polyelectrolyte/Surfactant Complexes at the Air/Water Interface: Formation of Interfacial Gels. *Langmuir* **2004**, *20* (1), 57–63. <https://doi.org/10.1021/la0347861>.
- (48) Ting, L.; Wasan, D. T.; Miyano, K. Longitudinal Surface Waves for the Study of Dynamic Properties of Surfactant Systems. III. Liquid-Liquid Interface. *J. Colloid Interface Sci.* **1985**, *107* (2), 345–354. [https://doi.org/10.1016/0021-9797\(85\)90187-0](https://doi.org/10.1016/0021-9797(85)90187-0).

- (49) Nash, J. J.; Erk, K. A. Stability and Interfacial Viscoelasticity of Oil-Water Nanoemulsions Stabilized by Soy Lecithin and Tween 20 for the Encapsulation of Bioactive Carvacrol. *Colloids Surfaces A Physicochem. Eng. Asp.* **2017**, *517*, 1–11. <https://doi.org/10.1016/j.colsurfa.2016.12.056>.
- (50) Anton, N.; Pierrat, P.; Lebeau, L.; Vandamme, T. F.; Bouriat, P. A Study of Insoluble Monolayers by Deposition at a Bubble Interface. *Soft Matter* **2013**, *9* (42), 10081. <https://doi.org/10.1039/c3sm51688a>.
- (51) Saad Bhamla, M.; Chai, C.; Álvarez-Valenzuela, M. A.; Tajuelo, J.; Fuller, G. G. Interfacial Mechanisms for Stability of Surfactant-Laden Films. *PLoS One* **2017**, *12* (5), 1–14. <https://doi.org/10.1371/journal.pone.0175753>.
- (52) Rodríguez Niño, M. R.; Lucero, A.; Rodríguez Patino, J. M. Relaxation Phenomena in Phospholipid Monolayers at the Air-Water Interface. *Colloids Surfaces A Physicochem. Eng. Asp.* **2008**, *320* (1–3), 260–270. <https://doi.org/10.1016/j.colsurfa.2008.02.008>.
- (53) Kotula, A. P.; Anna, S. L. Insoluble Layer Deposition and Dilatational Rheology at a Microscale Spherical Cap Interface. *Soft Matter* **2016**, *12* (33), 7038–7055. <https://doi.org/10.1039/C5SM03133H>.
- (54) Choi, S. Q.; Steltenkamp, S.; Zasadzinski, J. A.; Squires, T. M. Active Microrheology and Simultaneous Visualization of Sheared Phospholipid Monolayers. *Nat. Commun.* **2011**, *2* (1), 312–316. <https://doi.org/10.1038/ncomms1321>.
- (55) Kim, K.; Choi, S. Q.; Zasadzinski, J. A.; Squires, T. M. Interfacial Microrheology of DPPC Monolayers at the Air-water Interface. *Soft Matter* **2011**, *7* (17), 7782. <https://doi.org/10.1039/c1sm05383c>.
- (56) Ghadiali, S. N.; Gaver, D. P. An Investigation of Pulmonary Surfactant Physicochemical Behavior under Airway Reopening Conditions. *J. Appl. Physiol.* **2000**, *88* (2), 493–506.
- (57) Ghadiali, S. N.; Gaver, D. P. The Influence of Non-Equilibrium Surfactant Dynamics on the Flow of a Semi-Infinite Bubble in a Rigid Cylindrical Capillary Tube. *J. Fluid Mech.* **2003**, *478* (478), 165–196. <https://doi.org/10.1017/S002211200200335X>.
- (58) Binks, B. P. Particles as Surfactants - Similarities and Differences. *Curr. Opin. Colloid Interface Sci.* **2002**, *7* (1–2), 21–41. [https://doi.org/10.1016/S1359-0294\(02\)00008-0](https://doi.org/10.1016/S1359-0294(02)00008-0).
- (59) Thijssen, J. H. J.; Vermant, J. Interfacial Rheology of Model Particles at Liquid Interfaces and Its Relation to (Bicontinuous) Pickering Emulsions. *J. Phys. Condens. Matter* **2018**, *30* (2). <https://doi.org/10.1088/1361-648X/aa9c74>.
- (60) Aveyard, R.; Binks, B. P.; Clint, J. H. Emulsions Stabilised Solely by Colloidal Particles. *Adv. Colloid Interface Sci.* **2003**, *100–102* (SUPPL.), 503–546. [https://doi.org/10.1016/S0001-8686\(02\)00069-6](https://doi.org/10.1016/S0001-8686(02)00069-6).

- (61) Langevin, D. Influence of Interfacial Rheology on Foam and Emulsion Properties. *Adv. Colloid Interface Sci.* **2000**, 88 (1–2), 209–222. [https://doi.org/10.1016/S0001-8686\(00\)00045-2](https://doi.org/10.1016/S0001-8686(00)00045-2).
- (62) Barman, S.; Christopher, G. F. Role of Capillarity and Microstructure on Interfacial Viscoelasticity of Particle Laden Interfaces. *J. Rheol. (N. Y. N. Y.)* **2016**, 60 (35).
- (63) Mendoza, A. J.; Guzmán, E.; Martínez-Pedrero, F.; Ritacco, H.; Rubio, R. G.; Ortega, F.; Starov, V. M.; Miller, R. Particle Laden Fluid Interfaces: Dynamics and Interfacial Rheology. *Adv. Colloid Interface Sci.* **2014**, 206, 303–319. <https://doi.org/10.1016/j.cis.2013.10.010>.
- (64) Erni, P.; Fischer, P.; Windhab, E. J. Sorbitan Tristearate Layers at the Air/Water Interface Studied by Shear and Dilatational Interfacial Rheology. *Langmuir* **2005**, 21 (23), 10555–10563. <https://doi.org/10.1021/la0514664>.
- (65) Erni, P.; Windhab, E. J.; Fischer, P. Interfacial Rheology in Food Science and Technology. In *Interfacial Rheology*; Liggieri, L., Miller, R., Eds.; CRC Press, 2009; pp 615–644. <https://doi.org/10.1163/ej.9789004175860.i-684>.
- (66) Williams, A.; Prins, A. Comparison of the Dilational Behaviour of Adsorbed Milk Proteins in the Air-Water and Oil-Water Interfaces. *Colloids Surfaces A Physicochem. Eng. Asp.* **1996**, 114 (1), 267–275. [https://doi.org/10.1016/0927-7757\(96\)03534-0](https://doi.org/10.1016/0927-7757(96)03534-0).
- (67) Williams, A.; Janssen, J. J. M.; Prins, A. Behaviour of Droplets in Simple Shear Flow in the Presence of a Protein Emulsifier. *Colloids Surfaces A Physicochem. Eng. Asp.* **1997**, 125 (2–3), 189–200. [https://doi.org/10.1016/S0927-7757\(96\)03972-6](https://doi.org/10.1016/S0927-7757(96)03972-6).
- (68) McClements, D. J. Critical Review of Techniques and Methodologies for Characterization of Emulsion Stability. *Crit. Rev. Food Sci. Nutr.* **2007**, 47 (7), 611–649. <https://doi.org/10.1080/10408390701289292>.
- (69) Thanasukarn, P.; Pongsawatmanit, R.; McClements, D. J. Impact of Fat and Water Crystallization on the Stability of Hydrogenated Palm Oil-in-Water Emulsions Stabilized by Whey Protein Isolate. *Colloids Surfaces A Physicochem. Eng. Asp.* **2004**, 246 (1–3), 49–59. <https://doi.org/10.1016/j.colsurfa.2004.07.018>.
- (70) Chanamai, R.; McClements, D. J. Creaming Stability of Flocculated Monodisperse Oil-in-Water Emulsions. *J. Colloid Interface Sci.* **2000**, 225 (1), 214–218. <https://doi.org/10.1006/jcis.2000.6766>.
- (71) Pontani, L.-L.; Haase, M. F.; Raczowska, I.; Brujic, J. Immiscible Lipids Control the Morphology of Patchy Emulsions. *Soft Matter* **2013**, 9 (29), 7150. <https://doi.org/10.1039/c3sm51137e>.
- (72) Pilapil, B. K.; Jahandideh, H.; Bryant, S. L.; Trifkovic, M. Stabilization of Oil-in-Water Emulsions with Noninterfacially Adsorbed Particles. *Langmuir* **2016**, 32 (28), 7109–7116. <https://doi.org/10.1021/acs.langmuir.6b00873>.

(73) Israelachvili, J. N. *Intermolecular and Surface Forces*, 3rd ed.; 2011.

## CHAPTER 2 STABILITY AND INTERFACIAL VISCOELASTICITY OF OIL-WATER NANOEMULSIONS STABILIZED BY SOY LECITHIN AND TWEEN 20 FOR THE ENCAPSULATION OF BIOACTIVE CARVACROL

Portions of the following chapter contain text and figures adapted (with permission from **J.J. Nash** and K.A. Erk) from the article, “Stability and interfacial viscoelasticity of oil-water nanoemulsions stabilized by soy lecithin and Tween 20 for the encapsulation of bioactive carvacrol,” *Colloids Surf., A*, 517, 1–11 (2017). Copyright 2016 Elsevier B.V. DOI: 10.1016/j.colsurfa.2016.12.056

### 2.1 Introduction

In recent years, the use of essential oils as natural antimicrobials in food products has attracted growing interest to meet consumers’ desires in terms of food quality and safety. These bioactive molecules are used for microbial disinfection during food processing, as well as to ensure a certain shelf-life of the food product without negatively affecting the organoleptic properties of food (*e.g.*, taste, texture).<sup>1,2</sup> Carvacrol (2-methyl-5-isopropylphenol) is an antimicrobial, lipophilic compound that is primarily derived from the essential oil fractions of oregano (~60-75%) and thyme (~45%).<sup>3-5</sup> Carvacrol is added to many food products including baked goods and nonalcoholic beverages due to its antimicrobial activity against several strains of harmful foodborne bacteria (*i.e.* *Escherichia coli*, *Staphylococcus aureus*, *Bacillus cereus*, etc.).<sup>4-8</sup> Unfortunately, carvacrol (like most lipophilic bioactive compounds) has a limited solubility in water (0.83 mg L<sup>-1</sup>),<sup>9</sup> where microorganisms are most likely to grow and proliferate.<sup>10,11</sup> Thus, more advanced delivery methods are required to incorporate lipophilic bioactive molecules into the water-rich phases within food products. One of these methods includes encapsulating the bioactive molecules in oil-based emulsion droplets.<sup>12,13</sup> Encapsulation of essential oils into

nanoscale delivery systems is known to increase their physical stability by protecting these compounds from undesirable chemical interactions with food ingredients.<sup>14</sup> Also, encapsulation of the essential oil compounds carvacrol and eugenol within nanoscale micelles has been shown to increase their antimicrobial activity by enhancing physicochemical interactions between these molecules and the outer membranes harmful microorganisms.<sup>15,16</sup>

Oil-in-water (O/W) nanoemulsions containing carvacrol have been recently created by high-energy homogenization,<sup>1</sup> as well as low-energy spontaneous emulsification.<sup>17</sup> In the latter study, initial droplet size was sensitive to the concentration of carvacrol in the carrier oil (medium chain triglyceride, MCT), and over 30 days, the droplets increased in size with the greatest increases observed for droplets containing the greatest amount of carvacrol (30, 40 wt.% carvacrol in MCT).<sup>17</sup> The authors speculate that the increased polarity of the oil phase resulting from the increased concentration of carvacrol contributed to the accelerated droplet coalescence due to weakened adsorption of the surfactant (Tween 20) to the O/W interface.<sup>18</sup> Indeed, the adsorption strength and level of intermolecular interactions of molecules adsorbed to fluid interfaces will have a strong effect on the overall kinetic stability of nanoemulsions, as well as the measured rheological response of the interface. Although, many past studies have concluded that there is not always a direct correlation between the interfacial rheological response and nanoemulsion stability.<sup>19,20</sup>

Here, to directly quantify the molecular-level interactions of surfactant-stabilized O/W nanoemulsions containing carvacrol, we investigated O/W droplet interfaces containing zwitterionic (soy lecithin) or non-ionic (Tween 20) molecules using axisymmetric drop shape analysis. Lecithin is a naturally derived mixture of zwitterionic phospholipid molecules widely used as an emulsifying agent in the food industry. Its major component, phosphatidylcholine, is composed of a polar head group containing phosphocholine and glycerol residue.

Phosphatidylcholine also contains a non-polar region composed of two hydrocarbon fatty acid chains. The effectiveness of lecithin as a nanoemulsion stabilizer is attributed to the self-assembly of the molecule at the O/W interface and subsequent formation of a thick viscoelastic film strengthened by hydrogen bonding between phosphate groups on neighboring molecules.<sup>21</sup> Tween 20 is a food-grade, non-ionic surfactant containing a polyoxyethylene head group and fatty acid tail linked together by sorbitol. Recent investigations have attributed the protection against oil droplet coalescence in O/W emulsions stabilized by Tween 20 to the high surface activity and steric interactions of Tween 20 molecules at oil droplet interfaces.<sup>18,22</sup> These surfactants were chosen to due to their widespread use as food grade emulsifiers.

This study seeks to elucidate the contribution of the rheological properties of surfactant-laden O/W interfaces in the stabilization of nanoemulsions containing carvacrol. The interfacial tension isotherms for soy lecithin or Tween 20 adsorbed O/W interfaces were measured by static pendant drop tensiometry. The development of viscoelasticity in these interfaces within the first 24 hours of formation was quantified by oscillating pendant drop tensiometry. Nanoemulsions containing these surfactants were created by ultrasonication. The Z-Average (Z-Ave) diameter and zeta ( $\zeta$ ) potential of oil droplets were measured 24 hours after formulation. The Z-Ave diameter and  $\zeta$  potential of nanoemulsions were monitored over 30 days at 23 °C under standard gravity and comparisons were made between initial and final values to illustrate extended emulsion stabilization behavior.

## **2.2 Experimental Methods**

### **2.2.1 Materials and Reagents**

For both axisymmetric drop shape analysis and nanoemulsion preparation, the aqueous phase was a citrate-phosphate buffer (5 mmol citric acid and 10 mmol dibasic sodium phosphate) mixed in various ratios to obtain pH 7 and 3 buffers. These aqueous phase pH values were selected to mimic the neutral and acidic environments of common commercial beverages, such as milk and soft drinks. Deionized water with 18 M $\Omega$  cm resistivity was obtained from a Barnsted Nanopure™ system with a 0.2  $\mu$ m filter. The emulsifying agents investigated were Ultralec® P soy lecithin (Archer Daniels Midland Specialty Products, stored at 4 °C) and Tween® 20 (Sigma-Aldrich, stored at 23 °C) and were used as received. The manufacturer reported lecithin's major phospholipid content as 23 wt.% phosphatidylcholine, 18 wt.% phosphatidylethanolamine, 15 wt.% phosphatidylinositol, and 6 wt.% phosphatidic acid.

For nanoemulsion preparation, the oil phase comprised 5 wt.% of the total 20 g nanoemulsion and the concentrations of carvacrol ( $\geq$ 99.8% pure, Sigma-Aldrich) in the oil phase were 0 (control), 5, 10, 20, 40, 60 and 80 wt.% carvacrol in Neobee® 1053 medium-chain triglyceride (MCT) oil (Stepan Specialty Products). Each oil phase mixture was passed through an alumina column three times to remove surface-active trace impurities prior to use. For axisymmetric drop shape analysis, the oil phase contained 10 wt.% carvacrol in MCT oil.

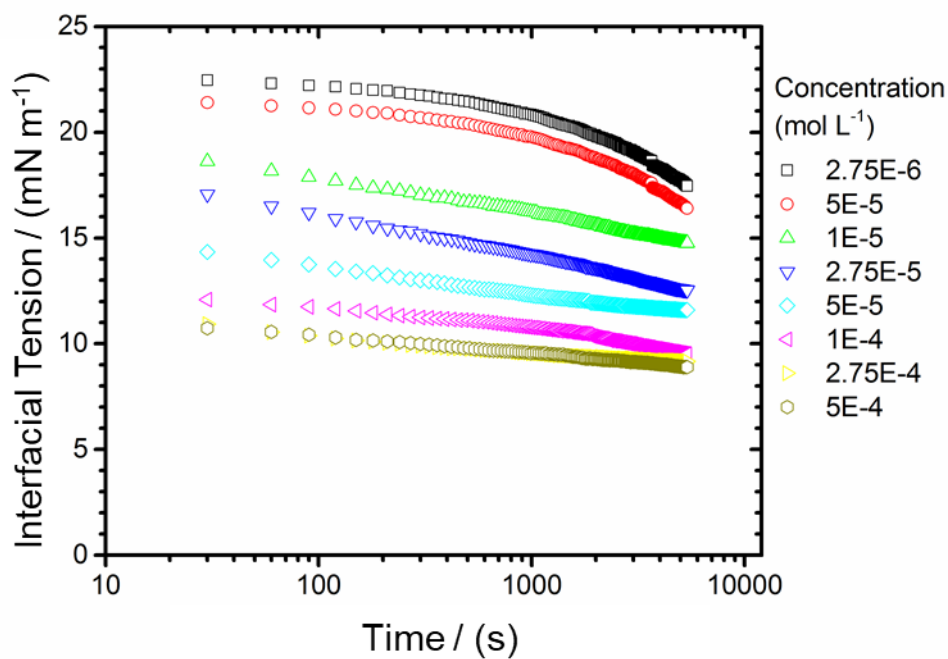
### **2.2.2 Determination of Minimum Nanoemulsion Surfactant Concentration**

In the process of nanoemulsion formulation, very large surface to volume ratios of oil droplet interfaces are generated. Therefore, the concentration of emulsifier (lecithin or Tween 20) necessary to accommodate the large interfacial areas generated were determined prior to emulsion formulation. The minimum surfactant concentration ( $C_a$ ) necessary for nanoemulsion formation is

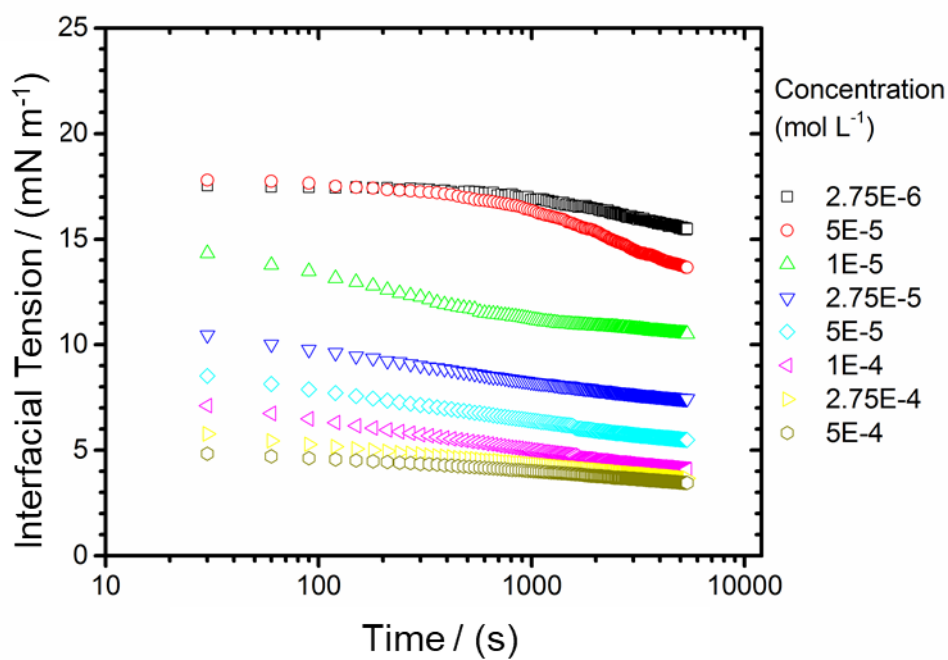
given by  $C_a = \frac{6\phi\Gamma_s}{d}$ , where  $\phi$  is the volume fraction of the disperse phase,  $d$  is the mean droplet diameter, and  $\Gamma_s$  is the surface load.<sup>40-42</sup> For our nanoemulsions, the dispersed oil phase volume fraction was  $\phi = 0.05$  and the desired droplet diameter was  $d = 150$  nm.

The surface load,  $\Gamma_s$ , was estimated by assuming that the required surfactant concentration at the O/W interfaces was equal to the surface excess concentration of the surfactant,  $\Gamma_\infty$ , where the O/W interface is saturated with surfactant molecules.<sup>43</sup> The surface excess concentration is given by Gibbs adsorption isotherm,  $\Gamma_\infty = -\frac{1}{nRT} \frac{d\gamma}{d \ln C}$ , where  $\gamma$  is the interfacial tension (mN/m),  $C$  is the bulk concentration (mol/L),  $R$  is the gas constant,  $T$  is the temperature (K), and the integer,  $n$ , accounts for the charge interactions within the polar head group of the surfactant. For non-ionic surfactants (Tween 20) the value for  $n = 1$ .<sup>44,45</sup> Likewise, the value for  $n$  may be taken as 1 for zwitterionic surfactants (lecithin) due to the zero-net ionization of the polar head group.<sup>46,47</sup>

To estimate  $\Gamma_\infty$ , the diffusion-limited equilibrium adsorption was measured for each surfactant using static pendant drop tensiometry. Dynamic O/W interfacial tension isotherms were measured for each surfactant at various concentrations until a plateau value was reached and are provided in Figure 2-1. Plateau values obtained from O/W interfacial tension isotherms were plotted as a function of surfactant concentration in Figure 2-2 to estimate  $\Gamma_\infty$ . Furthermore, these data yielded approximations for the critical aggregation concentrations (CAC) of lecithin and Tween 20. The CAC values were determined to be 0.08 g/L (0.008 wt.%) for lecithin and 0.1 g/L (0.01 wt.%) for Tween 20.



(a)



(b)

**Figure 2-1** Interfacial tension isotherms for (a) 0.35 wt.% lecithin stabilized interfaces and (b) 1 wt.% Tween 20 stabilized interfaces. The aqueous continuous phase contained the surfactant and citrate-phosphate buffer at pH 7. The oil droplet phase contained 10 wt.% carvacrol in MCT oil.

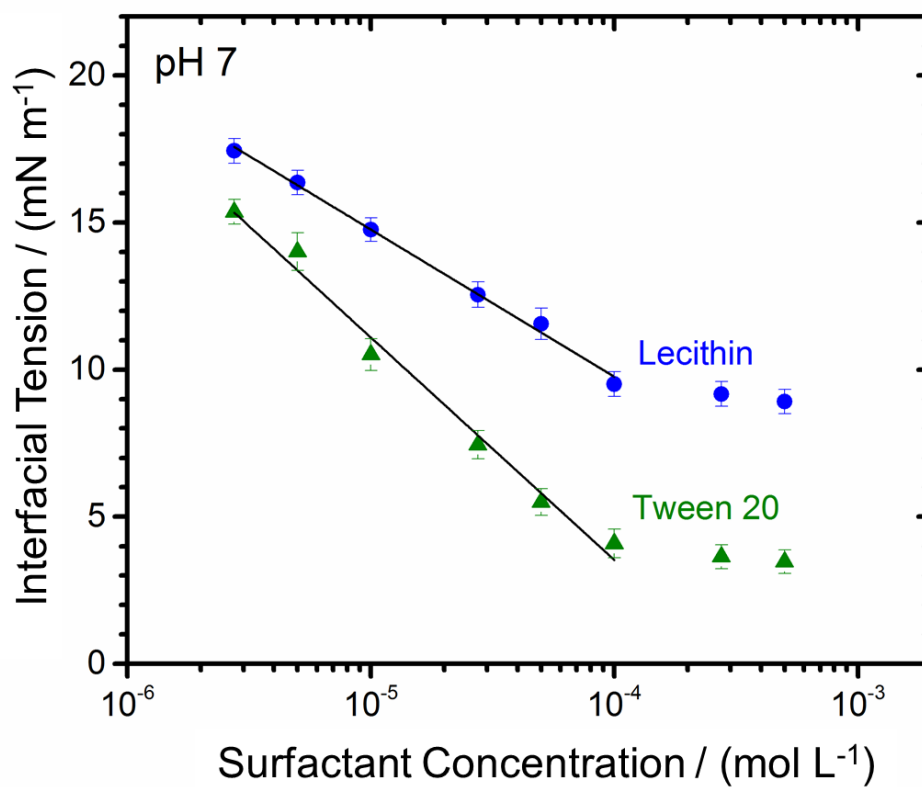


**Figure 2-2** Interfacial tension as a function of bulk surfactant concentration (mol L<sup>-1</sup>) for lecithin (blue/circles) and Tween 20 (green/triangles). Error bars represent  $\pm 1$  standard deviation. Surfactants were dispersed in a pH 7 citrate-phosphate buffer solution and the oil phase consisted of 10% (v/v) carvacrol in MCT oil. The lines are best fits of the Gibbs adsorption isotherm.

The slopes obtained from the semi-log plot of interfacial tension versus surfactant concentration, at concentrations near the point where the interfacial tension approaches a constant value, were used in the Gibbs adsorption isotherm.<sup>44,45</sup> Values for  $\Gamma_{\infty}$  were determined to be 2.0  $\mu\text{mol}/\text{m}^2$  for lecithin and 3.1  $\mu\text{mol}/\text{m}^2$  for Tween 20. Substituting these values of  $\Gamma_{\infty}$  for the values of  $\Gamma_s$ ,  $C_a$  values were calculated for 150 nm diameter spherical oil droplets and an oil volume fraction,  $\phi = 0.05$ . This analysis yielded approximate minimum nanoemulsion surfactant concentrations of 3.1 mg/mL (0.31 wt.%) for lecithin and 7.6 mg/mL (0.76 wt.%) for Tween 20. To quantify the measurable effect that surfactant concentration had on the interfacial rheology and kinetic stability of nanoemulsions, concentrations below  $C_a$  (0.25 wt.% lecithin and 0.25 wt.% Tween 20) and above  $C_a$  (0.35 wt.% lecithin and 1 wt.% Tween 20) were investigated.

### 2.2.3 Nanoemulsion Preparation

Nanoemulsions were prepared using a Branson<sup>TM</sup> digital sonifier. The sonifier was operated at 40% maximum intensity and sonics were applied for 2 second pulses for a total processing time of 3 minutes. Nanoemulsions were cooled during ultrasonic processing using an ice bath at 4 °C. A duplicate of each nanoemulsion was formulated to ensure reproducibility. Each nanoemulsion contained 5 wt.% oil dispersed in an aqueous citrate-phosphate buffer continuous phase, for a total emulsion mass of 20 g.

The effect of oil phase composition on the coarsening behavior of bulk nanoemulsions was investigated first. The composition of the oil phase within bulk nanoemulsions was varied by combining different mass ratios of our bioactive compound (carvacrol) and carrier oil (MCT) prior to emulsification (0, 5, 10, 20, 40, 60 and 80 wt.% carvacrol in MCT oil). Otherwise, a standardized oil phase composition (10 wt.% Carvacrol in MCT oil) was used to compare the effects of lecithin or Tween 20 adsorption on viscoelasticity and long-term stabilization behavior in bulk

nanoemulsions. Details on the determination of  $C_a$  for lecithin and Tween 20 are provided in Chapter 2.2.2. The nanoemulsion surfactant concentrations less than  $C_a$  were 0.25 wt.% lecithin or 0.25 wt.% Tween 20 and the concentrations greater than  $C_a$  were 0.35 wt.% lecithin or 1 wt.% Tween 20.

#### **2.2.4 Nanoemulsion Droplet Size Measurements**

The droplet properties analyzed in this study were average oil droplet size (Z-Ave) and  $\zeta$  potential, obtained after storage at 23 °C for 1, 7, 15, and 30 days using a Malvern® Zetasizer Nano ZS under standard operating conditions. Values are reported as averages  $\pm$  1 standard deviation (for  $n > 3$  measurements).

### **2.3 Results and Discussion**

#### **2.3.1 Effect of Oil Phase Composition and Surfactant Concentration on Initial Nanoemulsion Stability**

The composition of the oil phase and concentration of the surfactant in the aqueous phase were major contributors to the initial stability of nanoemulsions that contained carvacrol. Nanoemulsion instability manifested as the formation of a distinct lipid layer at the top of the container and a relatively clear, droplet-depleted aqueous layer at the bottom of the container. Nanoemulsions stabilized by 0.25 wt.% Tween 20, a concentration below its  $C_a$ , were highly unstable within the first 24 hours. When the concentration of carvacrol in the oil phase exceeded 10 wt.%, the formation of two distinct oil and aqueous phases begins to occur (Figure 2-3a). Nanoemulsions containing 1 wt.% Tween 20, a concentration above its  $C_a$ , appeared to be slightly more stable (Figure 2-3b). For these nanoemulsions, a distinct lipid layer at the top of the container also began to form when the concentration of carvacrol exceeded 10 wt.%. However, the bottom layer of the nanoemulsions remained relatively turbid until the concentration of carvacrol in the

oil phase exceeded 60 wt.%. Very low kinetic stability of nanoemulsions stabilized by Tween 20 has also been observed in the literature.<sup>22</sup>

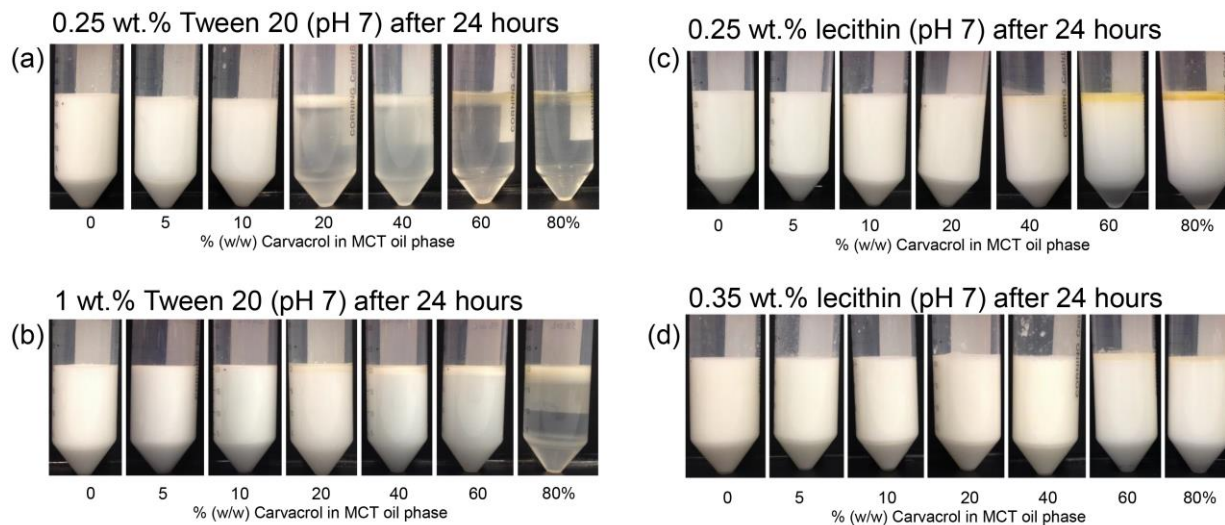


**Figure 2-3** Photographs taken 24 h after emulsification for oil-in-water nanoemulsions at pH 7 stabilized by (a) 0.25 wt.% Tween 20, (b) 1 wt.% Tween 20, (c) 0.25 wt.% lecithin or (d) 0.25 wt.% lecithin. Each emulsion contains 5 wt.% dispersed oil phase, with increasing amounts of carvacrol in MCT oil from left to right (0 (control), 5, 10, 20, 40, 60, 80 wt.% carvacrol).

Contrarily, nanoemulsions containing 0.25 wt. % lecithin, a concentration below its  $C_a$ , were notably more stable than Tween 20 nanoemulsions on all accounts. Nanoemulsions stabilized by lecithin did not form a visible lipid layer at the top of the container after 24 hours until the concentration of carvacrol in the oil phase exceeded 20 wt.%. Also, the bottom layer of these nanoemulsions remained turbid for each carvacrol concentrations investigated (Figure 2-3c). Furthermore, when the nanoemulsions contained 0.35 wt.% lecithin (above its  $C_a$ ), the stability of carvacrol containing nanoemulsions further increased. Nanoemulsions remained turbid for all carvacrol concentrations investigated and no visible lipid layer formed until the concentration of carvacrol exceeded 40 wt.% of the oil phase (Figure 2-3d).

The differences in kinetic stability seen between nanoemulsions containing surfactant concentrations below  $C_a$  to those above  $C_a$  may be partially due to a deficiency of surfactant in the aqueous phase that could adsorb to the large O/W interfacial areas generated during emulsification at surfactant concentrations below  $C_a$ . Generally, an excess of emulsifier is necessary because there is an equilibrium between emulsifier at the droplet surface and that in the continuous phase that must be achieved for adequate kinetic stability.<sup>41</sup>

A recent investigation of O/W nanoemulsions containing carvacrol attributed the rapid O/W phase separation to coalescence and Ostwald ripening mechanisms resulting from the addition of carvacrol.<sup>17</sup> Several studies have suggested that the high polarity and low interfacial tension of carvacrol (and similar compounds) accelerates the rate of emulsion droplet coalescence,<sup>17,18</sup> the process where colliding droplets merge together.<sup>42,48</sup> Likewise, nanoemulsions containing oils with some limited water solubility (*i.e.* carvacrol) have also been shown to be susceptible to Ostwald ripening,<sup>17,49</sup> the process where large droplets grow at the expense of smaller droplets due to the transport of mass through the aqueous continuous medium.<sup>13,17,49,50</sup> It has therefore been suggested that the presence of a non-polar, insoluble oil (*i.e.* MCT) decreases the rate of coalescence by decreasing the oil phase polarity and increasing the O/W interfacial tension<sup>17</sup> and inhibits Ostwald ripening due to an entropy of mixing effect.<sup>49,51–53</sup>

Indeed, the concentration of surfactant in the aqueous phase, relatively high polarity, low O/W interfacial tension, and limited water solubility of carvacrol molecules are likely attributable factors in the coalescence and Ostwald ripening of oil droplets and ultimately the macroscopic kinetic destabilization seen in these nanoemulsions. However, our interfacial rheometry results described in Chapter 2.3.2 indicate that the viscoelasticity of the surfactant-laden interfacial layer may also play a crucial role in the stabilization of nanoemulsion oil droplets.

### 2.3.2 Effect of Surfactant Concentration on Interfacial Viscoelasticity

The apparent viscoelastic moduli,  $E'$  and  $E''$ , were measured for an oil droplet in aqueous surfactant solutions at pH 7 and 3. The oil droplet was a mixture of carvacrol and MCT oil (10 wt.% carvacrol in MCT oil). The aqueous phase contained lecithin or Tween 20 at concentrations below and above their corresponding  $C_a$  values. It is important to note that all aqueous phase surfactant concentrations used in oscillating pendant drop experiments (0.25, 0.35 wt.% lecithin, or 0.25, 1 wt.% Tween 20) were much higher than the experimentally determined critical aggregation concentrations (CACs) for lecithin ( $\approx 0.008$  wt.%) and Tween 20 ( $\approx 0.01$  wt.%).

The concentration of the surfactant in the aqueous phase appeared to slightly influence the developed viscoelastic response of O/W interfaces containing lecithin after 24 hours. When the concentration of surfactant in the aqueous phase (pH 7) was increased from 0.25 wt.% lecithin (Figure 2-4a) to 0.35 wt.% lecithin (Figure 2-5a), the apparent  $E'$  value after 24 hours increased by ca. 13%. Similar viscoelastic behavior was seen for aqueous lecithin solutions at pH 3. When the concentration of lecithin was increased from 0.25 wt.% lecithin (Figure 2-4b) to 0.35 wt.% lecithin (Figure 2-5b), the developed  $E'$  value increased by ca. 28%. Conversely, the developed viscoelastic response for O/W interfaces containing Tween 20 appeared to be insensitive to surfactant concentration in the aqueous phase (at pH 7 and 3). Values for  $E'$  and  $E''$  remained unchanged when the concentration was increased from 0.25 wt.% Tween 20 to 1 wt.% Tween 20.

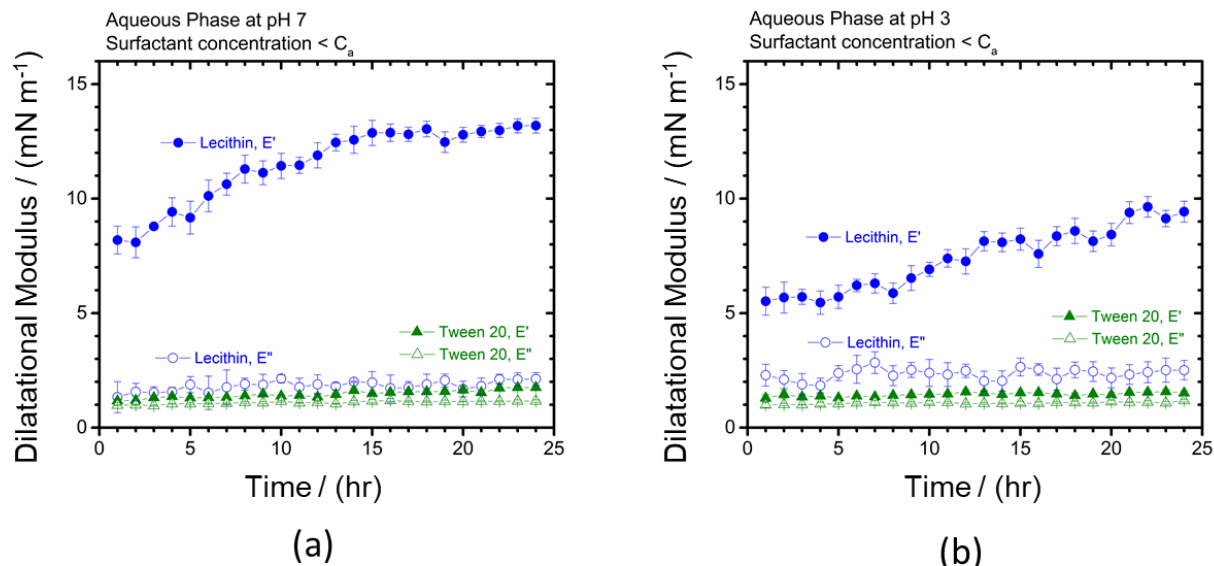


**Figure 2-4** Evolution of the viscoelastic moduli,  $E'$  and  $E''$ , over 24 h for 0.25 wt.% Lecithin and 0.25 wt.% Tween 20 stabilized O/W interfaces at (a) pH 7 and (b) pH 3. The aqueous phase contained the emulsifier, while the oil phase had a composition of 10 wt.% carvacrol in MCT oil. Oscillations were conducted at a frequency of 0.01 Hz. Lines simply connect data points to aid the eye.

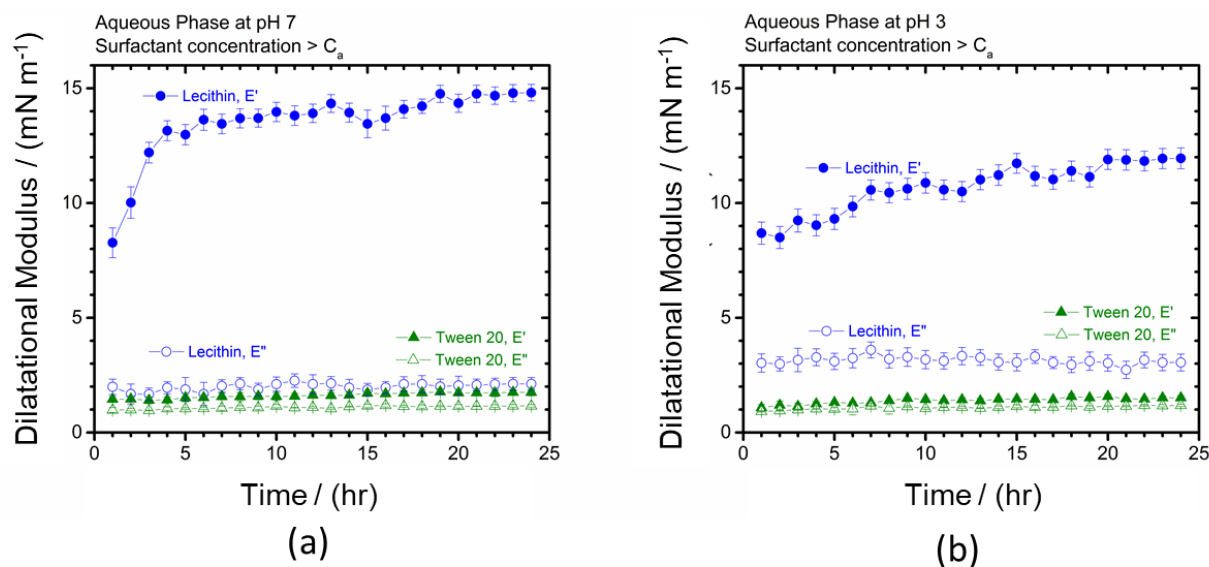


**Figure 2-5** Evolution of the viscoelastic moduli,  $E'$  and  $E''$ , over 24 h for 0.35 wt.% Lecithin and 1 wt.% Tween 20 stabilized O/W interfaces at (a) pH 7 and (b) pH 3. The aqueous phase contained the emulsifier, while the oil phase had a composition of 10 wt.% carvacrol in MCT oil. Oscillations were conducted at a frequency of 0.01 Hz. Lines simply connect data points to aid the eye.

In all interfacial rheological measurements of surfactant-laden interfaces, the applied area strain was small (2%) and rate of interfacial area deformation was low (0.01 Hz). Also, the concentrations of surfactant in the aqueous phase relative to the CACs for lecithin and Tween 20 were several orders of magnitude higher. Therefore, the variations in the viscoelastic response (or lack thereof) resulting from increases in surfactant concentration in the aqueous phase were believed not to be a result of Marangoni stresses, where surfactant concentration gradients in the interface lead to non-uniform interfacial tension contributions.

The slight increase in the elastic storage modulus,  $E'$ , when the concentration of lecithin was increased from 0.25 to 0.35 wt.% was presumably due to accumulation of lecithin molecules near the O/W interface and the further development of a rigid, two-dimensional layer of lecithin molecules in the aqueous sub-phase. As stated in the literature, lecithin is believed to form a thick viscoelastic film that is strengthened by hydrogen bonding between phosphate groups on neighboring molecules.<sup>21</sup> On the other hand, Tween 20 molecules are non-ionic, and thus lack the ability to form a strongly associated network with neighboring molecules. Therefore, a very low resistance to interfacial deformation (i.e. a low viscoelastic response) was seen for each O/W interface containing 0.25 and 1 wt. % Tween 20.

### **2.3.3 Effect of pH on Interfacial Viscoelasticity**

The pH of the aqueous phase markedly contributed to the apparent viscoelastic response developed after 24 hours for O/W interfaces containing lecithin. For aqueous solutions containing 0.25 wt.% lecithin, shifting the pH from 7 to 3 decreased  $E'$  by ca. -28% (Figure 2-4). Similarly, for aqueous solutions containing 0.35 wt.% lecithin, shifting the aqueous phase pH from 7 to 3 decreased  $E'$  by ca. -19% (Figure 2-5).

In previous studies,<sup>54,55</sup> the surface mechanics of insoluble monolayers formed by phosphatidylcholine molecules at the air-water interface were investigated at pH 9, 7, and 5. The explicit underlying assumption in these studies was that all spread phospholipid molecules remained at the air-water interface during relaxation experiments. The authors created uniform phospholipid monolayers by direct spreading of phosphatidylcholine molecules at the air-water interface using a volatile solvent. With this process, the concentration of phosphatidylcholine molecules in the aqueous sub-phase was essentially zero, as all spread surfactant molecules adsorbed to and strongly remained at the air-water interface during rheological investigation. The authors stated that the presence of surfactant aggregates in the aqueous sub-phase may lead to desorption/readsorption of surfactant molecules from/to the interface during relaxation experiments, which would have a noticeable impact on the observed interfacial viscoelastic behavior.<sup>54</sup>

In the current study, the interfacial systems investigated contained aqueous phases with high surfactant concentrations (and thus surfactant aggregates) in the bulk aqueous phase. The presence of surfactant aggregates in the aqueous sub-phase allows the surfactant molecules to readily adsorb/desorb to accommodate interfacial dilatational fluctuations. It is believed that at pH 7, the tendency for desorption/readsorption of phospholipids from/to the oil-water interface is relatively low due to strong attractive van der Waals interactions (hydrogen-bonding) between phospholipids and surrounding molecules provided by the ionized phosphate moieties within phospholipid head-groups, and thus the measured elastic response of the interface is high.

However, at pH 3, it is believed the desorption/readsorption tendency is slightly more pronounced due to a net increase in the repulsive electrostatic interactions between phospholipids. Presumably, this behavior is due to the protonation of the negatively charged phosphate moieties

(which begins to occur near pH 3<sup>56</sup>) and the domination of repulsive interactions originating from the positively charged choline and ethanolamine moieties of PC and PE, respectively. Thus, surfactant desorption/adsorption would occur more easily at low pH for these systems and would in turn lead to the decrease in the elastic response of the surfactant stabilized interface observed in this study.

Contrarily, the developed viscoelastic response after 24 hours for Tween 20 monolayers was very low overall and less sensitive to the pH of the aqueous phase. Adjusting the aqueous phase pH from 7 to 3 slightly decreased the O/W interface's (very low) viscoelastic response. For aqueous solutions containing 0.25 wt.% Tween 20, adjusting the pH from 7 to 3 decreased  $E'$  by ca. -11% (Figure 2-4). Likewise, when the aqueous phase contained 0.35 wt.% Tween 20, shifting the pH from 7 to 3 decreased  $E'$  by ca. -7% (Figure 2-5).

The very low viscoelastic response overall for interfaces stabilized by Tween 20 may be because these systems also contained high concentrations of surfactant in the bulk aqueous phase which would allow desorption/readsorption of surfactant molecules from/to the interface during relaxation experiments. Furthermore, the tendency for desorption/readsorption would be magnified by the nonionic nature of Tween 20 molecules and the lack of a strongly associated surfactant network to act as a barrier for surfactant desorption/readsorption from/to the interface in response to imposed dilatational strains for each pH investigated.

In general, shifting the pH of the aqueous phase from neutral to acidic notably decreased the interfacial elasticity of O/W interfaces containing zwitterionic lecithin molecules, and to a much lesser extent for O/W interfaces containing non-ionic Tween 20 molecules. However, upon analysis of the evolution of nanoemulsion size distributions and change in Z-Ave droplet diameter over 30 days (discussed in Chapter 2.3.4), there was no apparent correlation between the pH of the

aqueous phase and the extended stability of the bulk surfactant-stabilized nanoemulsions. Therefore, the pH of the aqueous was determined to not be a primary contributor to the extended stability of bulk nanoemulsions (Table 2-1).

**Table 2-1** Z-Ave oil droplet diameters collected on Day 1 and Day 30 for lecithin and Tween 20 nanoemulsions at pH 7 and 3. Each system had a dispersed oil phase that contained 10 wt.% carvacrol in MCT oil (0.05 wt.% carvacrol overall). Data are reported for nanoemulsions with lecithin or Tween 20 concentrations less than and greater than  $C_a$ . Values are reported as averages  $\pm$  1 standard deviation ( $n > 3$ ).

	Nanoemulsions containing Tween 20					Nanoemulsions containing Lecithin				
	Concentration	pH	Day 1	Day 30	% Increase (time)	Concentration	pH	Day 1	Day 30	% Increase (time)
Z-Ave Diameter (nm)	0.25 wt.%	7	159 $\pm$ 5	956 $\pm$ 73	500	0.25 wt.%	7	201 $\pm$ 3	248 $\pm$ 5	23
		3	241 $\pm$ 3	584 $\pm$ 76	142		3	205 $\pm$ 2	218 $\pm$ 4	6
	1 wt.%	7	232 $\pm$ 2	569 $\pm$ 81	145	0.35 wt.%	7	142 $\pm$ 2	151 $\pm$ 1	6
		3	228 $\pm$ 2	558 $\pm$ 69	145		3	196 $\pm$ 1	212 $\pm$ 2	8

### 2.3.4 Correlation Between Dilatational Viscoelasticity and Nanoemulsion Stability

The viscoelastic response of O/W interfaces after 24 hours was shown to correlate with the extended kinetic stability of bulk nanoemulsions. For the O/W interface containing 0.25 wt.% Tween 20, a concentration below its  $C_a$  (Figure 2-4), a very low viscoelastic response was observed. Similarly, a low viscoelastic response was also observed for the O/W interface containing 1 wt.% Tween 20, a concentration above its  $C_a$  (Figure 2-5). Previous research on foam bubbles<sup>57</sup> and emulsion droplets<sup>58</sup> has indicated that interfacial films with low elasticity and electrical potential are susceptible to the development of bimodal droplet size distributions over time through the mechanism of Ostwald ripening.<sup>57,58</sup>

This behavior was evident in the droplet size distributions of O/W nanoemulsions containing 0.25 wt.% Tween 20 at pH 7 (Figure 2-6a) and pH 3 (Figure 2-7a), as well as those containing 1 wt.% Tween 20 at pH 7 (Figure 2-6b) and pH 3 (Figure 2-7b). Over 30 days, the nanoemulsion droplet size distributions consistently transitioned from monomodal to biomodal. Furthermore, for all nanoemulsions containing Tween 20, the Z-Ave droplet diameters of oil droplets increased by a least 140% over 30 days of storage (Figure 2-8). Analysis of the droplet  $\zeta$  potential 24 hours after formulation (Table 2-2) for pH 7 nanoemulsions containing 0.25 wt.% Tween 20 yielded near zero values of ca. +1.1 mV and those at a concentration of 1 wt.% Tween 20 also yielded relatively low values of ca. +1.3 mV. Very similar  $\zeta$  potential values were also observed when the pH was shifted from 7 to 3 (Table 2-2).

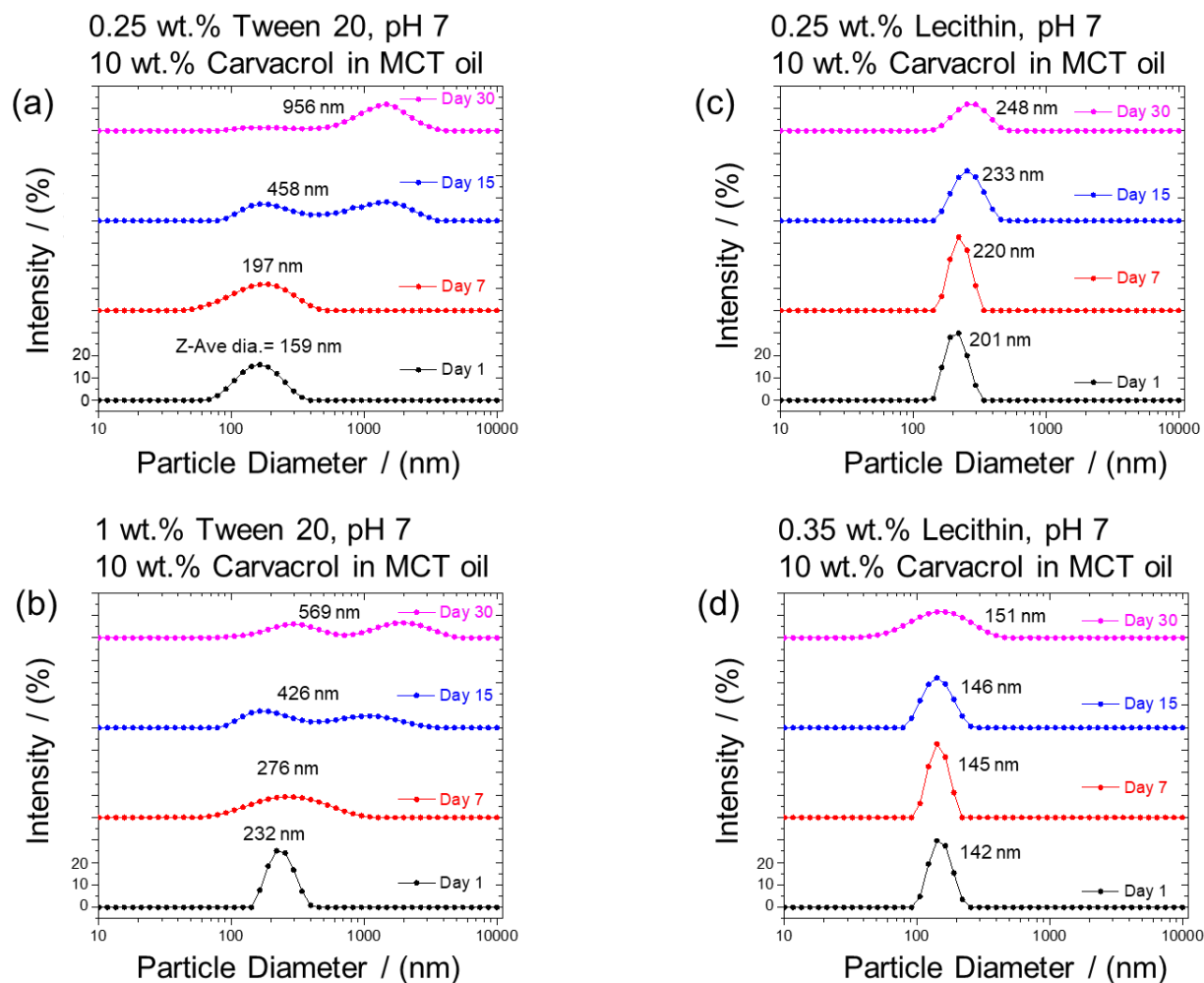


**Figure 2-6** Intensity size distributions over 30 days for oil-in-water emulsions that contained 5 wt.% oil (10 wt.% carvacrol in MCT oil) stabilized by (a) 0.25 wt.% Tween 20, (b) 1 wt.% Tween 20, (c) 0.25 wt.% lecithin or (d) 0.35 wt.% lecithin at pH 7. Data were offset from zero to illustrate size distribution changes over time.

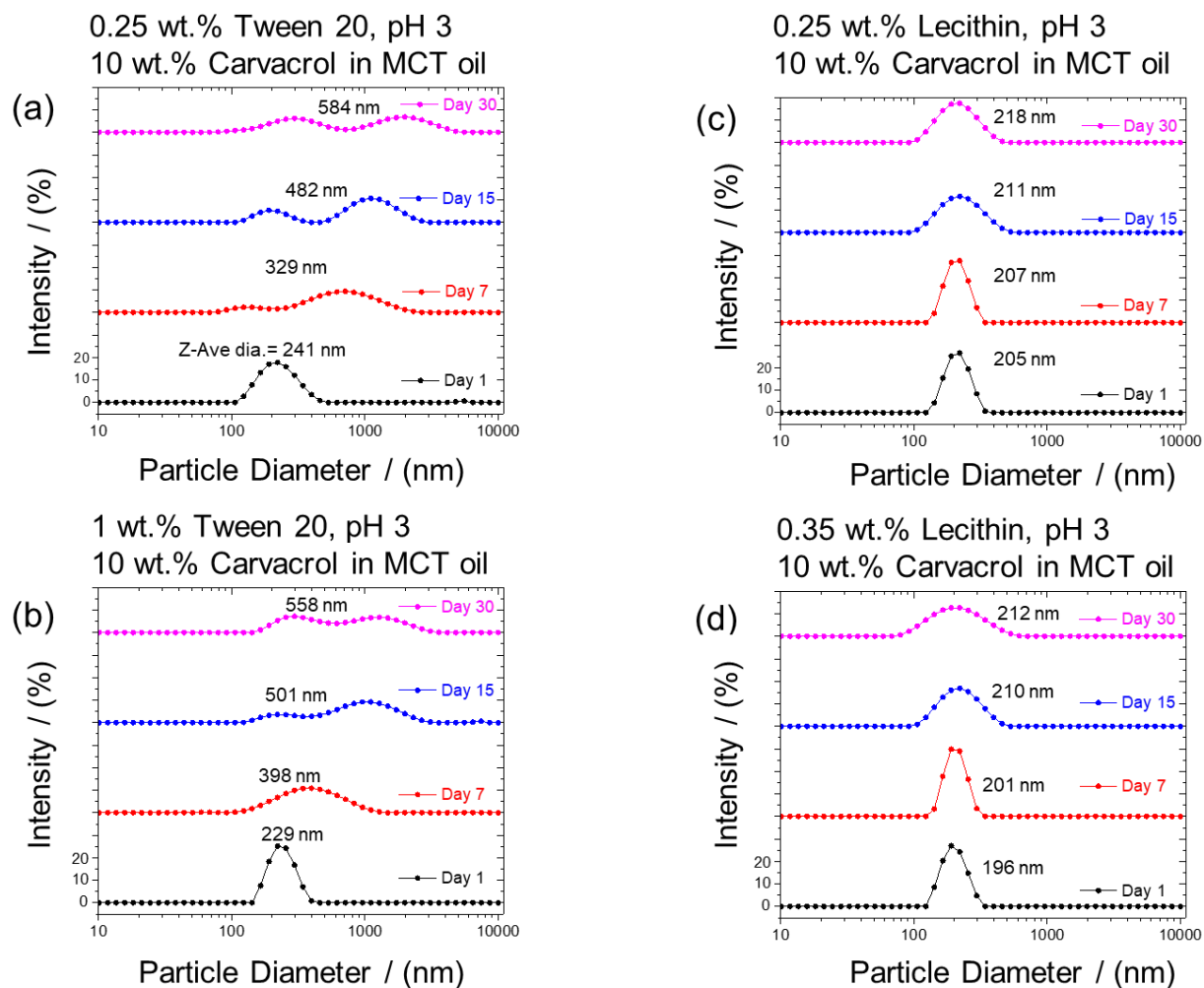


**Figure 2-7** Intensity size distributions over 30 days for oil-in-water emulsions that contained 5 wt.% oil (10 wt.% carvacrol in MCT oil) stabilized by (a) 0.25 wt.% Tween 20, (b) 1 wt.% Tween 20, (c) 0.25 wt.% lecithin or (d) 0.35 wt.% lecithin at pH 3. Data were offset from zero to illustrate size distribution changes over time.

**Table 2-2** Zeta ( $\zeta$ ) potential measurements collected on Day 1 and Day 30 for lecithin and Tween 20 nanoemulsions at pH 7 and 3. Each system had a dispersed oil phase that contained 10 wt.% carvacrol in MCT oil (0.05 wt.% carvacrol overall). Data are reported for nanoemulsions with lecithin or Tween 20 concentrations less than and greater than  $C_a$ . Values are reported as averages  $\pm$  1 standard deviation ( $n > 3$ ).

	Nanoemulsions containing Tween 20				Nanoemulsions containing Lecithin			
	Concentration	pH	Day 1	Day 30	Concentration	pH	Day 1	Day 30
$\zeta$ potential / (mV)	0.25 wt.%	7	$1.1 \pm 0.1$	$1.2 \pm 0.1$	0.25 wt.%	7	$-33.9 \pm 0.4$	$-32.4 \pm 1.9$
		3	$1.0 \pm 0.2$	$0.8 \pm 0.3$		3	$-51.8 \pm 0.1$	$-51.9 \pm 0.3$
	1 wt.%	7	$1.3 \pm 0.2$	$1.4 \pm 0.1$	0.35 wt.%	7	$-36.9 \pm 0.9$	$-38.9 \pm 0.2$
		3	$0.9 \pm 0.1$	$0.9 \pm 0.2$		3	$-48.9 \pm 0.4$	$-56.9 \pm 0.5$

Contrary to the interfacial layer formed by non-ionic Tween 20 molecules, the layer formed by lecithin molecules was highly viscoelastic. This translated to greatly improved extended stability of nanoemulsions stabilized by lecithin. For nanoemulsions containing 0.25 wt.% lecithin at pH 7, the increase in droplet diameter was relatively small over the course of 30 days, increasing by 23% (Figure 2-8). Shifting the aqueous phase pH down to 3 reduced the change in oil droplet diameter over time, yielding increases of only ca. 6% after 30 days. Changing the pH of the aqueous phase also appeared to slightly affect the initial Z-Ave diameter of nanoemulsions containing 0.35 wt.% lecithin. At pH 7, the initial diameter of oil droplets was ca. 142 nm; however, when the aqueous phase pH was decreased to pH 3 at this surfactant concentration, the initial diameter of oil droplets increased to ca. 196 nm. Increases in droplet diameter over time remained small, however, increasing by ca. 8% after 30 days.

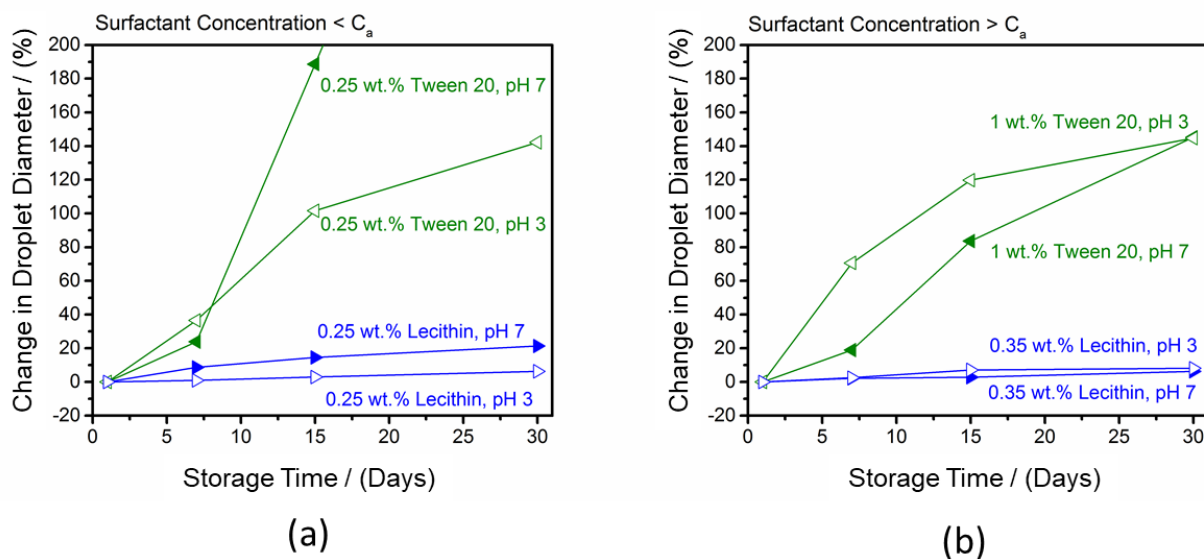


**Figure 2-8** Visualization of the % change in droplet Z-Ave diameter over 30 days for Tween 20 and lecithin stabilized nanoemulsions at surfactant concentrations (a) below and (b) above their corresponding  $C_a$  values. The oil phase made up 5 wt.% of the total nanoemulsion (10 wt.% carvacrol in MCT oil). Lines simply connect data points to aid the eye.

The dependence of initial droplet diameter on pH may be due to a change in the optimum curvature of the surfactant at the O/W interface as a result of a change in the sub-phase pH, as discussed in the literature.<sup>41,59,60</sup> This is supported by the behavior seen in the  $\zeta$  potential measurements of lecithin-stabilized nanoemulsions over 30 days. Lecithin molecules adsorbed to O/W interface formed monolayers with relatively high  $\zeta$  potential. For the nanoemulsions containing 0.25 wt.% lecithin at pH 7, the initial  $\zeta$  potential values were ca. -34 mV. Likewise, for nanoemulsions containing 0.35 wt.% lecithin at pH 7, the  $\zeta$  potential values were ca. -37 mV after 24 hours, comparable to the values found by other researchers.<sup>61</sup> When the pH of the aqueous phase was shifted to 3 for nanoemulsions containing 0.25 wt.% lecithin, there was a noticeable increase in the magnitude of the initial  $\zeta$  potential to ca. -52 mV. Likewise, when the pH was shifted to 3 for nanoemulsions containing 0.35 wt. % lecithin, the magnitude of the initial  $\zeta$  potential increased to ca. -49 mV. This correlated well with observed increase in initial Z-Ave droplet diameter of lecithin-stabilized nanoemulsions under acidic (pH 3) conditions, compared to those in a neutral environment (pH 7). Presumably, protonation of the phosphate ion in zwitterionic lecithin molecules would increase the overall ionization of these molecules and simultaneously change the optimum curvature of these molecules at the O/W interface. An increase in the number of adsorbed negative ions at the O/W interface would cause the increase in the magnitude of measured  $\zeta$  potential. Likewise, the change in optimum curvature of lecithin molecules at the interface would result in the observed increase in initial oil droplet diameter.

Generally, the nanoemulsions stabilized by Tween 20 were anticipated to have poor extended stability due to the absence of a strongly associated viscoelastic network of surfactant molecules at the O/W interface and low electrostatic stabilization between oil droplets. These properties likely led to the high susceptibility of Tween 20 stabilized nanoemulsions to

destabilization mechanisms involving interfacial deformation (i.e. coalescence). This behavior was supported by data showing the consistent formation of a bimodal droplet size distribution in Tween 20 stabilized nanoemulsion over 30 days. However, nanoemulsions stabilized by lecithin were anticipated to be relatively more stable due to the formation of oil droplets with high interfacial viscoelasticity and electrical potential. These predictions were confirmed in the analysis of the oil droplet size for these nanoemulsions, which revealed the continuation of monomial size distributions over the storage time investigated, agreeing well with other researchers.<sup>58</sup> This information potentially illustrates that the extended kinetic stabilization of nanoemulsion delivery systems is closely related to the physicochemical properties of the bulk nanoemulsion, as well as the mechanical properties of the interfacial layer.

## **2.4 Summary**

This investigation demonstrates that the formation of surfactant-laden interfacial layer with high viscoelasticity may provide additional benefits in food-based O/W nanoemulsion delivery systems. This study also supports the use of oscillating pendant drop tensiometry as a viable methodology for predicting the kinetic stability of nanoemulsions, which can be used in parallel with other nanoemulsion characterization analyses. Pendant drop results indicated that the O/W interface containing lecithin displayed much higher viscoelasticity than interfaces containing Tween 20, possibly due to strong chemical association between lecithin and adjacent molecules. This phenomenon correlated well with stability of nanoemulsions containing carvacrol, such as the nanoemulsion's resistance to droplet size increases and the formation of a bimodal droplet size distribution over time.

Past studies have ultimately determined that there is not always a direct correlation between measured shear or dilatational interfacial rheology and emulsion stability.<sup>19,20</sup> It has been found,

however, that interfaces with highly elastic or gelled structures reduce the overall magnitude of deformation that a droplet encounters due to external forces.<sup>62,63</sup> The results in this work indicate that the resistance to interfacial deformation displayed by lecithin-stabilized interface may contribute to the highly stable bulk nanoemulsion characteristics, in terms of resistance to increases in Z-Ave droplet diameter and the formation of a bimodal size distribution.

This information is potentially very useful for the fabrication of stable nanoemulsion-based delivery systems containing other antimicrobial and flavor compounds with similar chemical architectures to carvacrol (*i.e.*, thymol and menthol); however, due to the differences in physicochemical properties of these compounds, detailed analyses of such systems would be required for specific determination of the extended nanoemulsion stability. The techniques provided in this work also give insight into the interfacial criteria for selecting appropriate emulsifiers to use in nanoemulsion-based delivery systems containing food grade compounds.

## 2.5 References

- (1) Donsì, F.; Annunziata, M.; Vincensi, M.; Ferrari, G. Design of Nanoemulsion-Based Delivery Systems of Natural Antimicrobials: Effect of the Emulsifier. *J. Biotechnol.* **2012**, *159* (4), 342–350. <https://doi.org/10.1016/j.jbiotec.2011.07.001>.
- (2) Chang, Y.; Mclandsborough, L.; McClements, D. J. Physical Properties and Antimicrobial Efficacy of Thyme Oil Nanoemulsions: Influence of Ripening Inhibitors. *J. Agric. Food Chem.* **2012**, *60*, 12056–12063. <https://doi.org/10.1021/jf402147p>.
- (3) Ultee, A.; Bennik, M. H. J.; Moezelaar, R. The Phenolic Hydroxyl Group of Carvacrol Is Essential for Action against the Food-Borne Pathogen *Bacillus Cereus*. *Appl. Environ. Microbiol.* **2002**, *68* (4), 1561–1568. <https://doi.org/10.1128/AEM.68.4.1561>.
- (4) Lagouri, V.; Blekas, G.; Tsimidou, M.; Kokkini, S.; Boskou, D. Composition and Antioxidant Activity of Essential Oils from Oregano Plants Grown Wild in Greece. *Zeitschrift für Lebensmittel- und Futtermittelwissenschaften* **1993**, *197* (1), 20–23. <https://doi.org/10.1007/BF01202694>.
- (5) Arrebola, M. L.; Navarro, M. C.; Jiménez, J.; Ocaña, F. A. Yield and Composition of the Essential Oil of *Thymus Serpylloides* Subsp. *Serpylloides*. *Phytochemistry* **1994**, *36* (1), 67–72. [https://doi.org/10.1016/S0031-9422\(00\)97014-6](https://doi.org/10.1016/S0031-9422(00)97014-6).
- (6) Cosentino, S.; Tuberoso, C. I. G.; Pisano, B.; Satta, M.; Mascia, V.; Arzedi, E.; Palmas, F. In-Vitro Antimicrobial Activity and Chemical Composition of Sardinian *Thymus* Essential Oils. *Lett. Appl. Microbiol.* **1999**, *29* (2), 130–135. <https://doi.org/10.1046/j.1472-765X.1999.00605.x>.
- (7) Kim, J.; Marshall, M. R.; Wei, C. Antibacterial Activity of Some Essential Oil Components against Five Foodborne Pathogens. *J. Agric. Food Chem.* **1995**, *43* (0021), 2839–2845. <https://doi.org/10.1021/jf00059a013>.
- (8) Gallucci, M. N.; Oliva, M.; Casero, C.; Dambolena, J.; Luna, A.; Zygadlo, J.; Demo, M. Antimicrobial Combined Action of Terpenes against the Food-Borne Microorganisms *Escherichia Coli*, *Staphylococcus Aureus* and *Bacillus Cereus*. *Flavour Fragr. J.* **2009**, *24* (6), 348–354. <https://doi.org/10.1002/ffj.1948>.
- (9) Griffin, S. G.; Wyllie, S. G.; Markham, J. L.; Leach, D. N. The Role of Structure and Molecular Properties of Terpenoids in Determining Their Antimicrobial Activity. *Flavour Fragr. J.* **1999**, *14* (5), 322–332. [https://doi.org/10.1002/\(SICI\)1099-1026\(199909/10\)14:5<322::AID-FFJ837>3.0.CO;2-4](https://doi.org/10.1002/(SICI)1099-1026(199909/10)14:5<322::AID-FFJ837>3.0.CO;2-4).
- (10) Ait-Ouazzou, A.; Espina, L.; Gelaw, T. K.; De Lamo-Castellví, S.; Pagán, R.; García-Gonzalo, D. New Insights in Mechanisms of Bacterial Inactivation by Carvacrol. *J. Appl. Microbiol.* **2013**, *114* (1), 173–185. <https://doi.org/10.1111/jam.12028>.

- (11) Ben Arfa, A.; Combes, S.; Preziosi-Belloy, L.; Gontard, N.; Chalier, P. Antimicrobial Activity of Carvacrol Related to Its Chemical Structure. *Lett. Appl. Microbiol.* **2006**, *43* (2), 149–154.
- (12) McClements, D. J.; Decker, E. A.; Weiss, J. Emulsion-Based Delivery Systems for Lipophilic Bioactive Components. *J. Food Sci.* **2007**, *72* (8), 109–124. <https://doi.org/10.1111/j.1750-3841.2007.00507.x>.
- (13) McClements, D. J. Edible Nanoemulsions: Fabrication, Properties, and Functional Performance. *Soft Matter* **2011**, *7* (6), 2297. <https://doi.org/10.1039/c0sm00549e>.
- (14) Weiss, J.; Gaysinsky, S.; Davidson, M.; McClements, J. *Nanostructured Encapsulation Systems: Food Antimicrobials*; 2009. <https://doi.org/10.1016/B978-0-12-374124-0.00024-7>.
- (15) Gaysinsky, S.; Davidson, P. M.; Bruce, B. D.; Weiss, J. Growth Inhibition of Escherichia Coli O157:H7 and Listeria Monocytogenes by Carvacrol and Eugenol Encapsulated in Surfactant Micelles. *J. Food Prot.* **2005**, *68* (12), 2559–2566.
- (16) Ultee, A.; Kets, E. P. W.; Smid, E. J. Mechanisms of Action of Carvacrol on the Food-Borne Pathogen Bacillus Cereus. *Appl. Environ. Microbiol.* **1999**, *65* (10), 4606–4610.
- (17) Chang, Y.; Mclandsborough, L.; McClements, D. J. Physicochemical Properties and Antimicrobial Efficacy of Carvacrol Nanoemulsions Formed by Spontaneous Emulsification. *J. Agric. Food Chem.* **2013**, *61*, 8906–8913. <https://doi.org/10.1021/jf402147p>.
- (18) Chanamai, R.; Horn, G.; McClements, D. J. Influence of Oil Polarity on Droplet Growth in Oil-in-Water Emulsions Stabilized by a Weakly Adsorbing Biopolymer or a Nonionic Surfactant. *J. Colloid Interface Sci.* **2002**, *247* (1), 167–176. <https://doi.org/10.1006/jcis.2001.8110>.
- (19) Erni, P.; Windhab, E. J.; Fischer, P. Interfacial Rheology in Food Science and Technology. In *Interfacial Rheology*; Liggieri, L., Miller, R., Eds.; CRC Press, 2009; pp 615–644. <https://doi.org/10.1163/ej.9789004175860.i-684>.
- (20) Erni, P. Deformation Modes of Complex Fluid Interfaces. *Soft Matter* **2011**, *7* (17), 7586. <https://doi.org/10.1039/c1sm05263b>.
- (21) Shchipunov, Y. a. Lecithin Organogel: A Micellar System with Unique Properties. *Colloids Surfaces A Physicochem. Eng. Asp.* **2001**, *183–185*, 541–554. [https://doi.org/10.1016/S0927-7757\(01\)00511-8](https://doi.org/10.1016/S0927-7757(01)00511-8).
- (22) Dickinson, E.; Goller, M. I.; Wedlock, D. J. Creaming and Rheology of Emulsions Containing Polysaccharide and Non-Ionic or Anionic Surfactants. *Colloids Surfaces A Physicochem. Eng. Asp.* **1993**, *75* (C), 195–201. [https://doi.org/10.1016/0927-7757\(93\)80430-M](https://doi.org/10.1016/0927-7757(93)80430-M).

- (23) Dickinson, E. *An Introduction to Food Colloids*; Oxford Science Publishers, 1992.
- (24) McClements, D. J. Critical Review of Techniques and Methodologies for Characterization of Emulsion Stability. *Crit. Rev. Food Sci. Nutr.* **2007**, *47* (7), 611–649. <https://doi.org/10.1080/10408390701289292>.
- (25) McClements, D. J. *Food Emulsions Principles, Practices, and Techniques*; CRC Press, 2005. <https://doi.org/10.1093/acprof:oso/9780195383607.003.0002>.
- (26) Gupta, A.; Eral, H. B.; Hatton, T. A.; Doyle, P. S. Nanoemulsions: Formation, Properties and Applications. *Soft Matter* **2016**, *12* (11), 2826–2841. <https://doi.org/10.1039/C5SM02958A>.
- (27) Kirby, S. M.; Anna, S. L.; Walker, L. M. Sequential Adsorption of an Irreversibly Adsorbed Nonionic Surfactant and an Anionic Surfactant at an Oil/Aqueous Interface. *Langmuir* **2015**, *31* (14), 4063–4071. <https://doi.org/10.1021/la504969v>.
- (28) Eastoe, J.; Nave, S.; Downer, A.; Paul, A.; Rankin, A.; Penfold, J. Adsorption of Ionic Surfactants at the Air - Solution Interface. *Langmuir* **2000**, *16* (25), 4511–4518. <https://doi.org/10.1021/la991564n>.
- (29) Seredyuk, V.; Alami, E.; Nydén, M.; Holmberg, K.; Peresyphkin, A. V.; Menger, F. M. Adsorption of Zwitterionic Gemini Surfactants at the Air-Water and Solid-Water Interfaces. *Colloids Surfaces A Physicochem. Eng. Asp.* **2002**, *203* (1–3), 245–258. [https://doi.org/10.1016/S0927-7757\(01\)01106-2](https://doi.org/10.1016/S0927-7757(01)01106-2).
- (30) Hines, J. D.; Garrett, P. R.; Rennie, G. K.; Thomas, R. K.; Penfold, J. Structure of an Adsorbed Layer of n -Dodecyl- N , N -Dimethylamino Acetate at the Air/Solution Interface As Determined by Neutron Reflection. *J. Phys. Chem. B* **1997**, *101* (36), 7121–7126. <https://doi.org/10.1021/jp9711959>.
- (31) Capek, I. Degradation of Kinetically-Stable o/w Emulsions. *Adv. Colloid Interface Sci.* **2004**, *107* (2–3), 125–155. [https://doi.org/10.1016/S0001-8686\(03\)00115-5](https://doi.org/10.1016/S0001-8686(03)00115-5).
- (32) Li, Y.; Le Maux, S.; Xiao, H.; McClements, D. J. Emulsion-Based Delivery Systems for Tributyrin, a Potential Colon Cancer Preventative Agent. *J. Agric. Food Chem.* **2009**, *57* (19), 9243–9249. <https://doi.org/10.1021/jf901836f>.
- (33) Nostro, A.; Roccaro, A. S.; Bisignano, G.; Marino, A.; Cannatelli, M. A.; Pizzimenti, F. C.; Cioni, P. L.; Procopio, F.; Blanco, A. R. Effects of Oregano, Carvacrol and Thymol on Staphylococcus Aureus and Staphylococcus Epidermidis Biofilms. *J. Med. Microbiol.* **2007**, *56* (4), 519–523. <https://doi.org/10.1099/jmm.0.46804-0>.
- (34) Kabalnov, A. S.; Shchukin, E. D. Ostwald Ripening Theory: Applications to Fluorocarbon Emulsion Stability. *Adv. Colloid Interface Sci.* **1992**, *38* (C), 69–97. [https://doi.org/10.1016/0001-8686\(92\)80043-W](https://doi.org/10.1016/0001-8686(92)80043-W).

- (35) Wooster, T. J.; Golding, M.; Sanguansri, P. Impact of Oil Type on Nanoemulsion Formation and Ostwald Ripening Stability. *Langmuir* **2008**, *24* (22), 12758–12765. <https://doi.org/10.1021/la801685v>.
- (36) Ziani, K.; Chang, Y.; McLandsborough, L.; McClements, D. J. Influence of Surfactant Charge on Antimicrobial Efficacy of Surfactant-Stabilized Thyme Oil Nanoemulsions. *J. Agric. Food Chem.* **2011**, *59* (11), 6247–6255. <https://doi.org/10.1021/jf200450m>.
- (37) Rodríguez Niño, M. R.; Lucero, A.; Rodríguez Patino, J. M. Relaxation Phenomena in Phospholipid Monolayers at the Air-Water Interface. *Colloids Surfaces A Physicochem. Eng. Asp.* **2008**, *320* (1–3), 260–270. <https://doi.org/10.1016/j.colsurfa.2008.02.008>.
- (38) Lucero Caro, A.; Rodríguez Niño, M. R.; Rodríguez Patino, J. M. The Effect of PH on Surface Dilatational and Shear Properties of Phospholipid Monolayers. *Colloids Surfaces A Physicochem. Eng. Asp.* **2008**, *327* (1–3), 79–89. <https://doi.org/10.1016/j.colsurfa.2008.06.007>.
- (39) Marsh, D. *Handbook of Lipid Bilayers*; 2013. <https://doi.org/10.1201/b11712>.
- (40) Georgieva, D.; Cagna, A.; Langevin, D. Link between Surface Elasticity and Foam Stability. *Soft Matter* **2009**, *5* (10), 2063. <https://doi.org/10.1039/b822568k>.
- (41) Meinders, M. B. J.; Kloek, W.; van Vliet, T. Effect of Surface Elasticity on Ostwald Ripening in Emulsions. *Langmuir* **2001**, *17* (13), 3923–3929. <https://doi.org/10.1021/la000304z>.
- (42) Tadros, T. F. *Surfactants in Pharmaceutical Formulations*; 2005. <https://doi.org/10.1002/3527604812.ch13>.
- (43) Piorkowski, D. T.; McClements, D. J. Beverage Emulsions: Recent Developments in Formulation, Production, and Applications. *Food Hydrocoll.* **2013**, *42*, 5–41. <https://doi.org/10.1016/j.foodhyd.2013.07.009>.
- (44) Xue, J.; Zhong, Q. Thyme Oil Nanoemulsions Coemulsified by Sodium Caseinate and Lecithin. *J. Agric. Food Chem.* **2014**, *62* (40), 9900–9907. <https://doi.org/10.1021/jf5034366>.
- (45) Erni, P.; Fischer, P.; Windhab, E. J. Sorbitan Tristearate Layers at the Air/Water Interface Studied by Shear and Dilatational Interfacial Rheology. *Langmuir* **2005**, *21* (23), 10555–10563. <https://doi.org/10.1021/la0514664>.
- (46) Erni, P.; Windhab, E. J.; Fischer, P. Emulsion Drops with Complex Interfaces: Globular versus Flexible Proteins. *Macromol. Mater. Eng.* **2011**, *296* (3–4), 249–262. <https://doi.org/10.1002/mame.201000290>.

## CHAPTER 3      ADSORPTION, DILATATIONAL RHEOLOGY, AND EMULSION STABILIZATION OF SiO<sub>2</sub>-DPPC COMPLEXES AT THE OIL-WATER INTERFACE

Portions of the following chapter contain text and figures adapted from the article, “Adsorption, Dilatational Rheology, and Emulsion Stabilization of SiO<sub>2</sub>-DPPC Complexes at the Oil-Water Interface,” with permission from **J.J. Nash** and K.A. Erk, which has been submitted for publication.

### 3.1 Introduction

Recent advances in the production of pharmaceutical compounds has led to a large proportion (> 40%) of newly developed pharmaceuticals being lipophilic in character.<sup>1</sup> The limited solubility of these drugs in aqueous media presents many challenges for pharmaceutical scientists including poor oral bioavailability, significant variation between human subjects, and limited flexibility in controlling appropriate dosing levels.<sup>2</sup> Many approaches are currently used to overcome the difficulties associated with the suboptimal bioavailability of lipophilic pharmaceuticals, some of which include pre-dissolving the compound in a suitable solvent followed by filling the mixture into capsules<sup>3</sup> or by creating a solid solution using water-soluble polymers.<sup>4</sup> While these approaches can aid in partially dissolving poorly-soluble molecules within the aqueous environment of the gastrointestinal (GI) tract, major challenges including bulk drug accumulation upon introduction of the formulation into the GI tract remain.<sup>1</sup>

One of the most promising and readily accessible strategies for overcoming these additional challenges is by using emulsion-based delivery systems, which encapsulate the oil-soluble drug within a natural lipid vehicle. These delivery systems allow the oil-soluble drug to be dispersed uniformly in the GI tract and slowly release the encapsulated compound, thus increasing

the bioavailability of the poorly-soluble therapeutic. Naturally occurring oils (e.g., corn oil, soybean oil, palm oil, etc.) are well suited to act as carries for poorly-soluble therapeutics and are regularly utilized to deliver encapsulated flavor compounds in food engineering applications.<sup>5,6</sup>

Many oil-in-water emulsions used in the delivery of pharmaceuticals are formulated using traditional low molecular weight biological surfactants that significantly reduce the interfacial tension of immiscible fluids and ultimately ease the creation of disperse phase droplets on the order 10s of nanometer to several microns<sup>7,8</sup> Often, a downside of these emulsions is their susceptibility to physical destabilization mechanisms over time, such as droplet coalescence and Ostwald ripening.<sup>9,10</sup> The shelf-life of emulsions of this type has recently been shown to be dramatically extended for similar emulsion-based delivery systems that contain a combination of surfactant and silicon dioxide nanoparticles.<sup>11-14</sup> Silicon dioxide (SiO<sub>2</sub>) has received the “Generally Recognized as Safe” classification as a food for human consumption by the United States Food and Drug Administration.<sup>15</sup> However, many of the surfactants (e.g., cetyltrimethylammonium bromide or CTAB) employed alongside SiO<sub>2</sub> nanoparticles in these studies for improving the dispersion of immiscible fluids exhibit a high degree of toxicity,<sup>16</sup> and as such, their suitability in biological applications is significantly limited.

Understanding the adsorptive and interfacial properties of colloidal silica nanoparticles in the presence of surfactants has proven to be of special interest in recent literature because of the noted association with enhanced dispersion stability.<sup>12,17-20</sup> Surface tension measurements on aqueous particle-surfactant dispersions have been employed as a reliable method for determining the concentration of surfactant monomer in equilibrium with the adsorbed interfacial layer<sup>17,19</sup> and the mechanics of mixed particle-surfactant monolayers have been studied by interfacial rheology.<sup>21,22</sup> In a study by Liggieri et al.,<sup>21</sup> wide frequency dilatational rheology measurements

(ranging from  $10^{-3}$  to  $10^3$  Hz) for SiO<sub>2</sub> nanoparticle-CTAB complexes were performed by using several devices with various operating frequency ranges in conjunction (i.e., an oscillating drop shape tensiometer, a capillary pressure tensiometer and a Langmuir trough). The authors postulated that interfacial monolayers comprised of particle-surfactant complexes exhibit two distinct relaxation mechanisms: one at low frequencies which corresponds to the motion of the surfactant-decorated nanoparticles and one at high frequencies that corresponds to the dynamics of the surfactant. Low-frequency dilatational elasticity has been evidenced as a key contributor in the impedance of film thinning between dispersed drops and bubbles<sup>22-24</sup> (and coalescence by extension<sup>25</sup>), thus understanding such interfacial mechanics is vitally important.

This study specifically seeks to elucidate fundamental phenomena underlying the fabrication of highly stable, oil-in-water emulsions generated by colloidal SiO<sub>2</sub> decorated with the biologically safe emulsifier dipalmitoylphosphatidylcholine (DPPC). Additionally, this work focused solely on the physical correlations between the low-frequency ( $<10^{-1}$  Hz), small-amplitude (2.5% area strain) dilatational viscoelasticity of SiO<sub>2</sub> nanoparticle-surfactant composite interfacial layers and the corresponding stability to coalescence and phase separation of the bulk emulsion. Emulsions stabilized by DPPC alone, SiO<sub>2</sub> nanoparticles alone, and mixtures of the two emulsifiers were fabricated by ultrasonication and their bulk phase behavior and corresponding microstructures were correlated to their interfacial dilatational rheological properties. The connection between interfacial mechanics, observed bulk emulsion behavior, and drop morphology has yet to be adequately discussed within the literature. Thus, this work is exceedingly relevant to formulators seeking a framework for developing stable, nanoparticle-surfactant stabilized emulsions comprised entirely of biologically safe materials.

## 3.2 Experimental Methods

### 3.2.1 Materials and Reagents

The zwitterionic surfactant 1,2-dipalmitoyl-*sn*-glycero-3-phosphocholine (DPPC, >99%, CAS Registry No. 63-89-8) was obtained from Avanti Polar Lipids (Alabaster, AL) and was used as received. DPPC (Figure 3-1) is a semisynthetic phospholipid containing two palmitic acids bonded to a polar phosphocholine head-group. The head-group consists of a positively charged choline moiety covalently bonded to a negatively charged phosphate moiety. The critical micelle concentration of DPPC was reported by the manufacturer as  $0.4 \times 10^{-9}$  M, several orders of magnitude lower than the surfactant concentrations investigated in this study.

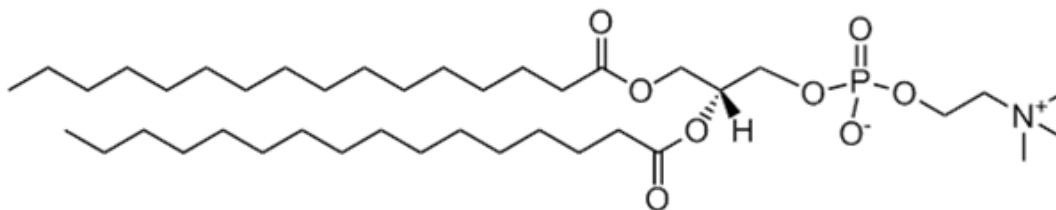


**Figure 3-1** Chemical structure of 1,2-dipalmitoyl-*sn*-glycero-3-phosphocholine, or DPPC.

Unmodified colloidal SiO<sub>2</sub> (Ludox<sup>®</sup> HS-40, CAS Registry No. 7631-86-9) was purchased from Sigma-Aldrich (St. Louis, MO) and supplied as a 40 wt.% aqueous suspension at pH 9.8. The manufacturer reported specific surface area of the SiO<sub>2</sub> suspension was 200 m<sup>2</sup> g<sup>-1</sup>, with a density of 1.3 g cm<sup>-3</sup>. The oil phase in each adsorption experiment and bulk emulsion was a caprylic/capric triglyceride (Neobee<sup>®</sup> 1053, CAS Registry No. 73398-61-5, Stepan Company, Northfield, IL) with a density of 0.949 g cm<sup>-3</sup>. The oil was passed five times through a column containing Al<sub>2</sub>O<sub>3</sub> (CAS Registry No. 1344-28-1, Fisher Scientific, Hampton, NH) prior to use to remove trace surface active impurities. The purity of the resulting oil was verified by measuring its interfacial tension with deionized water, which maintained a constant equilibrated value of

$24.57 \pm 0.45 \text{ mN m}^{-1}$  over 1.5 hours. The water used for each experiment in this study was produced by a Barnsted Nanopure™ system containing a  $0.2 \text{ }\mu\text{m}$  filter and had a measured resistivity of  $18 \text{ M}\Omega \text{ cm}$ .

### 3.2.2 Preparation of Aqueous Dispersions and Bulk Oil-in-Water Emulsions

To obtain the desired concentration of  $\text{SiO}_2$  nanoparticles in the aqueous phase for each experiment, the as-supplied suspension was first diluted to 30 wt.%  $\text{SiO}_2$  and the pH of the was modulated to  $7.06 \pm 0.13$  during dilution with a  $0.1 \text{ M HCl}$  aqueous solution. Further dilution with deionized water was performed to obtain aqueous particle suspensions with the desired concentrations: 0.05, 1, 2.5, 5, 10, and 20 wt.%  $\text{SiO}_2$  with respect to the aqueous phase. In the absence of any added emulsifiers, the  $\text{SiO}_2$  remained well-dispersed in water during dilution. The size and surface zeta ( $\zeta$ ) potential distributions of unmodified silica nanoparticles in aqueous solution at pH 7 were characterized by dynamic light scattering with a Malvern Zetasizer Nano ZS. Dynamic light scattering analysis for the neat  $\text{SiO}_2$  at pH 7 yielded a narrow size distribution with an average particle diameter of  $23.02 \pm 0.25 \text{ nm}$  and average  $\zeta$  potential of  $-42.05 \pm 1.04 \text{ mV}$ . The as-supplied colloidal  $\text{SiO}_2$  possessed a negative surface charge due to the addition of alkali and the subsequent dissociation of silanol groups on the surfaces of the nanoparticles within the aqueous suspension. The estimated contact angle of neat  $\text{SiO}_2$  is  $\theta \sim 20\text{-}37^\circ$ ,<sup>26,27</sup> indicating the bare  $\text{SiO}_2$  nanoparticles in this study were very hydrophilic.

A 2.5 wt.% colloidal  $\text{SiO}_2$  concentration was chosen for interfacial and bulk emulsification studies to make comparisons with previous investigations which have incorporated CTAB as the co-adsorbing surfactant.<sup>12,19</sup> Aqueous dispersions containing 2.5 wt.% colloidal  $\text{SiO}_2$  and the desired DPPC concentration (i.e., 0.01, 0.02, 0.05, 0.1, 0.2, 0.5, and 1 mM) were obtained by diluting a 5 wt.% colloidal  $\text{SiO}_2$  suspension with a concentrated DPPC aqueous suspension and

deionized water. Dilutions were performed by dropwise addition of the aqueous DPPC solution under constant stirring to avoid local particle aggregation upon dilution with the aqueous DPPC suspension. After mixing, the aqueous dispersions containing both emulsifiers were agitated in a sonic bath for 30 seconds, then equilibrated for 24 hours to allow DPPC adsorption onto SiO<sub>2</sub> surfaces. Dynamic light scattering measurements on DPPC-decorated SiO<sub>2</sub> nanoparticles were taken within 48 hours of sample preparation.

The first step in fabricating bulk emulsions consisted of hand-mixing vials containing a 1:1 (v/v) ratio of purified oil and an aqueous dispersion containing one or both emulsifiers for 30 seconds. The coarse emulsion was then sonicated in an ice bath at 4 °C using an ultrasonic probe sonicator (Branson Digital Sonifier, Model 250, 117V, max. output = 200 W) at 30% of the probe's maximum intensity for 1 minute. Each of the resulting oil-water mixtures had a total volume equal to 4 mL. The microstructure and extent of phase separation of each mixture were then imaged and characterized 24 hours after emulsification.

### **3.2.3 Phase Separation Stability and Morphology Characterization**

The stability to gravitational phase separation for each oil-in-water emulsion was determined by quantifying the height of the upper oil-rich layer ( $H_o$ ) and the height of the lower water-rich layer ( $H_w$ ) relative to the total height of the oil-water mixture ( $H_T$ ) after a predetermined equilibration time.<sup>7</sup> The Separation Index (SI) for the upper oil-rich layer ( $SI = 100 \times H_o/H_T$ ) and the lower water-rich layer ( $SI = 100 \times H_w/H_T$ ) was measured for each emulsion 24 hours after fabrication. The opaque middle layer present in select oil-water mixtures comprised the emulsified layer, which was sampled from and used for microstructural characterization. Within this context, smaller SI values corresponded to emulsions with greater stability to gravitational phase separation. All emulsion samples were stored under standard gravity at 25 °C.

Though additional techniques exist for directly measuring the gravity-induced settling rates of emulsions (e.g., X-ray transmission and light scattering techniques), visual observation and utilization of the Separation Index remain the most inexpensive and simply-applied methods for characterizing phase separation stability. Moreover, visual observation is a non-destructive technique that most accurately simulates the behavior of an emulsion under quiescent conditions. Thus, the expected shelf-life of emulsions can be most readily predicted with this method.

The microstructure of the emulsified layer within select oil-water mixtures was studied by depositing an aliquot of the middle emulsified layer from select emulsions onto a glass slide placed on the stage of an inverted bright-field optical microscope (AmScope). Images of the dispersed emulsion droplets were taken with a digital single-lens reflex camera (Nikon D3300) and measurements of the average droplet size and  $\pm 1$  standard deviation were performed via image processing using open-source ImageJ software.<sup>28</sup>

### **3.3 Results and Discussion**

#### **3.3.1 Effect of Bare SiO<sub>2</sub> on Oil-Water Interfacial Properties**

The presence of bare SiO<sub>2</sub> in the aqueous phase (for concentrations between 0.05-20 wt.%) did not measurably reduce the equilibrium interfacial tension from the value obtained for the clean oil-water interface,  $25.47 \pm 0.35$  mN m<sup>-1</sup>. Moreover, measurements of the dilatational viscoelastic moduli for these systems 1.5 hours after interface formation revealed that bare SiO<sub>2</sub> nanoparticles alone did not modify the mechanics of the oil-water interface. The magnitudes of E' and E'' were not experimentally measurable (i.e., E' and E'' were < 1 mN m<sup>-1</sup>) following the 1.5-hour equilibration period irrespective of bulk aqueous concentration. This behavior that was synonymous to the mechanical behavior observed for the clean oil-water interface. Bare SiO<sub>2</sub> nanoparticles in the aqueous phase at pH 7 also displayed a large, negative zeta potential (ca. -40

mV). Each of these results agree well with the previous observations of aqueous dispersions containing bare colloidal SiO<sub>2</sub> particles.<sup>18</sup> It can be inferred from these results that the bare SiO<sub>2</sub> nanoparticles were very hydrophilic and possessed a low driving energy for spontaneous adsorption to the oil-water interface.

### 3.3.2 Effect of DPPC Alone on Oil-Water Interfacial Properties

Equilibrium interfacial tension measurements demonstrated that the rate of surfactant adsorption increased and the measured equilibrium interfacial tension values decreased with greater concentrations of DPPC in the bulk, suggesting a diffusion-controlled surfactant system.<sup>29,30</sup> The corresponding equilibrium interfacial tension values versus DPPC concentration are provided in Figure 3-2, along with the best fit of the Langmuir adsorption isotherm to the experimental data. The Langmuir adsorption isotherm is given by  $\Gamma = \Gamma_{\infty} \frac{c_0}{a_L + c_0}$ , where  $\Gamma_{\infty}$  is the surface excess concentration,  $c_0$  is the bulk DPPC surfactant concentration, and  $a_L$  is the Langmuir adsorption constant ( $= 2.79 \times 10^{-4} \text{ mol m}^{-3}$ )<sup>29</sup> which represents the concentration where half of the maximum interfacial coverage has been achieved (i.e., where  $\Gamma = \Gamma_{\infty}/2$ ). This adsorption model is commonly used for similar surfactant systems<sup>29</sup> and provided a direct approximation of the surface excess concentration,  $\Gamma_{\infty} \approx 2.867 \times 10^{-6} \text{ mol m}^{-2}$ , for DPPC molecules at the oil-water interface. Aqueous solutions containing various concentrations of DPPC alone exhibited interfacial tension reduction and dilatational viscoelastic behavior at the oil-water interface that was anticipated for monolayers of this type.<sup>13,31</sup>

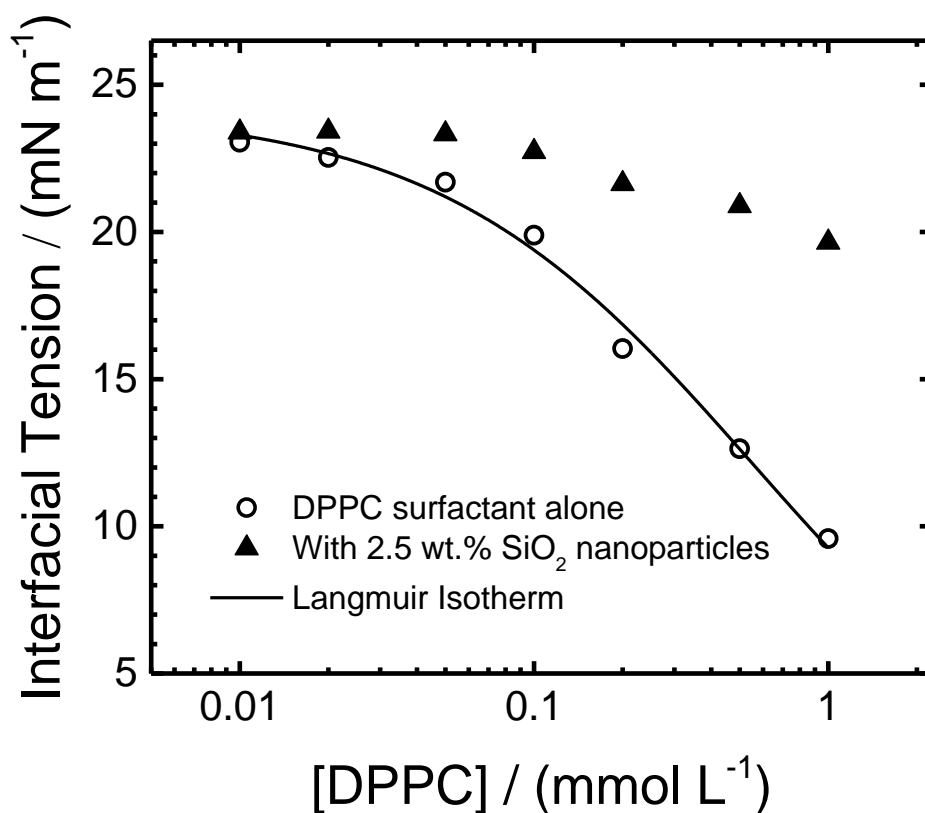


**Figure 3-2** Equilibrium interfacial tensions versus DPPC concentration for oil-water interfaces containing DPPC alone and DPPC in the presence of a fixed SiO<sub>2</sub> concentration (2.5 wt.%). Measurements were obtained 1.5 hours after interface formation. The solid line represents the best fit of the Langmuir adsorption isotherm.

Measurements of the dilatational elastic (storage),  $E'$ , and viscous (loss) modulus,  $E''$ , versus interfacial deformation frequency were performed for oil-water interfaces containing various concentrations of DPPC. The results of this analysis are reported in Figure 3-3 and illustrate a moderate overall increase in  $E'$  with DPPC concentration and no distinguishable trend in  $E''$  for these interfaces. This trend in the dilatational viscoelastic behavior has also been observed in our previous publication<sup>32</sup> for oil-water interfaces laden with DPPC molecules, where higher concentrations of lecithin in the bulk aqueous phase increased adsorption of the surfactant to the

oil-water interface and enabled strengthened hydrogen bonding interactions between molecules within the surfactant monolayer.

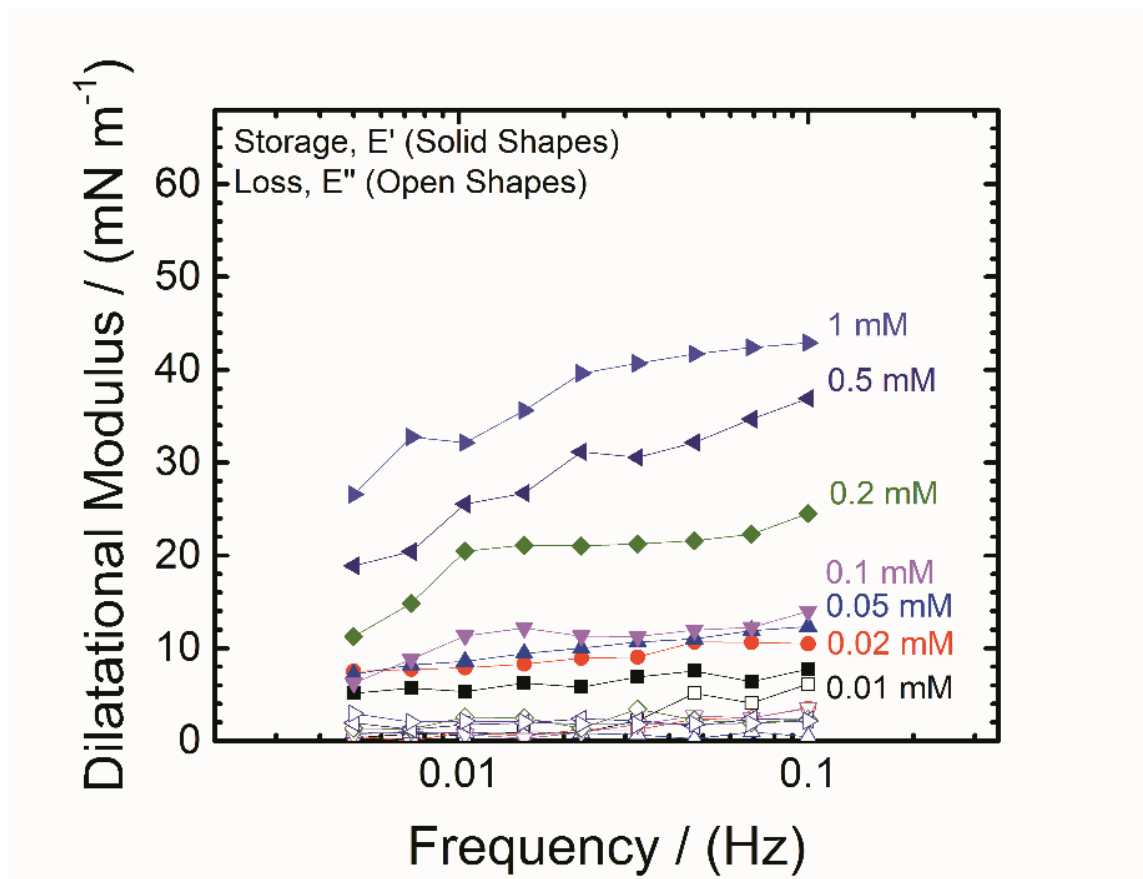


**Figure 3-3** Dilatational storage and loss moduli for oil-water interfaces laden with various concentrations of DPPC alone. Measurements were taken following an interface equilibration period of 1.5 hours. Solid lines are aids for the eye.

### 3.3.3 Physical Association of DPPC and SiO<sub>2</sub> in Water

As mentioned previously, a SiO<sub>2</sub> nanoparticle concentration of 2.5 wt.% was chosen to make comparisons with previous research on the interfacial behavior of CTAB-decorated nanoparticles.<sup>12,19</sup> The number of DPPC molecules adsorbed onto SiO<sub>2</sub> surfaces per particle (in an aqueous environment) is plotted as a function of bulk DPPC concentration in Figure 3-4. These data are given for bulk SiO<sub>2</sub> concentrations ranging from 0.1 – 20 wt.%. Approximation of the DPPC-to-SiO<sub>2</sub> ratio assumed that all available DPPC molecules irreversibly adsorbed onto the available SiO<sub>2</sub> surface area and that no free surfactant remained in the bulk aqueous dispersion following adsorption. Values for the DPPC-to-SiO<sub>2</sub> ratio were calculated from the following mass balance,  $\text{Ratio}_{\text{DPPC to SiO}_2} = \frac{c_0}{a_s \chi_{pw} \rho}$ , where  $c_0$  is the bulk concentration of DPPC,  $a_s$  is the total surface area of the bare SiO<sub>2</sub> (taken as 200 m<sup>2</sup> g<sup>-1</sup> from the manufacturer's specification),  $\chi_{pw}$  is the weight fraction of particle in aqueous dispersion (= 0.025), and  $\rho$  is the density of the dispersion. This process has been routinely applied in the literature for the determination of CTAB adsorption onto the silica nanoparticles in aqueous media.<sup>18,21</sup>

The results of this analysis, coupled with knowledge of  $\Gamma_\infty$  for DPPC, revealed that complete adsorption of DPPC molecules onto SiO<sub>2</sub> surfaces occurs at a bulk DPPC-to- SiO<sub>2</sub> ratio ~5000 to 1. Thus, complete adsorption of DPPC onto SiO<sub>2</sub> surfaces is not expected to occur at any of the chosen DPPC concentrations (0.01–1 mmol L<sup>-1</sup>) for systems containing 2.5 wt.% SiO<sub>2</sub>. However, the results that follow regarding the interfacial rheology of SiO<sub>2</sub>-DPPC interfacial layers indicate that the relatively small concentration of DPPC that does adsorb onto SiO<sub>2</sub> surfaces (~100 DPPC molecules per particle) was enough to promote particle attachment to the oil-water interface and produce to rich dynamic mechanical behavior.

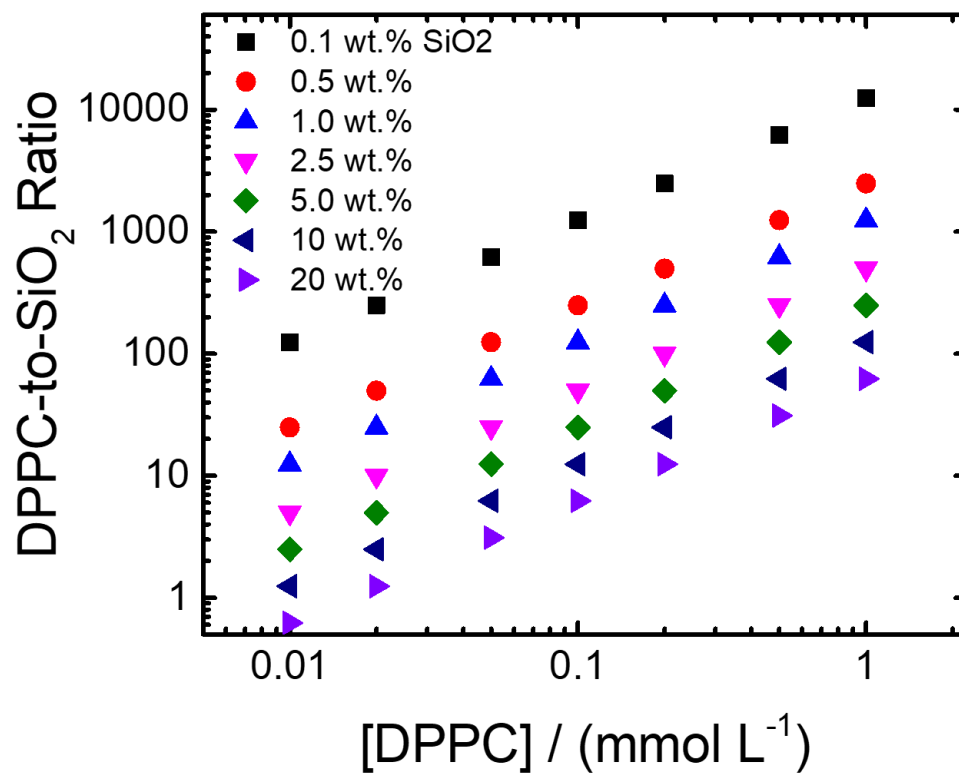


**Figure 3-4** Calculations of DPPC molecule-to-SiO<sub>2</sub> nanoparticle ratio plotted as a function of bulk DPPC concentration. These data assume complete, irreversible adsorption of DPPC molecules onto the available surfaces of SiO<sub>2</sub> in the bulk aqueous phase.

The adsorption of DPPC molecules onto the free surfaces of SiO<sub>2</sub> nanoparticles in the aqueous phase prior to emulsification was investigated by dynamic light scattering. The change in the average  $\zeta$  potentials of SiO<sub>2</sub> (2.5 wt.% loading in water) in the presence of increasing DPPC concentrations was studied at neutral pH (Figure 3-5). Measurement of the  $\zeta$  potential show a stark decrease in the magnitude of the SiO<sub>2</sub> surface charge, from ca. -40 mV for unmodified SiO<sub>2</sub> nanoparticles to ca. -5 mV for SiO<sub>2</sub> in the presence of 2 mM DPPC. This downward trend toward in the magnitude of the  $\zeta$  potential illustrate that DPPC became strongly adsorbed to SiO<sub>2</sub> surfaces with increasing concentrations of DPPC in the aqueous suspension. Neutralization of the surface charge for dispersed SiO<sub>2</sub> nanoparticles is a direct result of electrostatic ion pairing between the negatively-charged silanol groups at the SiO<sub>2</sub> surfaces and the positively charged choline moiety of DPPC molecules. Measurements of the average diameter of particles/agglomerates in the aqueous phase (Table 3-1) revealed an exponential increase in the average particle diameter when the concentration of DPPC exceeded 0.2 mM, which also illustrated surfactant adsorption onto the bare SiO<sub>2</sub> surfaces. This phenomenon has been observed in similar studies of nanoparticle-surfactant complexes.<sup>22,33</sup>

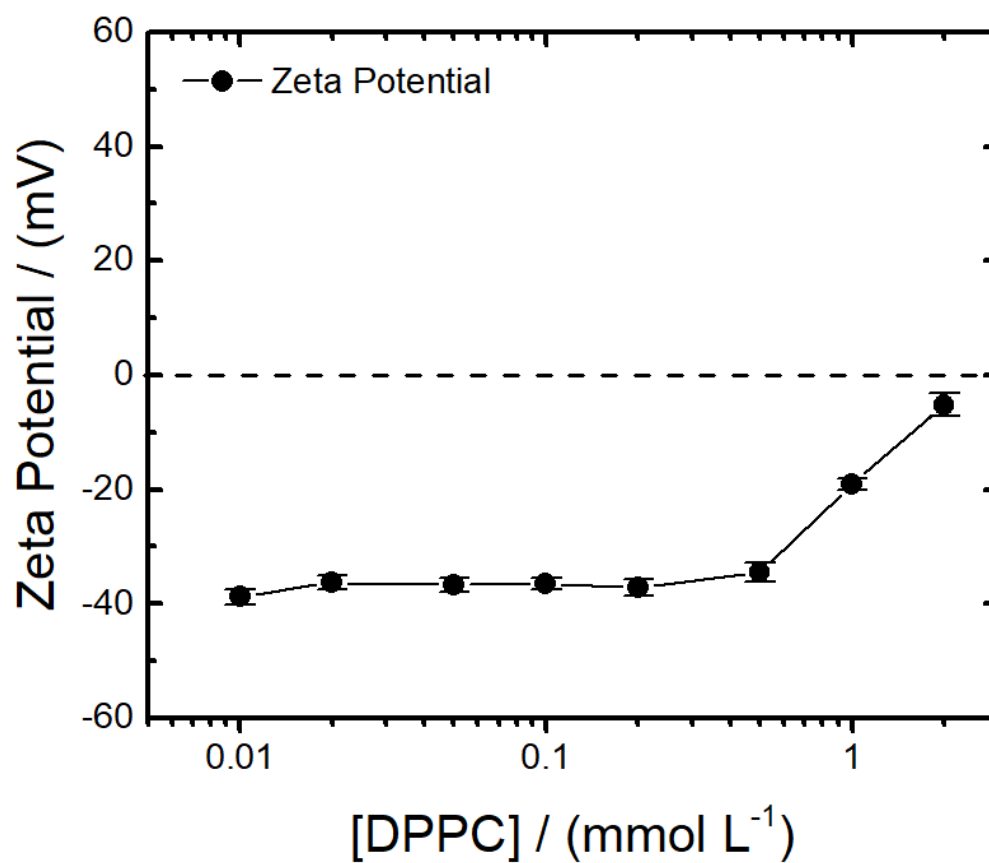


**Figure 3-5** Influence of bulk DPPC concentration on the average zeta potential of SiO<sub>2</sub> nanoparticles in an aqueous suspension at pH 7, as quantified by dynamic light scattering measurements at 25 °C. Each aqueous dispersion contained 2.5 wt.% SiO<sub>2</sub> nanoparticles and measurements were taken within 48 hours of sample preparation. Error bars represent  $\pm 1$  standard deviation.

**Table 3-1** Average hydrodynamic diameters of particles/agglomerates in aqueous mixtures containing 2.5 wt.% SiO<sub>2</sub> and various DPPC concentrations. Measurements were taken within 48 hours of sample preparation.

DPPC Concentration / (mM)	0.01	0.02	0.05	0.10	0.20	0.50	1.00	2.00
Average Diameter / (nm)	25.0	33.0	55.0	56.3	74.0	250.0	476.0	1210.0
Standard Deviation / (nm)	6.23	6.82	5.99	6.54	7.61	9.2	11.47	27.16

### 3.3.4 Interfacial Rheology of Mixed SiO<sub>2</sub>-DPPC Systems

The interfacial relaxation behavior observed for mixed SiO<sub>2</sub>-DPPC systems was quite different from the dynamics observed in systems containing either bare SiO<sub>2</sub> or DPPC alone. Equilibrium interfacial tension values for each system were achieved within 3-5 minutes, and corresponding equilibrium interfacial tension values versus DPPC concentration are reported in Figure 3-2. The equilibrium interfacial tension was observed to decrease slightly with increasing DPPC concentration; however, not to the same extent as systems containing DPPC alone. This difference in interfacial tension reduction provides further evidence that DPPC molecules first adsorb onto the free SiO<sub>2</sub> surfaces in the aqueous phase and partially hydrophobize the surface of the nanoparticles. Following DPPC adsorption onto nanoparticle surfaces, DPPC-decorated SiO<sub>2</sub> nanoparticles are then promoted to the oil-water interface. As discussed in Chapter 3.3.1, bare SiO<sub>2</sub> nanoparticles did not reduce the interfacial tension of the oil-water interface. Thus, partially hydrophobized SiO<sub>2</sub> nanoparticles are presumed to be the key contributor to the observed decrease in the equilibrium interfacial tension.

The response in the dilatational elasticity for oil-water systems containing composite SiO<sub>2</sub>-DPPC mixtures is illustrated in Figure 3-6. The rheological behavior of these systems was different than the behavior observed in systems containing bare SiO<sub>2</sub> nanoparticles (Chapter 3.3.1) or DPPC alone (Figure 3-3). The overall magnitude of the dilatational elasticity trended toward much higher values as the concentration of DPPC increased in the presence of 2.5 wt.% SiO<sub>2</sub>, as compared to systems that contained DPPC alone. Moreover, the frequency dependence of  $E'$  is lower for composite interfaces as compared to interfaces laden with DPPC molecules alone. This behavior may be interpreted as synergistic physical interactions between the SiO<sub>2</sub> and DPPC molecules at the oil-water interface. It has been shown that with sufficient surfactant adsorption, the contact

angle of SiO<sub>2</sub> nanoparticles has increased from low  $\theta$  values to  $\theta \sim 60\text{-}80^\circ$ .<sup>34,35</sup> Thus, the increase in particle hydrophobicity resulting from DPPC adsorption onto SiO<sub>2</sub> surfaces would presumably increase the driving energy for attachment of the nanoparticles at the oil water interface. Moreover, the partially hydrophobized SiO<sub>2</sub> nanoparticles would provide additional rigidity to the interfacial monolayer due to interfacial particle jamming and other particle-surfactant interactions.<sup>36</sup>

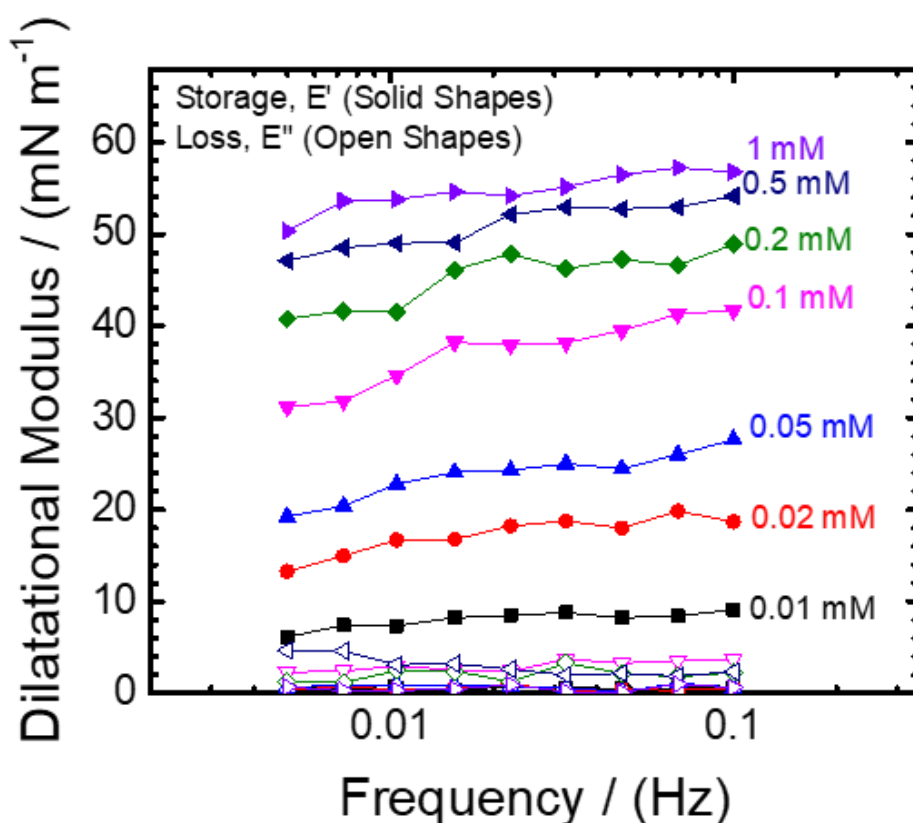


**Figure 3-6** Dilatational storage and loss moduli for oil-water interfaces laden with DPPC-SiO<sub>2</sub> nanoparticle complexes as a function of deformation frequency. Data are shown for increasing concentrations of DPPC in the presence of a fixed SiO<sub>2</sub> nanoparticle concentration (2.5 wt.%). Measurements were taken following an interface equilibration period of 1.5 hours. Solid lines are aids for the eye.

### 3.3.5 Bulk Emulsion Stability and Morphology

The stability of oil-water mixtures with aqueous phases containing either SiO<sub>2</sub> nanoparticles or DPPC alone were investigated first. Bare SiO<sub>2</sub> nanoparticles alone proved to be very poor emulsifying agents for concentrations ranging from 0.05 to 20 wt.%, as shown in Figure 3-7. The initial emulsion type for these systems was oil-in-water. However, each of these oil-water mixtures were highly unstable and susceptible to rapid coalescence and phase separation within the first 2 minutes of emulsification, as indicated by the formation of distinct upper oil-rich layer that comprised approximately half of the bulk mixture and lower water-rich layer containing the aqueous SiO<sub>2</sub> nanoparticle dispersion. The SI values for both the upper oil-rich layer and lower water-rich layer for each of these emulsions was ~50%, indicating completely unstable emulsions. The turbidity of the lower water-rich layer in each of these emulsions was caused by scattering of light by SiO<sub>2</sub> nanoparticle aggregates formed during emulsification. These aggregates sedimented to the bottom of each vial within 48 hours of emulsion formation.

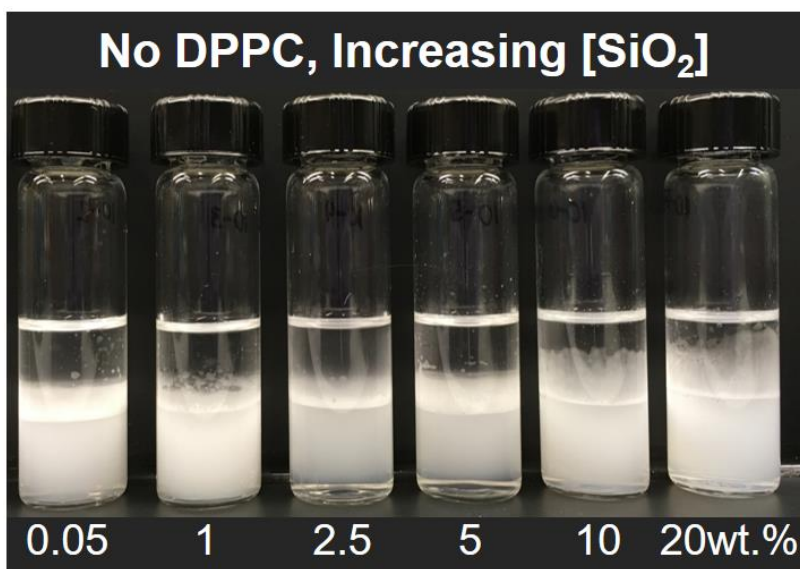


**Figure 3-7** Bulk oil-water mixtures containing initial concentrations of bare SiO<sub>2</sub> nanoparticles ranging from 0.05-20 wt.% in the aqueous phase. This image was taken after emulsification and the 24-hour equilibration period. The transparent upper fluid in each system was the less-dense oil-rich layer and the turbid lower layer fluid is the water-rich SiO<sub>2</sub> nanoparticle suspension. No middle emulsified layer was formed in any of these mixtures.

Systems containing only DPPC in the aqueous phase were slightly better at forming stable emulsions. From Figure 3-8, the formation of an oil-in-water emulsified layer was not attainable for DPPC concentrations below 0.5 mM, which yielded mixtures with distinct oil-rich layers and SI values ~50%. At 0.5 mM DPPC, a semi-stable emulsified layer was observed; however, significant coalescence and phase separation was still evident at this concentration. At 1 mM DPPC, a stable emulsified layer was observed. These results illustrate that at sufficiently high concentrations, DPPC serves as a suitable emulsifier for oil-in-water emulsion-based delivery systems.

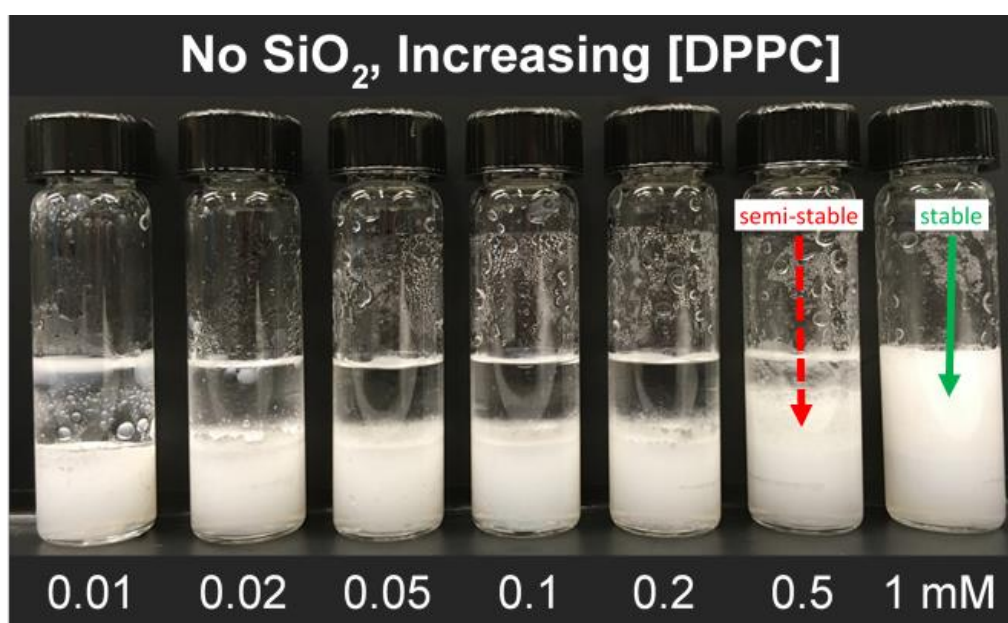


**Figure 3-8** Oil-water mixtures containing initial concentrations of DPPC ranging from 0.01–1 mM in the aqueous phase. The image was taken after emulsification and the 24-hour equilibration period. The translucent upper fluid in each system was the less-dense oil-rich layer and the turbid lower layer was comprised of the water-rich DPPC dispersions. An emulsified layer was formed only in mixtures containing  $\geq 0.5$  mM DPPC. The dashed (red) arrow indicates the location of a semi-stable emulsified layer and solid (green) arrow indicates a stable emulsified layer.

The gravitational phase separation analysis performed after the 24-hour equilibration period for oil-water mixtures containing a fixed concentration of SiO<sub>2</sub> (2.5 wt.%) and varying concentrations of DPPC (0.01-1 mM) are shown in Figure 3-9. Remarkable stability to gravitational phase separation within the 24-hour equilibration period was observed for DPPC concentrations  $\geq 0.2$  mM. A precipitous reduction in the SI values for the upper oil-rich layer in these mixtures was observed between 0.05 and 0.2 mM DPPC, while a linear reduction in the SI values for the lower water-rich layer was seen (Figure 3-9b). However, systems below a concentration of 0.2 mM DPPC, mixtures were unable to form an emulsified layer and phase separated on a timescale shorter than the equilibration period.

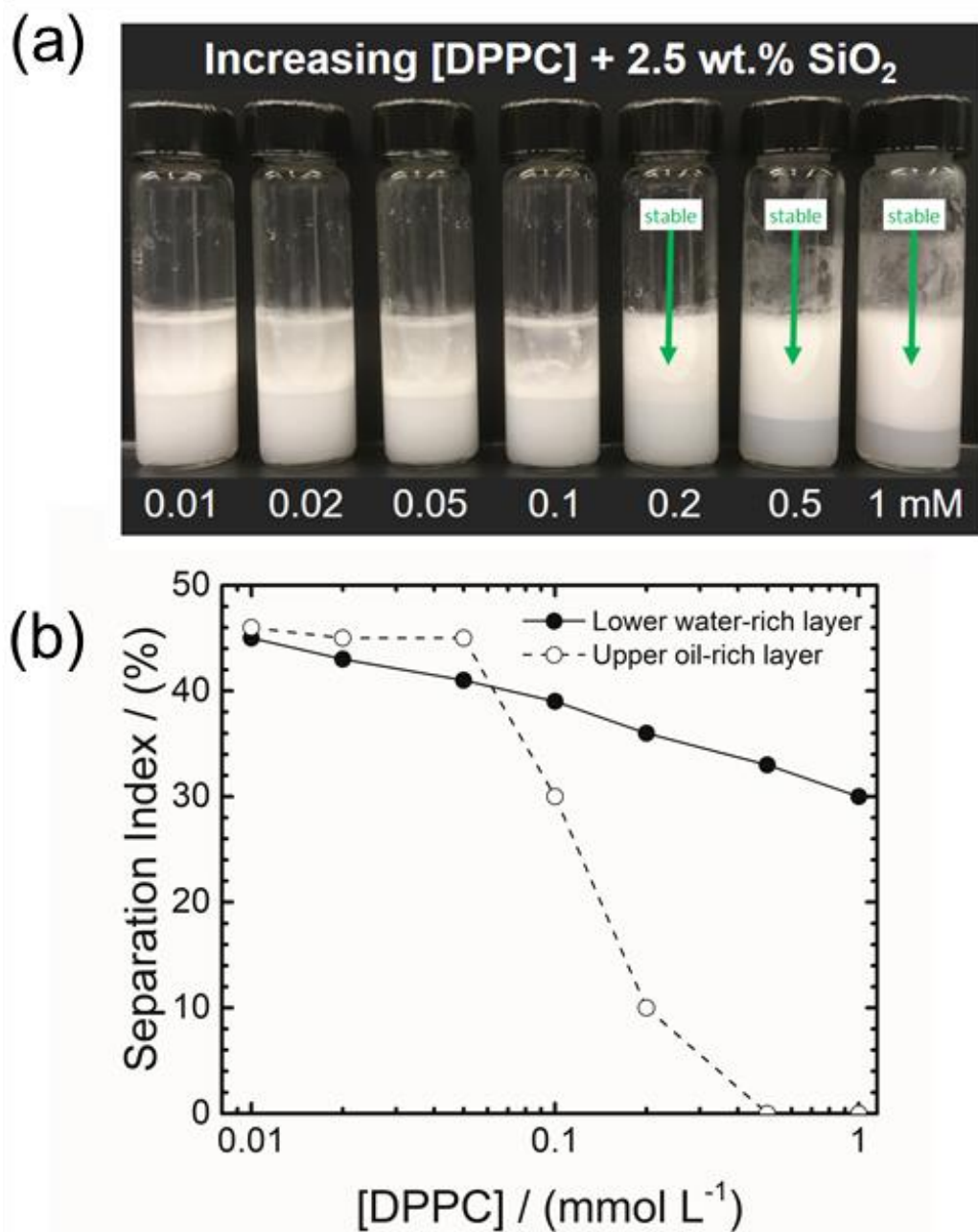


**Figure 3-9** (a) Gravitational phase separation analysis of bulk oil-water mixtures containing a fixed 2.5 wt.% SiO<sub>2</sub> concentration and a varying concentration of DPPC in the aqueous phase. This image was taken after the 24-hour equilibration period following initial emulsification. Dashed (red) arrows indicate the location of semi-stable emulsified layers and solid (green) arrows indicate stable emulsified layers. (b) Separation Index (SI) values for the lower, water-rich layer (closed circles) and the upper, oil-rich layer in each oil-water mixture. Lower SI values correspond to greater stability to phase separation and coalescence.

Micrographs taken 24 hours after emulsification of the emulsified layers in oil-water systems containing a fixed 2.5 wt.% SiO<sub>2</sub> concentration and DPPC concentrations  $\geq 0.2$  mM are shown in Figure 3-10. Each of these emulsions were oil-in-water, as determined by diluting an aliquot of the emulsified layers into a container of pure oil and pure water. Both the average diameter and size distribution of dispersed oil droplets decreased with greater DPPC concentration. The average droplet size and dispersity of the oil droplets in these emulsions trended downward from  $178 \pm 63$   $\mu\text{m}$  to  $65 \pm 32$   $\mu\text{m}$  to  $44 \pm 15$   $\mu\text{m}$  for the mixtures containing 0.2 mM (Figure 3-10a), 0.5 mM (Figure 3-10b), and 1 mM DPPC (Figure 3-10c), respectively.

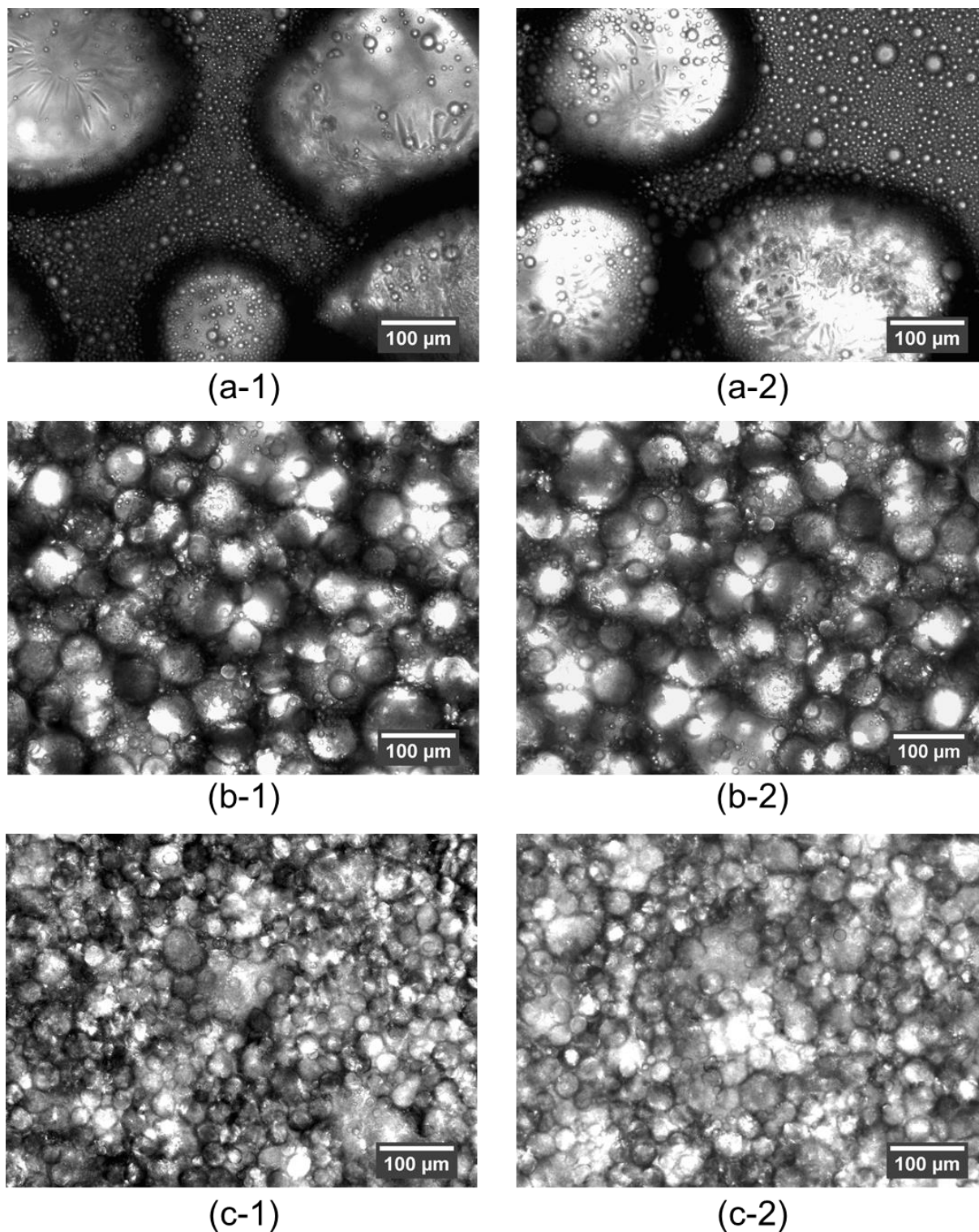


**Figure 3-10** Optical micrographs of the emulsified layers sampled from bulk emulsions obtained after the 24-hour equilibration period. These images correspond to bulk emulsions that contained a fixed 2.5 wt.% SiO<sub>2</sub> concentration and 0.2 mM DPPC (a-1, a-2), 0.5 mM DPPC (b-1, b-2), and 1 mM DPPC (c-1, c-2) in the aqueous dispersion prior to emulsification. Each emulsion was oil-in-water, as determined by dilution measurements. The scale bar in each image is 100 μm.

These behaviors may indicate that denser surfactant adsorption onto the available surfaces of the SiO<sub>2</sub> nanoparticles increases the driving energy for particle attachment to the oil-water interface. This increased driving energy would encourage more nanoparticles to adhere to the oil-water interface during emulsification. Oil-water interfaces densely populated by DPPC-SiO<sub>2</sub> complexes could then halt coalescence earlier, ultimately reducing the observed average diameter and size distribution of the emulsified oil droplets. Similar physical behavior has also been seen for dispersions stabilized by CTAB-SiO<sub>2</sub> nanoparticle complexes,<sup>12,14</sup> where the mechanism underlying this favorable stabilization behavior was attributed to interparticle aggregation within the oil-water interfacial layer.

The effect of increasing SiO<sub>2</sub> concentration at a fixed DPPC concentration (0.1 mM) on emulsion behavior was also determined (Figure 3-11). Noteworthy stability to gravitational phase separation was observed in oil-water mixtures containing  $\geq 5$  wt.% SiO<sub>2</sub>, moderate stability to phase separation was seen for systems containing 1 and 2.5 wt.% SiO<sub>2</sub>, and no phase separation stability was observed for the system containing 0.05 wt.% SiO<sub>2</sub> nanoparticles (Figure 3-11a). The SI values for both the lower water-rich layer and the upper oil-rich layer decreased exponentially as the concentration of SiO<sub>2</sub> nanoparticles increased from 0.05-10 wt.%. These values then appear to approach a plateau at concentrations >10 wt.% (Figure 3-11b).

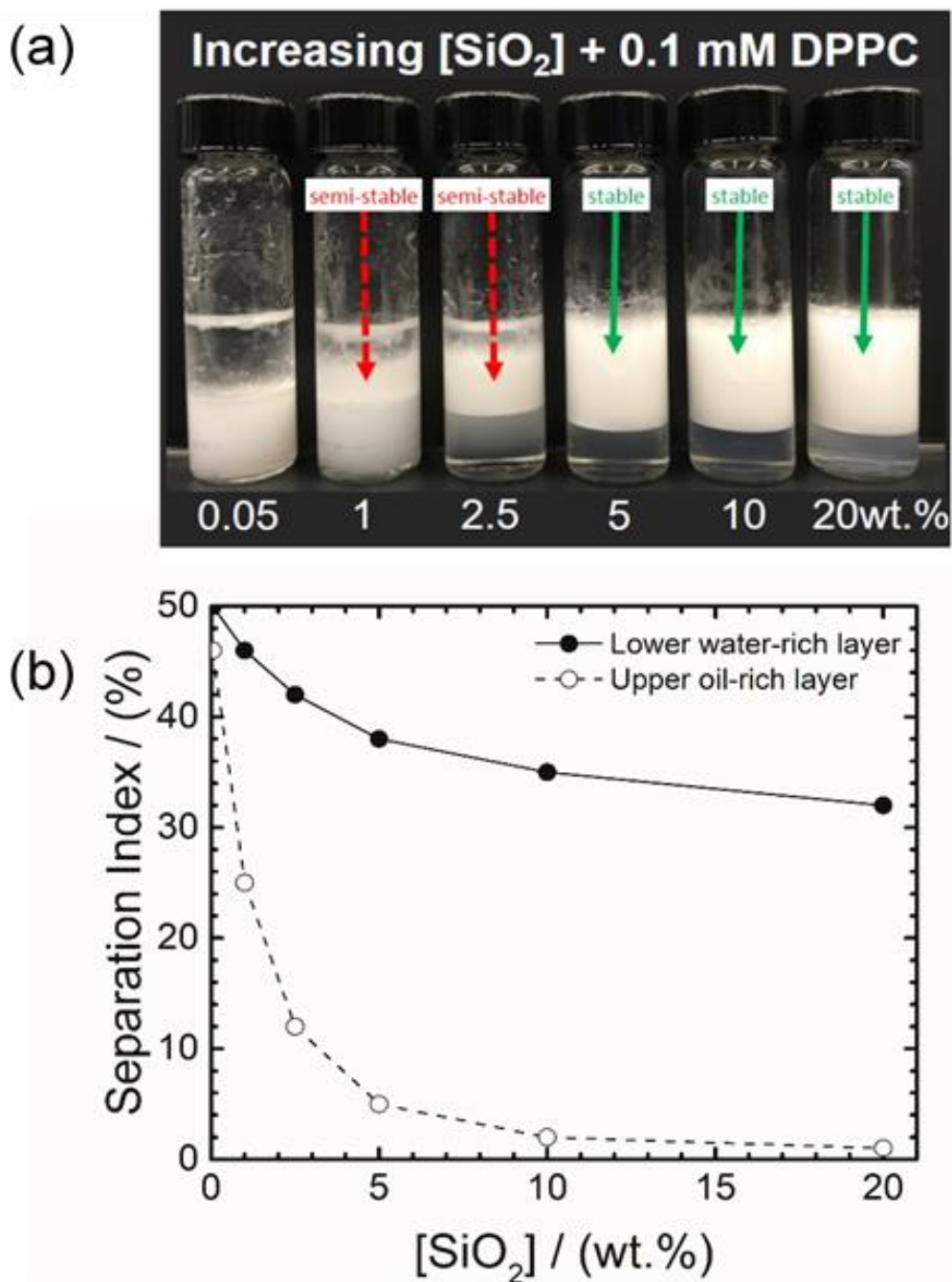


**Figure 3-11** (a) Gravitational phase separation analysis of bulk oil-water mixtures containing a fixed DPPC concentration (0.1 mM) and a varying  $\text{SiO}_2$  concentration (0.5-20 wt.%). This image was taken after the 24-hour equilibration period following initial emulsification. Dashed (red) arrows indicate the location of semi-stable emulsified layers and solid (green) arrows indicate stable emulsified layers. (b) Separation Index (SI) values for the lower, water-rich layer (closed circles) and the upper, oil-rich layer in each oil-water mixture. Lower SI values correspond to greater stability to phase separation and coalescence.

Micrographs taken 24 hours after emulsification of the emulsified layers in oil-water systems containing a fixed 0.1 mM DPPC concentration and the three highest SiO<sub>2</sub> concentrations are provided in Figure 3-12. The average diameter and size distributions of the dispersed oil droplets trended downward from  $149 \pm 51 \mu\text{m}$ ,  $58 \pm 17 \mu\text{m}$ , to  $52 \pm 13 \mu\text{m}$  for emulsions containing 2.5 wt.% (Figure 3-12a), 10 wt.% (Figure 3-12b), and 20 wt.% (Figure 3-12c) SiO<sub>2</sub>, respectively. The average size and distribution of the dispersed drops appeared to decrease with increasing SiO<sub>2</sub> concentration until an equilibrium droplet size could be obtained, yielding oil droplets with highly consistent sizes, regardless of bulk SiO<sub>2</sub> loading. This may be interpreted as the point where oil-water interfaces become completely saturated with DPPC-decorated SiO<sub>2</sub> nanoparticles and interparticle jamming halts the droplets at their equilibrium size. Beyond this point, no additional particles could adsorb to the interface, and further addition of SiO<sub>2</sub> had no synergistic effect.

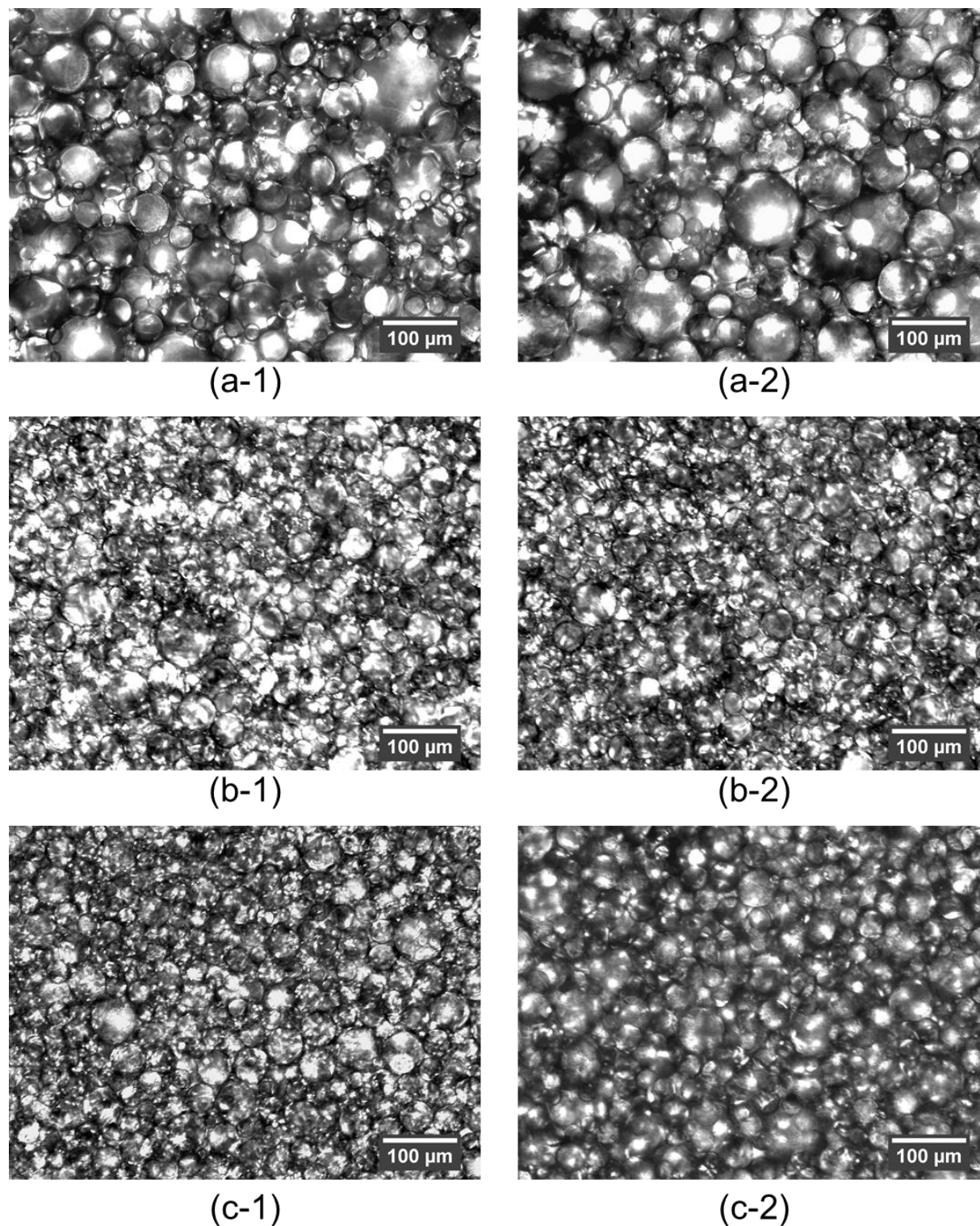


**Figure 3-12** Optical micrographs of the emulsified layers sampled from bulk emulsions obtained after the 24-hour equilibration period. These images correspond to bulk emulsions that contained a fixed 0.1 mM DPPC concentration and 2.5 wt.% SiO<sub>2</sub> (a-1, a-2), 10 wt.% SiO<sub>2</sub> (b-1, b-2), or 20 wt.% SiO<sub>2</sub> (c-1, c-2) in the aqueous dispersion prior to emulsification. Each emulsion was oil-in-water, as determined by dilution measurements. The scale bar in each image is 100 μm.

Interestingly, emulsions containing a fixed SiO<sub>2</sub> concentration and  $\geq 0.5$  mM DPPC (Figure 3-9a) did not show any visible signs of coalescence for  $> 3$  months, whereas emulsions containing a fixed DPPC concentration and  $\geq 5$ wt.% SiO<sub>2</sub> (Figure 3-11a) began to display substantial signs of coalescence in  $< 3$  days. The difference in stabilization observed for the two cases could be attributed to differences in the mechanism by which the dispersed droplets were stabilized. In the former case, the surface area available for molecules to adsorb remained fixed, while the concentration of molecules available to adsorb onto the free nanoparticle surfaces increased. This increased the density of surfactant adsorption onto the surfaces of the nanoparticles, and ultimately the density of nanoparticles that could populate the oil-water interface. In the latter case, the concentration of molecules available to adsorb onto the free nanoparticle surfaces remained constant, while the surface area available for surfactant adsorption (and bulk concentration of SiO<sub>2</sub>) increased. While the low concentration of DPPC could promote some interfacial particle attachment, the high concentration of nanoparticles in the aqueous phase would also stabilize the emulsions by reducing the rate of liquid drainage in the interstices between dispersed droplets. Coalescence between oil drops would still proceed rather easily in this case because the interfaces were insufficiently covered with nanoparticle-surfactant complexes. Thus, droplet breakup would readily occur, producing the observed bulk phase separation within 3 days.

### 3.4 Summary

The results of this work illustrate the following: (1) DPPC addition modifies the hydrophobicity of initially hydrophilic SiO<sub>2</sub> nanoparticles by amphiphilic adsorption. (2) The concentration of DPPC necessary to modify the hydrophilicity of SiO<sub>2</sub> nanoparticles (and ergo, their interfacial affinity) is an order of magnitude lower than what has been previously observed for uncompressed CTAB-SiO<sub>2</sub> nanoparticle complexes.<sup>21</sup> (3) The magnitude of the dilatational

elastic modulus for uncompressed DPPC-SiO<sub>2</sub> nanoparticle complexes is an order of magnitude higher than previous observations.<sup>14,21,22</sup> (4) The observed stability to gravitational phase separation is markedly higher for oil-in-water emulsions stabilized by DPPC-SiO<sub>2</sub> as compared to oil-in-water emulsion stabilized by either emulsifier alone.

Low molecular weight surfactants are known to improve an emulsion's resistance to various phenomena that contribute to bulk phase separation at sufficiently high concentrations.<sup>10</sup> However, reducing the bulk concentration of surfactant necessary to generate emulsion-based delivery with excellent coalescence and creaming stability is desirable, as doing so is anticipated to dramatically reduce the cost of fabricating emulsion-based delivery systems for biopharmaceutical applications. The amount of surfactant necessary to achieve an emulsion-based delivery system with desirable stability characteristics can be reduced by the incorporation of SiO<sub>2</sub> nanoparticles.

While mixed monolayers of DPPC and solid particles have been investigated,<sup>37-40</sup> direct relation to bulk emulsion stabilization phenomena have been omitted from these studies. The results of the present study therefore provide additional insight into the correlation between the interfacial rheological behavior of DPPC-SiO<sub>2</sub> composite interfacial layers and bulk emulsion susceptibility to gravitational phase separation. These results are highly relevant for academic and industrial emulsion formulators that seek highly-stable oil-in-water emulsions comprised entirely of biologically safe materials.

### 3.5 References

- (1) Wadhwa, J.; Nair, A.; Kumria, R. Emulsion Forming Drug Delivery System for Lipophilic Drugs. *Drug Res. (Stuttg)*. **2012**, *69* (2), 179–191.
- (2) Stegemann, S.; Leveiller, F.; Franchi, D.; de Jong, H.; Lindén, H. When Poor Solubility Becomes an Issue: From Early Stage to Proof of Concept. *Eur. J. Pharm. Sci.* **2007**, *31* (5), 249–261. <https://doi.org/10.1016/j.ejps.2007.05.110>.
- (3) Cole, E. T.; Cade, D.; Benameur, H. Challenges and Opportunities in the Encapsulation of Liquid and Semi-Solid Formulations into Capsules for Oral Administration. *Adv. Drug Deliv. Rev.* **2008**, *60* (6), 747–756. <https://doi.org/10.1016/j.addr.2007.09.009>.
- (4) Porter, C. J. H.; Pouton, C. W.; Cuine, J. F.; Charman, W. N. Enhancing Intestinal Drug Solubilisation Using Lipid-Based Delivery Systems. *Adv. Drug Deliv. Rev.* **2008**, *60* (6), 673–691. <https://doi.org/10.1016/j.addr.2007.10.014>.
- (5) Bakry, A. M.; Abbas, S.; Ali, B.; Majeed, H.; Abouelwafa, M. Y.; Mousa, A.; Liang, L. Microencapsulation of Oils: A Comprehensive Review of Benefits, Techniques, and Applications. *Compr. Rev. Food Sci. Food Saf.* **2016**, *15* (1), 143–182. <https://doi.org/10.1111/1541-4337.12179>.
- (6) Papagianni, M.; Anastasiadou, S. Encapsulation of *Pediococcus Acidilactici* Cells in Corn and Olive Oil Microcapsules Emulsified by Peptides and Stabilized with Xanthan in Oil-in-Water Emulsions: Studies on Cell Viability under Gastro-Intestinal Simulating Conditions. *Enzyme Microb. Technol.* **2009**, *45* (6–7), 514–522. <https://doi.org/10.1016/j.enzmictec.2009.06.007>.
- (7) McClements, D. J. Critical Review of Techniques and Methodologies for Characterization of Emulsion Stability. *Crit. Rev. Food Sci. Nutr.* **2007**, *47* (7), 611–649. <https://doi.org/10.1080/10408390701289292>.
- (8) Hörmann, K.; Zimmer, A. Drug Delivery and Drug Targeting with Parenteral Lipid Nanoemulsions - A Review. *J. Control. Release* **2016**, *223*, 85–98. <https://doi.org/10.1016/j.jconrel.2015.12.016>.
- (9) McClements, D. J. *Food Emulsions Principles, Practices, and Techniques*; CRC Press, 2005. <https://doi.org/10.1093/acprof:oso/9780195383607.003.0002>.
- (10) Tadros, T. F. *Applied Surfactants: Principles and Applications*; Wiley, 2005.
- (11) Eskandar, N. G.; Simovic, S.; Prestidge, C. A. Synergistic Effect of Silica Nanoparticles and Charged Surfactants in the Formation and Stability of Submicron Oil-in-Water Emulsions. *Phys. Chem. Chem. Phys.* **2007**, *9* (48), 6426–6434. <https://doi.org/10.1039/b710256a>.

- (12) Binks, B. P.; Rodrigues, J. A.; Frith, W. J. Synergistic Interaction in Emulsions Stabilized by a Mixture of Silica Nanoparticles and Cationic Surfactant. *Langmuir* **2007**, *23* (7), 3626–3636. <https://doi.org/10.1021/la0634600>.
- (13) Santini, E.; Guzmán, E.; Ferrari, M.; Liggieri, L. Emulsions Stabilized by the Interaction of Silica Nanoparticles and Palmitic Acid at the Water-Hexane Interface. *Colloids Surfaces A Physicochem. Eng. Asp.* **2014**, *460*, 333–341. <https://doi.org/10.1016/j.colsurfa.2014.02.054>.
- (14) Ravera, F.; Ferrari, M.; Liggieri, L.; Loglio, G.; Santini, E.; Zanobini, A. Liquid-Liquid Interfacial Properties of Mixed Nanoparticle-Surfactant Systems. *Colloids Surfaces A Physicochem. Eng. Asp.* **2008**, *323* (1–3), 99–108. <https://doi.org/10.1016/j.colsurfa.2007.10.017>.
- (15) *CFR - Code of Federal Regulations Title 21*; U.S. Food and Drug Administration, 2018.
- (16) Isomaa, B.; Reuter, J.; Djupsund, B. M. The Subacute and Chronic Toxicity of Cetyltrimethylammonium Bromide (CTAB), a Cationic Surfactant, in the Rat. *Arch. Toxicol.* **1976**, *35* (2), 91–96. <https://doi.org/10.1007/BF00372762>.
- (17) Cummins, P. G.; Staples, E.; Penfold, J. Study of Surfactant Adsorption on Colloidal Particles. *J. Phys. Chem.* **1990**, *94* (9), 3740–3745. <https://doi.org/10.1021/j100372a071>.
- (18) Ravera, F.; Santini, E.; Loglio, G.; Ferrari, M.; Liggieri, L. Effect of Nanoparticles on the Interfacial Properties of Liquid/Liquid and Liquid/Air Surface Layers. *J. Phys. Chem. B* **2006**, *110* (39), 19543–19551. <https://doi.org/10.1021/jp0636468>.
- (19) Binks, B. P.; Rodrigues, J. A. Enhanced Stabilization of Emulsions Due to Surfactant-Induced Nanoparticle Flocculation. *Langmuir* **2007**, *23* (14), 7436–7439. <https://doi.org/10.1021/la700597k>.
- (20) Pichot, R.; Spyropoulos, F.; Norton, I. T. O/W Emulsions Stabilised by Both Low Molecular Weight Surfactants and Colloidal Particles: The Effect of Surfactant Type and Concentration. *J. Colloid Interface Sci.* **2010**, *352* (1), 128–135. <https://doi.org/10.1016/j.jcis.2010.08.021>.
- (21) Liggieri, L.; Santini, E.; Guzmán, E.; Maestro, A.; Ravera, F. Wide-Frequency Dilational Rheology Investigation of Mixed Silica Nanoparticle–CTAB Interfacial Layers. *Soft Matter* **2011**, *7* (17), 7699. <https://doi.org/10.1039/c1sm05257h>.
- (22) Kirby, S. M.; Anna, S. L.; Walker, L. M. Effect of Surfactant Tail Length and Ionic Strength on the Interfacial Properties of Nanoparticle-Surfactant Complexes. *Soft Matter* **2017**, *14*, 112–123. <https://doi.org/10.1039/c7sm01806a>.
- (23) Maestro, A.; Santini, E.; Zabiegaj, D.; Llamas, S.; Ravera, F.; Liggieri, L.; Ortega, F.; Rubio, R. G.; Guzman, E. Particle and Particle-Surfactant Mixtures at Fluid Interfaces: Assembly, Morphology, and Rheological Description. *Adv. Condens. Matter Phys.* **2015**, *2015*. <https://doi.org/10.1155/2015/917516>.

- (24) Manga, M. S.; Hunter, T. N.; Cayre, O. J.; York, D. W.; Reichert, M. D.; Anna, S. L.; Walker, L. M.; Williams, R. A.; Biggs, S. R. Measurements of Submicron Particle Adsorption and Particle Film Elasticity at Oil-Water Interfaces. *Langmuir* **2016**, *32* (17), 4125–4133. <https://doi.org/10.1021/acs.langmuir.5b04586>.
- (25) Hudson, S. D.; Jamieson, A. M.; Burkhart, B. E. The Effect of Surfactant on the Efficiency of Shear-Induced Drop Coalescence. *J. Colloid Interface Sci.* **2003**, *265* (2), 409–421. [https://doi.org/10.1016/S0021-9797\(03\)00396-5](https://doi.org/10.1016/S0021-9797(03)00396-5).
- (26) Safouane, M.; Langevin, D.; Binks, B. P. Effect of Particle Hydrophobicity on the Properties of Silica Particle Layers at the Air-Water Interface. *Langmuir* **2007**, *23* (23), 11546–11553. <https://doi.org/10.1021/la700800a>.
- (27) Hunter, T. N.; Jameson, G. J.; Wanless, E. J. Determination of Contact Angles of Nanosized Silica Particles by Multi-Angle Single-Wavelength Ellipsometry. *Aust. J. Chem.* **2007**, *60* (9), 651–655. <https://doi.org/10.1071/CH07133>.
- (28) Eliceiri, K.; Schneider, C. A.; Rasband, W. S.; Eliceiri, K. W. NIH Image to ImageJ: 25 Years of Image Analysis. *Nat. Methods* **2012**, *9* (7), 671–675. <https://doi.org/10.1038/nmeth.2089>.
- (29) Li, J.; Miller, R.; Möhwald, H. Characterisation of Phospholipid Layers at Liquid Interfaces. 1. Dynamics of Adsorption of Phospholipids at the Chloroform/Water Interface. *Colloids Surfaces A Physicochem. Eng. Asp.* **1996**, *114*, 113–121. [https://doi.org/10.1016/0927-7757\(96\)03521-2](https://doi.org/10.1016/0927-7757(96)03521-2).
- (30) Pinazo, A.; Wen, X.; Liao, Y. C.; Prosser, A. J.; Franses, E. I. Comparison of DLPC and DPPC in Controlling the Dynamic Adsorption and Surface Tension of Their Aqueous Dispersions. *Langmuir* **2002**, *18* (23), 8888–8896. <https://doi.org/10.1021/la020476r>.
- (31) Seredyuk, V.; Alami, E.; Nydén, M.; Holmberg, K.; Peresyphkin, A. V.; Menger, F. M. Adsorption of Zwitterionic Gemini Surfactants at the Air-Water and Solid-Water Interfaces. *Colloids Surfaces A Physicochem. Eng. Asp.* **2002**, *203* (1–3), 245–258. [https://doi.org/10.1016/S0927-7757\(01\)01106-2](https://doi.org/10.1016/S0927-7757(01)01106-2).
- (32) Nash, J. J.; Erk, K. A. Stability and Interfacial Viscoelasticity of Oil-Water Nanoemulsions Stabilized by Soy Lecithin and Tween 20 for the Encapsulation of Bioactive Carvacrol. *Colloids Surfaces A Physicochem. Eng. Asp.* **2017**, *517*, 1–11. <https://doi.org/10.1016/j.colsurfa.2016.12.056>.
- (33) Wang, W.; Gu, B.; Liang, L.; Hamilton, W. A. Adsorption and Structural Arrangement of Cetyltrimethylammonium Cations at the Silica Nanoparticle-Water Interface. *J. Phys. Chem. B* **2004**, *108* (45), 17477–17483. <https://doi.org/10.1021/jp048325f>.
- (34) Maestro, A.; Guzmán, E.; Santini, E.; Ravera, F.; Liggieri, L.; Ortega, F.; Rubio, R. G. Wettability of Silica Nanoparticle-Surfactant Nanocomposite Interfacial Layers. *Soft Matter* **2012**, *8* (3), 837–843. <https://doi.org/10.1039/c1sm06421e>.

- (35) Maestro, A.; Guzmán, E.; Ortega, F.; Rubio, R. G. Contact Angle of Micro- and Nanoparticles at Fluid Interfaces. *Curr. Opin. Colloid Interface Sci.* **2014**, *19* (4), 355–367. <https://doi.org/10.1016/j.cocis.2014.04.008>.
- (36) Hunter, T. N.; Pugh, R. J.; Franks, G. V.; Jameson, G. J. The Role of Particles in Stabilising Foams and Emulsions. *Adv. Colloid Interface Sci.* **2008**, *137* (2), 57–81. <https://doi.org/10.1016/j.cis.2007.07.007>.
- (37) Guzmán, E.; Santini, E.; Ferrari, M.; Liggieri, L.; Ravera, F. Effect of the Incorporation of Nanosized Titanium Dioxide on the Interfacial Properties of 1,2-Dipalmitoyl-Sn-Glycerol-3-Phosphocholine Langmuir Monolayers. *Langmuir* **2017**, *33* (40), 10715–10725. <https://doi.org/10.1021/acs.langmuir.7b02484>.
- (38) Guzmán, E.; Ferrari, M.; Santini, E.; Liggieri, L.; Ravera, F. Effect of Silica Nanoparticles on the Interfacial Properties of a Canonical Lipid Mixture. *Colloids Surfaces B Biointerfaces* **2015**, *136*, 971–980. <https://doi.org/10.1016/j.colsurfb.2015.11.001>.
- (39) Guzmán, E.; Santini, E.; Zabiegaj, D.; Ferrari, M.; Liggieri, L.; Ravera, F. Interaction of Carbon Black Particles and Dipalmitoylphosphatidylcholine at the Water/Air Interface: Thermodynamics and Rheology. *J. Phys. Chem. C* **2015**, *119* (48), 26937–26947. <https://doi.org/10.1021/acs.jpcc.5b07187>.
- (40) Guzmán, E.; Orsi, D.; Cristofolini, L.; Liggieri, L.; Ravera, F. Two-Dimensional DPPC Based Emulsion-like Structures Stabilized by Silica Nanoparticles. *Langmuir* **2014**, *30* (39), 11504–11512. <https://doi.org/10.1021/la502183t>.

## CHAPTER 4 GRAVITATIONAL PHASE SEPARATION OF OIL-IN-WATER EMULSIONS BY SiO<sub>2</sub> NANOPARTICLE-INDUCED FLOCCULATION

Portions of the following chapter contain text and figures adapted from the article “Gravitational phase separation of oil-in-water emulsions by SiO<sub>2</sub> nanoparticle-induced flocculation,” with permission from **J.J. Nash** and K.A. Erk.

### 4.1 Introduction

Requirements on the purity of the wastewater discharged by marine vessels into internationally regulated waters have become increasingly stringent in recent years.<sup>1</sup> This is because a disproportionately large amount of the oily wastewater (of the order of millions of tons annually<sup>2</sup>) is released into aquatic environments by shipping and offshore oil and gas operations via bilge water, ballast water, and produced water.<sup>3</sup> Oily bilge water is a multiphase emulsified mixture produced during shipboard machinery operation and maintenance and primarily comprised of water, oil (e.g., mineral, vegetable, or synthetic), and stabilizing surfactants (i.e., detergents).<sup>4,5</sup> Separating the oil from bilge water presents many unique challenges, primarily because a significant portion of this oil is contained within well-dispersed oil droplets smaller than 20 μm.<sup>6</sup> Generally, the total oil content of oily waste water is ~1-10% and thus the formation of oil-in-water emulsions is favored.<sup>2</sup> Many oil separation techniques have been employed to treat oily bilge water emulsion onboard marine vessels including centrifugation,<sup>7,8</sup> reverse osmosis and ultrafiltration,<sup>9,10</sup> and various photocatalytic methods.<sup>11,12</sup> However, several drawbacks to each of these techniques remain including processing time, instrumentation costs, and scalability of the separation technique.

Oily bilge water emulsions are known to contain both ionic and nonionic surfactants, where the stabilizing ionic surfactant typically contains an anionic sulfate moiety.<sup>12</sup> Ionic surfactants generally provide greater stability to droplet flocculation and gravitational phase separation (as compared to nonionic surfactants) due to their innate ability to electrostatically stabilize emulsion droplets, whereas nonionic surfactants provide enhanced mechanical stability to coalescence as a result of steric hinderance.<sup>13,14</sup> It has been shown in the literature that anionic surfactants are the dominant stabilizing component of oily bilge water emulsions<sup>12</sup> and that this category of surfactants is highly effective at inhibiting droplet flocculation and phase separation.<sup>14</sup> Additionally, the enhanced resistance to gravitational phase separation of the hardest to remove oil in bilge water has been shown to be due to the neutral buoyancy of the dispersed oil,<sup>15</sup> the exceedingly small length scale of the droplets,<sup>6</sup> and the electrostatic charge stabilization provided by the anionic surfactant.<sup>15</sup> As such, a model oil-in-water emulsion comprised of a neutrally buoyant natural oil and a widely utilized industrial anionic surfactant was the primary focus of this study.

The co-adsorption of surfactant molecules and silicon dioxide (SiO<sub>2</sub>) nanoparticles at the oil-water interface has been studied extensively for their combined ability to improve the coalescence resistance of oil-in-water Pickering emulsions.<sup>16-19</sup> However, only one study has shown how colloidal SiO<sub>2</sub> nanoparticles can be used to destabilize conventional surfactant-stabilized oil-in-water emulsions,<sup>20</sup> while none have investigated how oppositely-charged SiO<sub>2</sub> nanoparticles can be used phase separate electrostatically-stabilized oil-in-water emulsions. It was hypothesized that mixing oppositely-charged (positive) SiO<sub>2</sub> nanoparticles with an electrostatically-stabilized, conventional oil-in-water emulsion would induce rapid droplet flocculation and phase separation. This hypothesis was based on the knowledge that (1) complex

coacervates can be created from the association of oppositely charged molecules in an aqueous solution and that (2) larger colloidal aggregates are more susceptible to gravitational effects than their primary constituents.

It was predicted that the attractive electrostatic interactions between the negatively-charged oil droplet surfaces and the positively charged SiO<sub>2</sub> surfaces in water could be exploited to control the size of flocs that formed within model bilge water emulsions. The rate of sedimentation or creaming for a spherical, rigid particle in a Newtonian fluid is given by Stokes' Law,  $v = -\frac{2gr^2(\rho_2 - \rho_1)}{9\eta_1}$ , where  $r$  is the particle's radius,  $g$  is the acceleration due to gravity,  $\rho_1$  and  $\rho_2$  are the densities of the continuous phase and dispersed phase, respectively, and  $\eta_1$  is the viscosity of the continuous phase. Stokes' Law can also be used to calculate the sedimentation or creaming rate of flocs within an emulsion, assuming that the flocs are spherical and that the system is reasonably dilute.<sup>21</sup> Here, the rate of displacement,  $v_{\text{floc}}$ , depends on both the size and structure of the flocs. The characteristics of the primary droplets ( $r, \rho_2$ ) are substituted by those of the flocs ( $r_{\text{floc}}, \rho_{\text{floc}}$ ), yielding  $v_{\text{floc}} = -\frac{2gr_{\text{floc}}^2(\rho_{\text{floc}} - \rho_1)}{9\eta_1}$ . This equation states that the magnitude of the gravitational separation rate for a floc increases proportionally with the square of its radius. Thus, as expected, the rate of gravitational phase separation increases for larger flocs.

In this work, a straightforward and cost-effective preprocessing methodology is outlined for the treatment of oily shipboard waste water. A model of hazardous oil-in-water bilge water emulsions was made using a naturally-derived triglyceride oil, which approximates the neutral buoyancy and hydrophobicity of the oily components in bilge water. This model emulsion was stabilized by the anionic surfactant sodium lauryl ether sulfate (SLES) because of its ubiquity in the cleaning solutions aboard marine vessels.<sup>12</sup> Positively-charged SiO<sub>2</sub> nanoparticles were incorporated into the emulsion to neutralize the electrostatic repulsive forces of the dispersed oil

droplets and to induce widespread flocculation. Destabilization behavior of nanoparticle-emulsion mixtures was monitored as a function of time and a simple mass balance for determining the concentration of nanoparticles necessary to induce this desired destabilization behavior was also established.

The connection between interfacial mechanics and the observed stabilization behavior of oily bilge water emulsions has yet to be adequately analyzed in the literature. Thus, this work is exceedingly relevant to waste water managers aboard marine vessels, as the knowledge gathered in this study can be directly applied to optimize various processes involved in the separation of oil from shipboard bilge water emulsions.

## **4.2 Experimental Methods**

### **4.2.1 Materials**

The anionic surfactant sodium alkyl (C10-16) ether sulfate (SLES, molar mass = 328.38 g mol<sup>-1</sup>, CAS Registry No. 68585-34-2) was obtained from Stepan Company (Northfield, IL) and was used as received. The oil phase used to model the stabilized organic compounds found in bilge water emulsions was a caprylic/capric triglyceride (Neobee<sup>®</sup> 1053, CAS Registry No. 73398-61-5, Stepan Company, Northfield, IL) with a viscosity of 15.9 mPa s and density of 0.949 g cm<sup>-3</sup>. The oil was passed five times through a column containing Al<sub>2</sub>O<sub>3</sub> (CAS Registry No. 1344-28-1, Fisher Scientific, Hampton, NH) prior to use to remove trace surface active impurities. The purity of the resulting oil was verified by measuring its interfacial tension with deionized water, which maintained a constant equilibrated value of 24.57 ± 0.45 mN m<sup>-1</sup> over 1.5 hours. The water used for each experiment in this study was produced by a Barnsted Nanopure<sup>™</sup> system containing a 0.2 μm filter and had a measured resistivity of 18 MΩ cm.

The nanoparticles used were those of colloidal SiO<sub>2</sub> (Ludox<sup>®</sup> CL, CAS Registry No. 7631-86-9), which were purchased from Sigma-Aldrich (St. Louis, MO) and supplied as a 30 wt.% aqueous suspension at pH 3.8. The manufacturer reported a specific surface area of 230 m<sup>2</sup> g<sup>-1</sup> and a suspension density of 1.23 g cm<sup>-3</sup> at 25 °C. The nanoparticles in this colloidal suspension have each been coated with a layer of Al<sub>2</sub>O<sub>3</sub>. This surface coating shifts the isoelectric point of the nanoparticles to ~8.5,<sup>22</sup> leading them to possess a positive surface charge at low and neutral pH values. The size and surface zeta (ζ) potential distributions were measured for a 1 wt.% aqueous suspension of these colloidal SiO<sub>2</sub> particles at pH 7.1 by dynamic light scattering measurements using a Zetasizer Nano ZS instrument (Malvern, Worcestershire, United Kingdom). The ζ potential for the SiO<sub>2</sub> nanoparticles was +26.5 ± 2.1 mV, and the average particle diameter from the particle size distribution (Figure 4-1) was 31.2 ± 1.6 nm. Additionally, the estimated contact angle of neat SiO<sub>2</sub> is θ ~ 20-37°,<sup>23,24</sup> indicating the bare SiO<sub>2</sub> nanoparticles in this study were very hydrophilic.

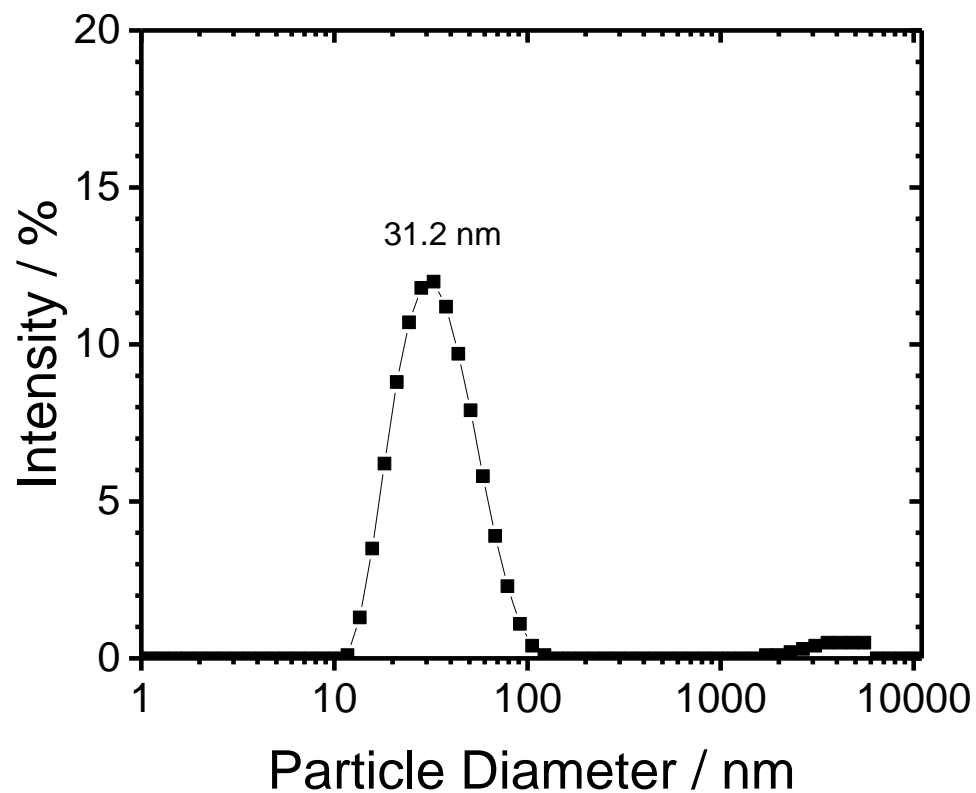


**Figure 4-1** Particle size distribution for a 1 wt.% Ludox CL nanoparticle aqueous suspension at pH 7.1, as determined by dynamic light scattering measurements using a Malvern Zetasizer Nano ZS instrument. The corresponding  $\zeta$  potential for the nanoparticles in this suspension was measured to be  $+ 26.5 \pm 2.1$  mV.

#### 4.2.2 Preparation of Model Oil-in-Water Bilge Emulsions

The first step in fabricating model bilge water emulsions consisted of hand-mixing vials containing  $25 \text{ g L}^{-1}$  (25,000 ppm) triglyceride oil and  $2.5 \text{ g L}^{-1}$  (2500 ppm) SLES in a container of deionized water for 30 seconds. These concentrations were  $\sim 25$  times higher than those used in previous investigations on model bilge water systems<sup>12,25</sup> and were chosen to aid in illustrating the effectiveness of the investigated procedure through visual methods. The coarse emulsion was then sonicated in an ice bath at  $4 \text{ }^{\circ}\text{C}$  using an ultrasonic probe sonicator (Branson Digital Sonifier, Model 250, 117V, max. output = 200 W) at 20% of the probe's maximum intensity for 1 minute. Each of the resulting oil-in-water emulsions had a total mass equal to 100 g. The model emulsion was equilibrated for 24 hours following emulsification. Aliquots of the model bilge emulsion were then partitioned into 8 mL scintillation vials, each containing 3 mL of the emulsion (Figure 4-2).

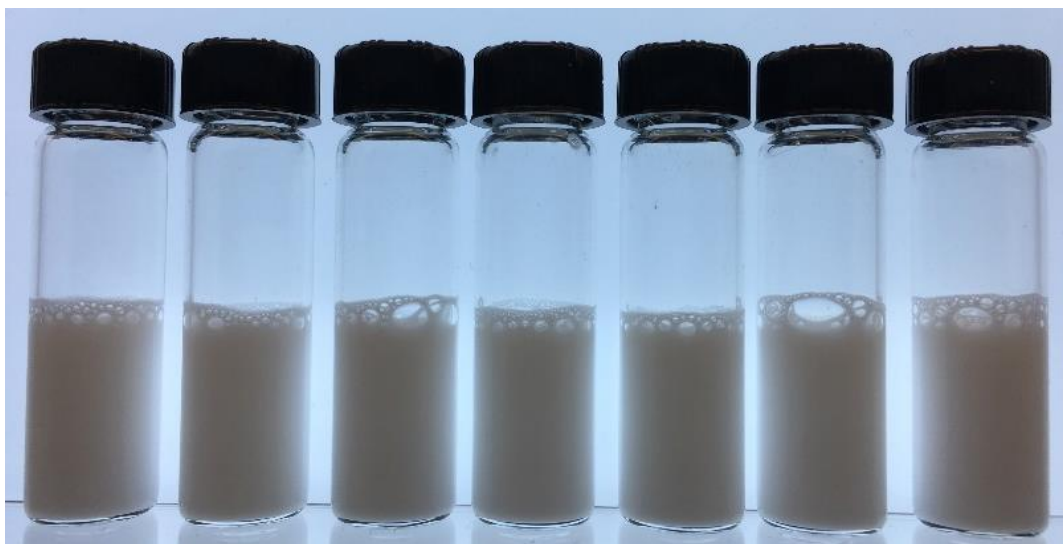


**Figure 4-2** Photograph of the neat model emulsion partitioned into scintillation vials, 24 hours after initial emulsification. The emulsion in each of these vials comprises 25,000 ppm of dispersed oil and 2500 ppm SLES surfactant in deionized water.

The size and surface zeta ( $\zeta$ ) potential distributions of the model bilge water emulsion was characterized by dynamic light scattering with a Zetasizer Nano ZS (Malvern, Worcestershire, United Kingdom). Emulsification produced spherical oil-in-water emulsion droplets with bimodal size distribution. The average droplet diameters were located at 290.9 nm and 2.85  $\mu\text{m}$ . Dispersed oil droplets also had an average  $\zeta$  potential of  $-81.5 \pm 6.2$  mV, corresponding to highly negative, electrostatically stabilized droplets. The size distribution and morphology of the model bilge water emulsions are illustrated in Figure 4-3a and 4-3b, respectively.

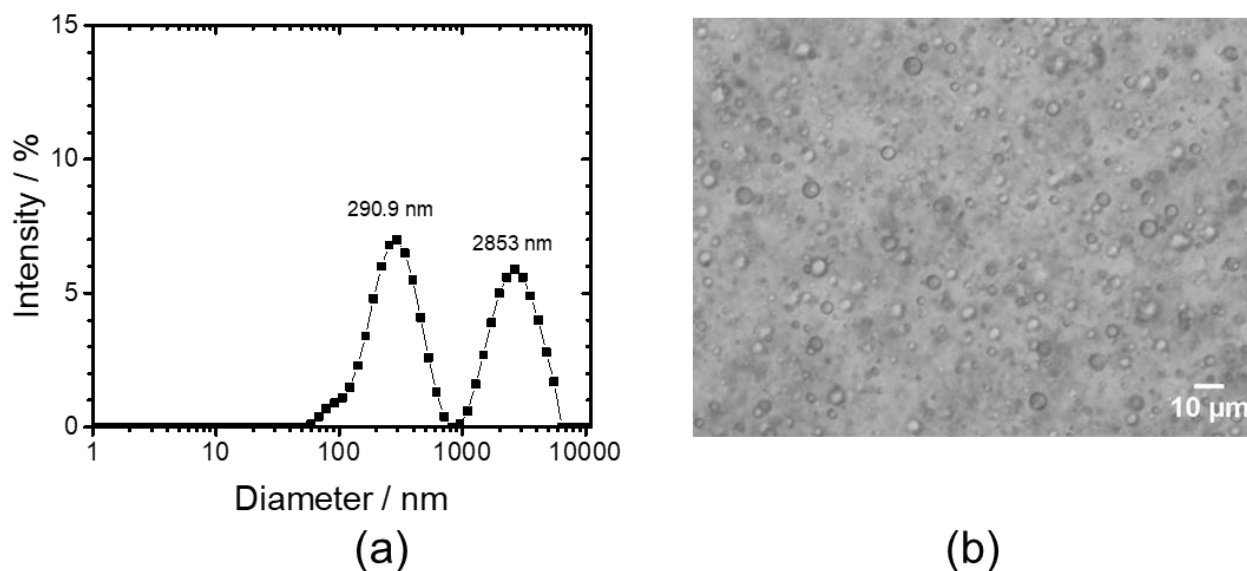


**Figure 4-3** (a) Particle size distribution, as determined by dynamic light scattering measurements using a Malvern Zetasizer Nano ZS instrument, and (b) corresponding micrograph of the neat, oil-in-water model emulsion. The emulsion used in each analysis comprised  $\sim 12,500$  ppm of dispersed oil.

### 4.2.3 Preparation of Aqueous SiO<sub>2</sub> Nanoparticle Suspensions

An approximation for the weight fraction of positively charged SiO<sub>2</sub> nanoparticles necessary to induce flocculation between all of the dispersed oil droplets in the model bilge water emulsion was determined by the following mass balance,  $\chi_{\text{SiO}_2} = \frac{c_{\text{SLES}}}{a_{\text{SiO}_2} \rho_{\text{SiO}_2} \Gamma_{\infty}}$ , where  $c_{\text{SLES}}$  is the bulk concentration of the surfactant in the emulsion,  $a_{\text{SiO}_2}$  is the specific surface area of the positively charged SiO<sub>2</sub> nanoparticles,  $\rho_{\text{SiO}_2}$  is the density of the SiO<sub>2</sub> nanoparticle suspension, and  $\Gamma_{\infty}$  is the saturation adsorption, or maximum surface density, of the surfactant. Here,  $c_{\text{SLES}}$  was taken as 2.5 g L<sup>-1</sup>,  $\Gamma_{\infty}$  was taken as 4.0 x 10<sup>-6</sup> mol m<sup>-2</sup> from Xu et al.,<sup>26</sup> and  $a_{\text{SiO}_2}$  and  $\rho_{\text{SiO}_2}$  were 230 m<sup>2</sup> g<sup>-1</sup> and 1.23 g mL<sup>-1</sup>, respectively, from the manufacturer's specifications. These quantities predicted that  $\chi_{\text{SiO}_2} = 0.67$  g per 100 g of the model emulsion (i.e., 0.67 wt.% SiO<sub>2</sub>). This mass balance was inspired by previous research studies on particle-surfactant complexes.<sup>27,28</sup>

To utilize this mass balance, it was assumed that all surfactant molecules in the emulsion were capable of adsorbing onto the available surface area of the SiO<sub>2</sub> nanoparticles at their maximum surface density ( $\Gamma_{\infty}$ ). Thus, this weight fraction estimates the maximum amount of SiO<sub>2</sub> required for complete transference of the surfactant molecules from their initial locations within the emulsion (i.e., at droplet interfaces and in micelles) to the surfaces of the SiO<sub>2</sub> nanoparticles. However, it was anticipated that this value would be an upper limit for the concentration of SiO<sub>2</sub> required to induce flocculation, as complete transference of all surfactant molecules in the emulsion would not be necessary to elicit widespread aggregation of the dispersed oil droplets. To obtain aqueous dispersions with the desired concentrations of SiO<sub>2</sub> nanoparticles, the as-supplied Ludox<sup>®</sup> CL suspension was diluted with deionized water. Aqueous dispersions containing 0.2, 0.4, 1, 1.5, 2, 4, 10, and 22 wt.% SiO<sub>2</sub> were prepared, which were then mixed in equal parts with the equilibrated model emulsion at a 1:1 (w/w) ratio.

#### 4.2.4 Emulsion Stability Characterization

The stability of the model emulsions following dilution with positively charge SiO<sub>2</sub> nanoparticles was investigated first by visual observation. Scintillation vials containing 3 mL of the model emulsion were diluted with 3 mL of a positively charged SiO<sub>2</sub> nanoparticle aqueous suspension with a concentration ranging from 0.2-22 wt.% SiO<sub>2</sub>. Unless otherwise specified, the SiO<sub>2</sub> nanoparticle suspension was added to the vials containing the model emulsion and was immediately vortex mixed for 30 seconds at 2500 rpm using an LP Vortex Mixer (Thermo Fisher Scientific, Waltham, MA). Images of the emulsion-particle mixtures were taken at two distinct intervals (i.e., 30 minutes and 24 hours after dilution) to qualitatively illustrate emulsion destabilization rates and physical behavior.

The non-flocculated, water-rich regions of the particle-emulsion mixtures were sampled from for dynamic light scattering analysis to investigate the concentration and size distribution of oil droplets that remained dispersed following the dilution procedure. The microstructure of the flocculated layer within select particle-emulsion mixtures was studied by depositing an aliquot of the flocculated layer from select emulsions onto a glass slide placed on the stage of an inverted bright-field optical microscope (AmScope). Images of the dispersed emulsion droplets were taken with a digital single-lens reflex camera (Nikon D3300) and post processing was performed using open-source ImageJ software.<sup>29</sup> Each of these destabilization analyses were performed following the dilution process and 24-hour equilibration period.

### 4.3 Results and Discussion

#### 4.3.1 Emulsion Destabilization – Effect of Vortex Mixing and Order of Addition

The accuracy of the mass balance proposed in Chapter 4.2.3 and the relative importance of vortex mixing following dilution were investigated first. Model oil-in-water emulsions which were diluted with 0-2 wt.% SiO<sub>2</sub> nanoparticle aqueous suspensions are shown in Figure 4-4. Particle-emulsion mixtures which were vortex mixed (Figure 4b and 4d) and were not vortex mixed (Figure 4-4a and 4-4c) for 30 seconds at 2500 rpm following dilution are shown after a 30-minute (Figure 4-4a and 4-4b) and a 24-hour (Figure 4-4c and 4-4d) equilibration period.

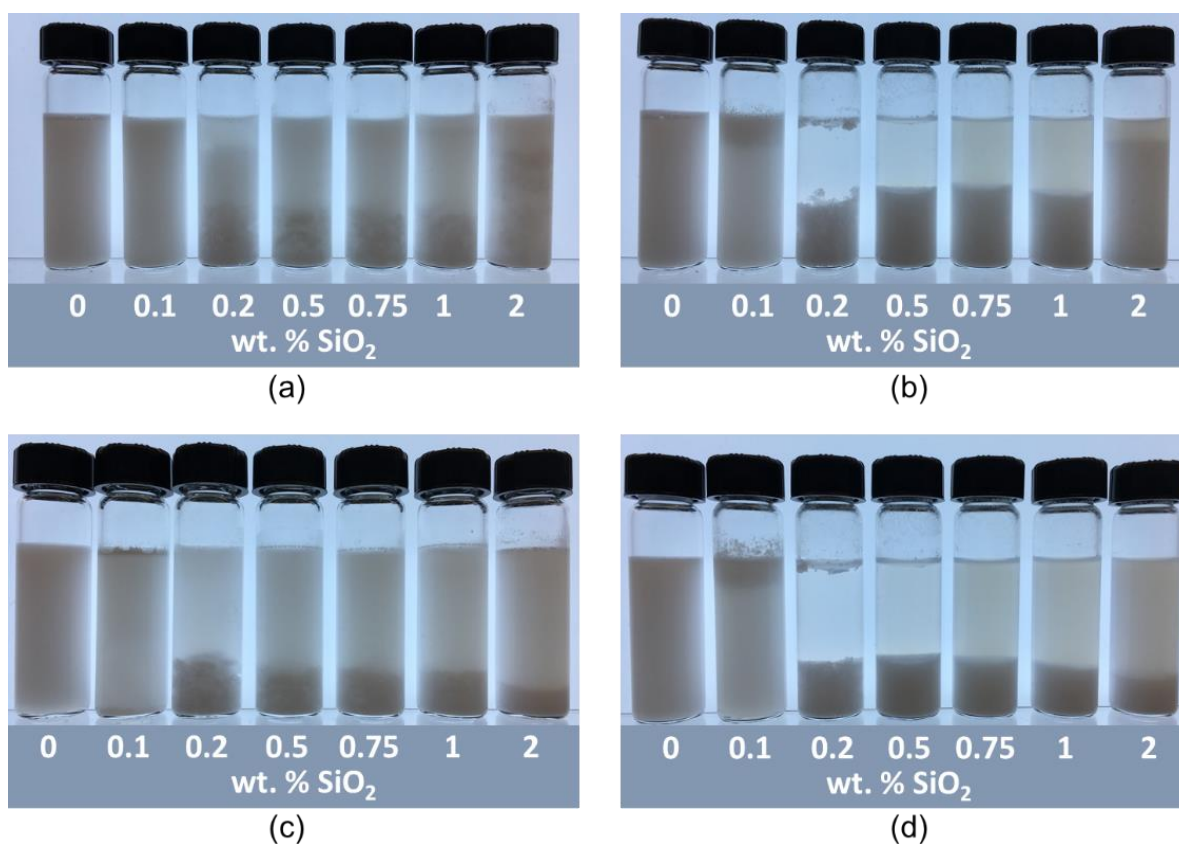


**Figure 4-4** Photographs of bulk oil-in-water emulsions following dilution with positively charged SiO<sub>2</sub> nanoparticles for a final nanoparticle concentration of 0, 0.1, 0.2, 0.5, 0.75, 1, or 2 wt.% SiO<sub>2</sub>. The images illustrate systems which were not vortex mixed (a and c) and those that were vortex mixed (b and d) for 30 seconds at 2500 rpm immediately following dilution. Destabilization behavior is shown for the mixtures after a 30-minute (a and b) and 24-hour (c and d) equilibration interval. The opaque regions in each mixture illustrate flocculated, oil-rich regions and the translucent/slightly turbid regions correspond to the droplet-depleted, water-rich regions of the mixture.

Overall, vortex mixing after diluting the model emulsion with the positively charged SiO<sub>2</sub> nanoparticle suspension was observed to have a noteworthy positive effect on the degree of oil droplet gravitational phase separation. Droplet-depleted, water-rich regions in mixtures that were not subjected to vortex mixing (Figure 4-4a and 4-4c) were more turbid than systems that were vortex mixed (Figure 4-4b and 4-4d), after both the 30-minute and 24-hour equilibration period. For each emulsion set, oil droplet flocculation was most pronounced immediately after dilution when the mixture contained 0.2 wt.% SiO<sub>2</sub>. At this concentration, the nanoparticle-emulsion mixture displayed very rapid droplet flocculation (<30 minutes) when dilution was coupled with vortex mixing. In the absence of subsequent mixing, the timescale of complete droplet flocculation increased by at least two orders of magnitude (>>24 hours).

Floc sedimentation stood in contrast to the creaming behavior (i.e., floc migration to the top of the vial) that is anticipated for similar oil-in-water emulsion systems.<sup>21</sup> Generally, creaming behavior would be expected for aggregates in such systems because the density of the dispersed oil droplets (0.949 g cm<sup>-3</sup>) was lower than that of the surrounding water phase (0.998 g cm<sup>-3</sup>). Therefore, the sedimentation behavior observed for the flocculated oil droplets in these mixtures was presumably due to the interfacial adsorption of positively charged SiO<sub>2</sub> nanoparticles. The SiO<sub>2</sub> in this study had a greater effective density (1.9 g cm<sup>-3</sup>) than water,<sup>30</sup> and thus, as the positively-charged SiO<sub>2</sub> associated with the negatively-charged SLES molecules at droplet interfaces, the SiO<sub>2</sub> became incorporated within the floc and increased its effective density. With the excess incorporation of SiO<sub>2</sub>, the density of the floc exceeded the density of aqueous continuous phase and produced a downward driving energy that favored floc sedimentation.

A comparison of particle-emulsion mixtures which were either diluted with an aqueous SiO<sub>2</sub> nanoparticle suspension or vice versa are shown in Figure 4-5. Each of these systems were

vortex mixed and are shown after a 30-minute (Figure 4-5a and 4-5b) and 24-hour (Figure 4-5c and 4-5d) equilibration period. When the SiO<sub>2</sub> suspensions were added to the model emulsion and the mixtures were vortexed, droplet flocculation occurred rapidly (<30 minutes) for SiO<sub>2</sub> nanoparticle concentrations between 0.2-1 wt.%. All aggregates that formed in these mixtures sedimented to the bottom of their respective scintillation vials. The mixture that contained 0.2 wt.% SiO<sub>2</sub> exhibited the fastest floc formation and sedimentation under standard gravity (~10 minutes).

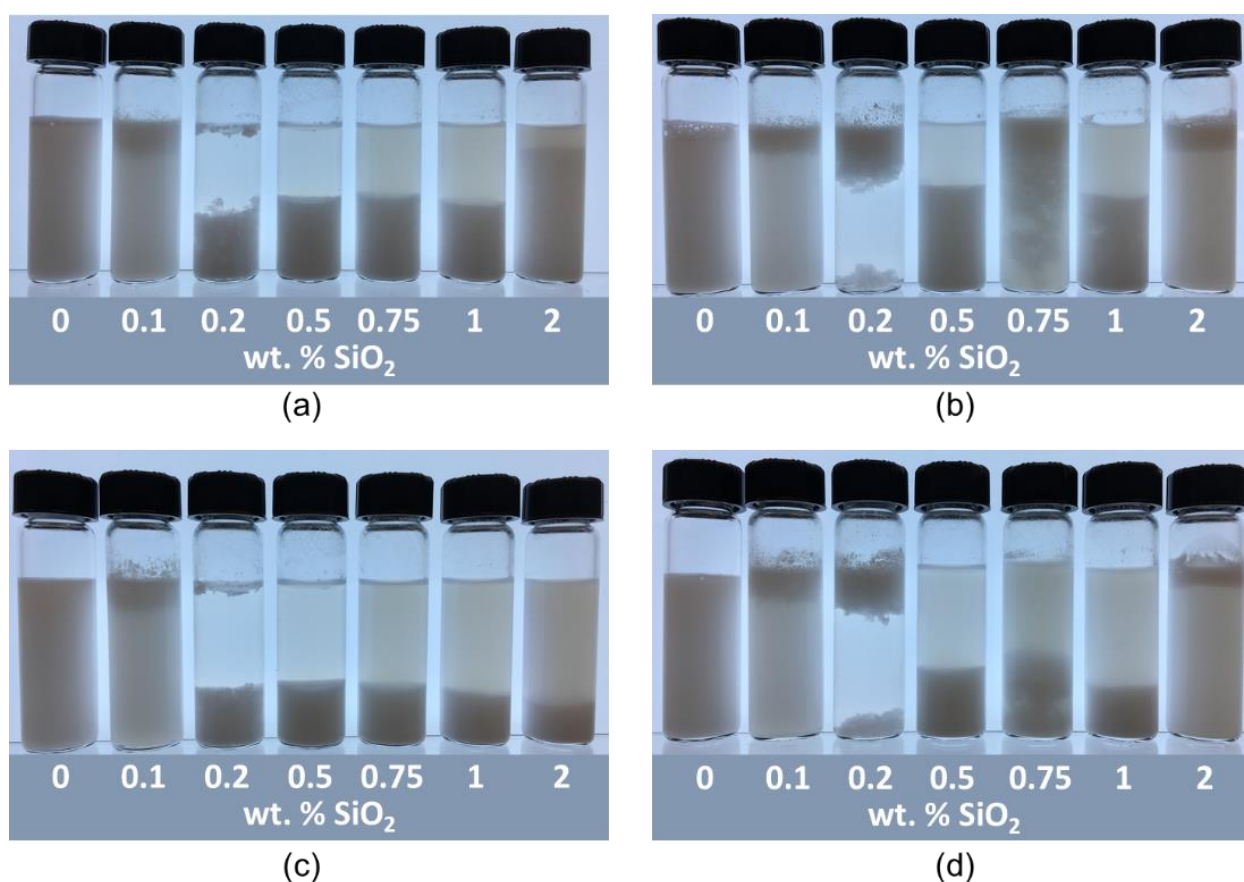


**Figure 4-5** Photographs of bulk oil-in-water emulsions following dilution, where positively charged SiO<sub>2</sub> nanoparticles were added to the neat model emulsion (a and c) or vice-versa (b and d). Each of these mixtures was vortex mixed for 30 seconds at 2500 rpm immediately following dilution. The final SiO<sub>2</sub> concentrations in each set of experiments was 0, 0.1, 0.2, 0.5, 0.75, 1, or 2 wt.% SiO<sub>2</sub>. Destabilization behavior is shown for the mixtures after a 30-minute (a and b) and 24-hour (c and d) equilibration interval. The opaque regions in each mixture illustrate flocculated, oil-rich regions and the translucent/slightly turbid regions correspond to the droplet-depleted, water-rich regions of the mixture.

Similarly, when the model emulsion was added to the SiO<sub>2</sub> suspensions (Figure 4-5b and 4-5d), rapid droplet aggregation (<30 minutes) was also observed. However, the direction in which the flocculated emulsion droplets migrated following dilution was highly variable, as compared to the behavior observed when the SiO<sub>2</sub> suspensions were used to dilute the model emulsion. For mixtures containing 0.1, 0.2, 0.75, and 2 wt.% SiO<sub>2</sub>, the flocs that formed after 30 minutes (Figure 4-5b) displayed substantial creaming behavior. This behavior was contrary to the behavior observed for mixtures in the same set that contained 0.5 and 1 wt.% SiO<sub>2</sub>, which formed flocs that rapidly sedimented to the bottom of their respective scintillation vials following dilution and secondary mixing. After a 24-hour equilibration period (Figure 4-5d), the flocs that formed in the mixture containing 0.75 wt.% SiO<sub>2</sub> also exhibited substantial sedimentation.

One hypothesis for the source of this behavior is that adding the emulsion to the SiO<sub>2</sub> suspension causes local aggregation between the oil droplets that contact the SiO<sub>2</sub> suspension first, leaving the droplets that would contact the SiO<sub>2</sub> suspension at later times trapped within an aggregated droplet network. The effective density of these aggregates would likely be closely matched to the density of the primary oil droplets ( $\sim 0.949 \text{ g cm}^{-3}$ ), thus creaming behavior would be favored. The subtle variation in the density of these aggregates upon dilution could then be the source of variability between creaming and sedimentation. This hypothesis could be validated by studying the convergent flows of model emulsions and particulate suspensions using high-speed imaging and microcapillary microfluidic techniques.<sup>31-33</sup>

### 4.3.2 Morphology of Flocculated Oil Droplets

Representative microstructures are shown in Figure 4-6 which illustrate the flocs that formed after a 24-hour equilibration period for nanoparticle-emulsion mixtures. The aggregates in these images were formed by the addition of the aqueous SiO<sub>2</sub> suspension to the model emulsion

and subsequent vortex mixing of the mixture. In the mixture that contained 0.1 wt.% SiO<sub>2</sub> (Figure 4-6a), several small aggregates comprised of ~1-3 primary oil droplets (~3-6 μm in diameter) were observed, with most of the oil droplets remaining well-dispersed. Substantially larger aggregates (~20-50 μm in diameter) were observed in the system that contained 1 wt.% SiO<sub>2</sub> (Figure 4-6b), each comprising 10s-100s of primary oil droplets. All of oil droplets in this system were held within a larger aggregate. In the system with the highest SiO<sub>2</sub> concentration (2 wt.%, Figure 4-6c), several moderately sized aggregates (~10 μm in diameter) comprising ~5-7 oil droplets were observed, with most of the primary oil droplets not exhibiting any aggregation.

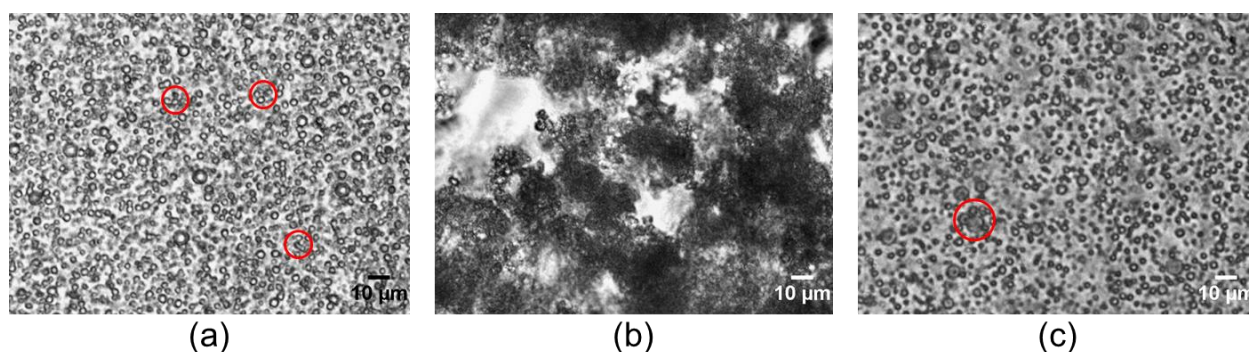


**Figure 4-6** Optical micrographs of aggregates formed within nanoparticle-emulsion mixtures with aqueous SiO<sub>2</sub> nanoparticle concentrations of 0.1 (a), 1 (b), and 2 wt.% (c) SiO<sub>2</sub> nanoparticles. Images were taken following the addition of SiO<sub>2</sub> nanoparticles to the neat emulsion, subsequent vortex mixing for 30 seconds at 2500 rpm, and a 24-hour equilibration period. Red circles highlight small and medium-sized aggregates.

It was hypothesized that the degree of SiO<sub>2</sub> interfacial adsorption attainable at different SiO<sub>2</sub> concentrations was directly responsible for the observed variability in droplet aggregation. For SiO<sub>2</sub> concentrations substantially below the value predicted by the mass balance for complete surfactant adsorption (e.g., 0.1 wt.%, Figure 4-6a), the free SiO<sub>2</sub> surface area added likely induces partial amphiphilic adsorption of the free and interfacially-adsorbed SLES molecules. However, the available SiO<sub>2</sub> surface area is insufficient for the high concentration of anionic surfactant in

the system and limits the attractive electrostatic interaction that can occur. Thus, the potential for SiO<sub>2</sub> to reduce the electrostatic stabilization of the dispersed oil droplets and drive widespread droplet flocculation is limited at lower SiO<sub>2</sub> concentrations. At SiO<sub>2</sub> concentrations substantially greater than what was determined necessary by the mass balance (e.g., 2 wt.%, Figure 4-6c), excess SiO<sub>2</sub> in the continuous aqueous phase of the mixture may form a percolated particle network which retards the gravitational phase separation of the dispersed oil droplets.

However, as the SiO<sub>2</sub> concentration approaches the value predicted by the mass balance (e.g., 0.2 wt.%, Figure 4-6b), complete neutralization of the negatively-charged SLES molecules by the positively-charged SiO<sub>2</sub> nanoparticle surfaces occurs. It is worth noting that the SiO<sub>2</sub> nanoparticles do not remove the SLES molecules from the surfaces of the dispersed oil droplets in this case. Instead, the positively-charged SiO<sub>2</sub> nanoparticles act as bridges between neighboring electrostatically-charged droplets which induce long-range floc formation. The progressive increase in the size of flocs following dilution and vortex mixing leads to the macroscopic gravitational phase separation that occurs in these systems (Figures 4-4 and 4-5). The tendency for floc sedimentation is enhanced by the increase in the effective density of the floc contributed by the integration of SiO<sub>2</sub>. The validity of the SiO<sub>2</sub> interfacial adsorption hypothesis was tested by analyzing the oil droplet-depleted regions for each nanoparticle-emulsion mixture using dynamic light scattering, the result of which are discussed in the Chapter 4.3.3.

Lastly, the primary oil droplets that comprised the flocs in the systems appeared to maintain their initial integrity, with no evidence of coalescence (interface disruption followed by droplet merging) after aggregation. Coalescence could potentially be facilitated during the prescribed droplet flocculation procedure through the utilization of hydrophobic particles with high aspect

ratios.<sup>34</sup> The anisotropy of such particles could enable penetration of droplet interfaces, thus acting as nucleation sites for droplet coalescence events.

### 4.3.3 Light Scattering Analysis of Droplet-Depleted Aqueous Regions

Size distributions corresponding to the translucent, droplet-depleted, water-rich regions for representative nanoparticle-emulsion mixtures are shown in Figure 4-7. These data are shown for systems that contained 0.2, 0.75, or 2 wt.% SiO<sub>2</sub>. Small aliquots were taken from these systems after the 24-hour equilibration period that followed dilution. For the systems that contained 0.2 wt.% SiO<sub>2</sub> (Figure 4-7a), secondary vortex mixing was found to have a noteworthy effect on the degree of gravitational phase separation that occurred. When the nanoparticle-emulsion mixture was not subjected to secondary vortex mixing after dilution, most of the oil droplets from neat emulsion remained well-dispersed. This was represented by the presence of two peaks in the size distribution at 190.1 nm and 955.4 nm (Figure 4-7a), which strongly correlated to the initial peaks of the model emulsion (Figure 4-3). Contrarily, when the nanoparticle-emulsion suspension was subjected to vortex mixing (regardless of the order-of-addition), all dispersed oil droplets > 500 nm in diameter were destabilized and phase separated. This was illustrated by the negligible scattering intensity from particles greater than 500 nm in diameter (Figure 4-7a). Additionally, the process of adding SiO<sub>2</sub> to the model emulsion was shown to be markedly more effective at removing the dispersed oil droplets than when the order of this process was inverted. This was demonstrated by the slightly higher average diameter of the droplets that remained suspended in the droplet-depleted, water-rich phase in this case (i.e., 220.2 nm).

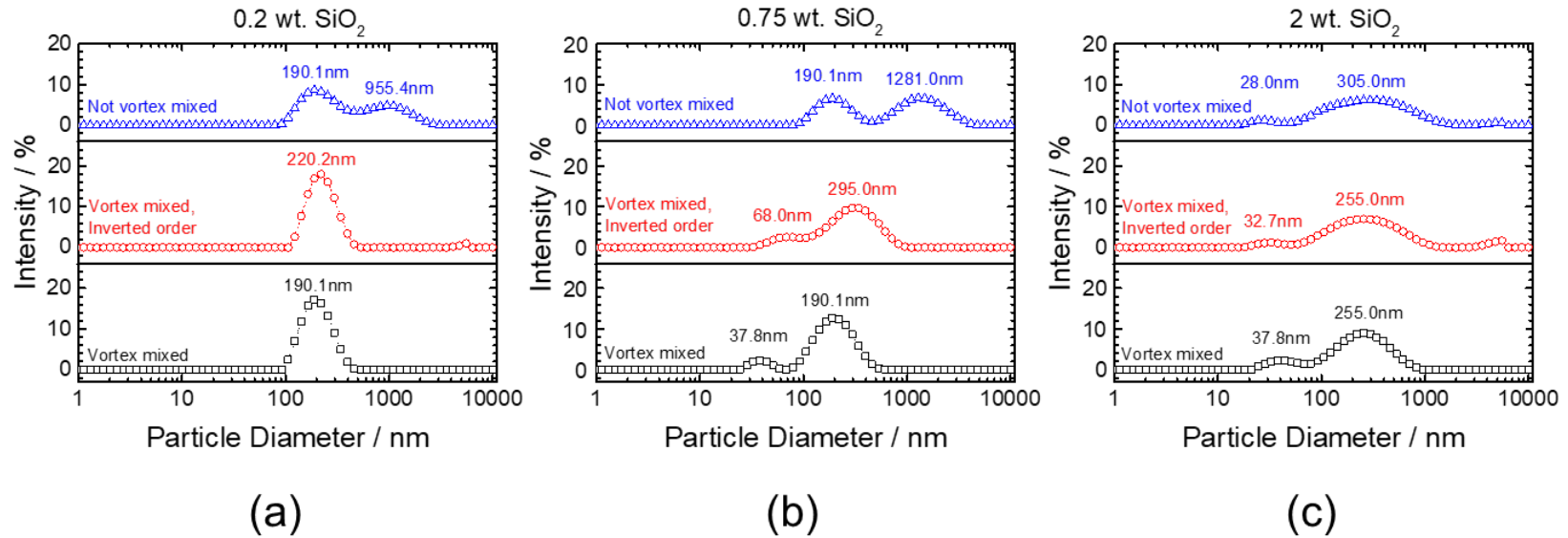


**Figure 4-7** Particle size distributions for the droplet-depleted, water-rich regions of nanoparticle-emulsion mixtures that contained (a) 0.2, (b) 0.75, and (c) 2 wt.% SiO<sub>2</sub>. Size distributions are shown for three mixing procedures: (1) where aqueous SiO<sub>2</sub> suspensions were added to the emulsion, followed by vortex mixing (black squares), (2) where the model emulsion was added to aqueous SiO<sub>2</sub> suspensions, followed by vortex mixing (red circles), and (3) where aqueous SiO<sub>2</sub> suspensions were added to the emulsion, but were not subjected to vortex mixing (blue triangles).

Dynamic light scattering data for the droplet-depleted, water-rich regions of suspension containing 0.75 and 2 wt.% SiO<sub>2</sub> (Figures 4-7b and 4-7c, respectively) provided additional support in favor of the SiO<sub>2</sub> interfacial adsorption hypothesis proposed in Chapter 4.3.2. It can be clearly seen from the data in Figure 4-7 that as the concentration of SiO<sub>2</sub> in the nanoparticle-emulsion mixture increased from 0.2 wt.% to 0.75 wt.% to 2 wt.%, the size distribution of the particles that remained dispersed in the system increased. Moreover, as the concentration of SiO<sub>2</sub> increased, the intensity of a secondary peak at ~31 nm also increased. The emergence of this secondary peak very likely corresponds to the presence of excess SiO<sub>2</sub> in the water-rich, droplet depleted region, given that the average diameter of the neat SiO<sub>2</sub> nanoparticles was measured to be 31.2 nm (Figure 4-1). The absence of this peak for the droplet-depleted regions of mixtures that contained 0.2 wt.% SiO<sub>2</sub> also implies that all the nanoparticles added to the system were incorporated into the flocs which phase separated following dilution.

It is worth noting here that some unknown proportion of oil droplets < 500 nm in diameter remained stabilized in the droplet-depleted, water-rich regions for all systems investigated. This behavior may be due to the comparable length scales of the SiO<sub>2</sub> and the nanometric oil droplets. Even in the event that the positively-charged SiO<sub>2</sub> completely neutralized and associated with all the negatively-charged oil droplets for a given system, the submicron nanoparticle-oil droplet complexes could remain stabilized by the thermal energy of the surrounding fluid. This contrasts with the dispersed oil droplets of the order of 1 μm or greater, which would have much higher surface areas available for association with SiO<sub>2</sub> nanoparticles and would ultimately be more sensitive to the enhanced gravitational effects. Removal of these submicron oil droplets could be performed by any number of the currently implemented bilge water treatment methods, such as

centrifugation<sup>7,8</sup> or ultrafiltration,<sup>9,10</sup> each of which would benefit substantially from the incorporation of the currently proposed technique as a preprocessing step.

#### 4.4 Summary

The results of this work illustrate the following: (1) Complete gravitational phase separation of electrostatically-stabilized oil-in-water emulsions can be readily induced by attractive electrostatic interactions between the anionic surfactants at the droplet interfaces and positively charged SiO<sub>2</sub> nanoparticles. (2) Rapid destabilization (< 1 hour) of all suspended oil droplets > 500 nm in diameter was observed when model emulsions were gently mixed with 0.2-1 wt.% SiO<sub>2</sub>. (3) A simple mass balance based on the saturation adsorption of the stabilizing surfactant(s) and the free surface area of the added SiO<sub>2</sub> nanoparticles can be used to predict the nanoparticle concentration required to induce widespread flocculation and phase separation of dispersed oil droplets.

The results of the present study can be readily applied to similar oil-in-water emulsions with differing physicochemical properties by utilizing the following procedure: (1) quantify the interfacial adsorptive properties of the stabilizing surfactant via interfacial tension measurements,<sup>35-37</sup> (2) measure the effective surface charge of the surfactant-stabilized oil droplets (e.g., via electrophoresis and light scattering measurements), (3) identify nanoparticles (e.g., SiO<sub>2</sub>, nanoclays, iron oxide, polymer latexes, or similar colloids) with a surface charge in the dispersion medium that is sufficiently high and opposite (positive or negative) to the surface charge of the surfactant-stabilized oil droplets, (4) approximate the nanoparticle concentration required to induce widespread droplet flocculation using the simple mass balance described herein, (5) add the necessary amount of nanoparticles to the emulsified system and follow with gentle shear mixing.

The prescribed procedure outlines a simple methodology which could be used in conjunction with many common water treatment techniques (e.g., ultrafiltration and centrifugation) to ease the strain on expensive equipment, reduce processing time, or to enhance the overall efficacy of the utilized treatment method. These results are therefore highly relevant to oil-water separation specialists that seek simple, effective, and inexpensive preprocessing strategies for the treatment of oil-in-water emulsions.

#### 4.5 References

- (1) Wilhelmsson, D.; Thompson, R. C.; Holmstrom, K.; Linden, O.; Eriksson-Hagg, H. Marine Pollution. In *Managing Ocean Environments in a Changing Climate*; 2013; pp 127–169. <https://doi.org/10.1016/B978-0-12-407668-6.00006-9>.
- (2) Karakulski, K.; Kozlowski, A.; Morawski, A. W. Purification of Oily Wastewater by Ultrafiltration. *Sep. Technol.* **1995**, *5*, 197–205. [https://doi.org/10.1016/0956-9618\(95\)00123-9](https://doi.org/10.1016/0956-9618(95)00123-9).
- (3) Jing, L.; Chen, B.; Zhang, B.; Peng, H. A Review of Ballast Water Management Practices and Challenges in Harsh and Arctic Environments. *Environ. Rev.* **2012**, *20* (2), 83–108. <https://doi.org/10.1139/a2012-002>.
- (4) Fisher, G.; Nault, P. *Bilge Water Characterization of CF Ships*; Defence R&D Canada – Atlantic, 2006.
- (5) Albert, R.; Danesi, R. Oily Bilgewater Separators. Environmental Protection Agency: Washington, DC 2011, pp 1–27.
- (6) McLaughlin, C.; Falatko, D.; Danesi, R.; Albert, R. Characterizing Shipboard Bilgewater Effluent before and after Treatment. *Environ. Sci. Pollut. Res.* **2014**, *21* (8), 5637–5652. <https://doi.org/10.1007/s11356-013-2443-x>.
- (7) Smookler, A. L.; Harden, J. W.; Conroy, P. D. NAVY DEVELOPMENT OF SUITABLE SHIPBOARD BILGE OIL/WATER SEPARATORS. In *International Oil Spill Conference Proceedings*; 1977; pp 423–428. <https://doi.org/10.7901/2169-3358-1977-1-423>.
- (8) Yang, C. Electrochemical Coagulation for Oily Water Demulsification. *Sep. Purif. Technol.* **2007**, *54*, 388–395. <https://doi.org/10.1016/j.seppur.2006.10.019>.
- (9) Jönsson, A. S.; Trägårdh, G. Ultrafiltration Applications. *Desalination* **1990**, *77* (C), 135–179. [https://doi.org/10.1016/0011-9164\(90\)85024-5](https://doi.org/10.1016/0011-9164(90)85024-5).
- (10) Gryta, M.; Karakulski, K.; Morawski, A. W. Purification of Oily Wastewater By Hybrid UF/MD. *Water Res.* **2001**, *35* (15), 3665–3669. [https://doi.org/10.1016/S0043-1354\(01\)00083-5](https://doi.org/10.1016/S0043-1354(01)00083-5).
- (11) Karakulski, K.; Morawski, W. A.; Grzechulska, J. Purification of Bilge Water by Hybrid Ultrafiltration and Photocatalytic Processes. *Sep. Purif. Technol.* **1998**, *14* (1–3), 163–173. [https://doi.org/10.1016/S1383-5866\(98\)00071-9](https://doi.org/10.1016/S1383-5866(98)00071-9).
- (12) Eskandarloo, H.; Selig, M. J.; Abbaspourrad, A. In Situ H<sub>2</sub>O<sub>2</sub> Generation for De-Emulsification of Fine Stable Bilge Water Emulsions. *Chem. Eng. J.* **2018**, *335* (October 2017), 434–442. <https://doi.org/10.1016/j.cej.2017.10.174>.
- (13) Israelachvili, J. N. *Intermolecular and Surface Forces*, 3rd ed.; 2011.

- (14) Tadros, T. F. *Applied Surfactants*; Wiley, 2005.
- (15) Coca, J.; Gutiérrez, G.; Benito, J. M. Treatment of Oily Wastewater. In *Water Purification and Management*; Coca, J., Gutiérrez, G., Eds.; Springer, 2011. <https://doi.org/10.1007/978-90-481-9775-0>.
- (16) Eskandar, N. G.; Simovic, S.; Prestidge, C. A. Synergistic Effect of Silica Nanoparticles and Charged Surfactants in the Formation and Stability of Submicron Oil-in-Water Emulsions. *Phys. Chem. Chem. Phys.* **2007**, *9* (48), 6426–6434. <https://doi.org/10.1039/b710256a>.
- (17) Binks, B. P.; Rodrigues, J. A.; Frith, W. J. Synergistic Interaction in Emulsions Stabilized by a Mixture of Silica Nanoparticles and Cationic Surfactant. *Langmuir* **2007**, *23* (7), 3626–3636. <https://doi.org/10.1021/la0634600>.
- (18) Binks, B. P.; Rodrigues, J. A. Enhanced Stabilization of Emulsions Due to Surfactant-Induced Nanoparticle Flocculation. *Langmuir* **2007**, *23* (14), 7436–7439. <https://doi.org/10.1021/la700597k>.
- (19) Santini, E.; Guzmán, E.; Ferrari, M.; Liggieri, L. Emulsions Stabilized by the Interaction of Silica Nanoparticles and Palmitic Acid at the Water-Hexane Interface. *Colloids Surfaces A Physicochem. Eng. Asp.* **2014**, *460*, 333–341. <https://doi.org/10.1016/j.colsurfa.2014.02.054>.
- (20) Katepalli, H.; Bose, A.; Hatton, T. A.; Blankschtein, D. Destabilization of Oil-in-Water Emulsions Stabilized by Non-Ionic Surfactants: Effect of Particle Hydrophilicity. *Langmuir* **2016**, *32* (41), 10694–10698. <https://doi.org/10.1021/acs.langmuir.6b03289>.
- (21) Chanamai, R.; McClements, D. J. Creaming Stability of Flocculated Monodisperse Oil-in-Water Emulsions. *J. Colloid Interface Sci.* **2000**, *225* (1), 214–218. <https://doi.org/10.1006/jcis.2000.6766>.
- (22) Van der Meeren, P.; Saveyn, H.; Bogale Kassa, S.; Doyen, W.; Leysen, R. Colloid-Membrane Interaction Effects on Flux Decline during Cross-Flow Ultrafiltration of Colloidal Silica on Semi-Ceramic Membranes. *Phys. Chem. Chem. Phys.* **2004**, *6* (7), 1408. <https://doi.org/10.1039/b315220k>.
- (23) Safouane, M.; Langevin, D.; Binks, B. P. Effect of Particle Hydrophobicity on the Properties of Silica Particle Layers at the Air-Water Interface. *Langmuir* **2007**, *23* (23), 11546–11553. <https://doi.org/10.1021/la700800a>.
- (24) Hunter, T. N.; Jameson, G. J.; Wanless, E. J. Determination of Contact Angles of Nanosized Silica Particles by Multi-Angle Single-Wavelength Ellipsometry. *Aust. J. Chem.* **2007**, *60* (9), 651–655. <https://doi.org/10.1071/CH07133>.
- (25) Carole, T. M. *Solids Separation and Concentration of Shipboard Wastewaters and Residuals by a High-Shear Rotary Membrane System*; 2015; Vol. 2.

- (26) Xu, H.; Li, P. X.; Ma, K.; Thomas, R. K.; Penfold, J.; Lu, J. R. Limitations in the Application of the Gibbs Equation to Anionic Surfactants at the Air/Water Surface: Sodium Dodecylsulfate and Sodium Dodecylmonooxyethylenesulfate above and below the CMC. *Langmuir* **2013**, *29* (30), 9335–9351. <https://doi.org/10.1021/la401835d>.
- (27) Ravera, F.; Santini, E.; Loglio, G.; Ferrari, M.; Liggieri, L. Effect of Nanoparticles on the Interfacial Properties of Liquid/Liquid and Liquid/Air Surface Layers. *J. Phys. Chem. B* **2006**, *110* (39), 19543–19551. <https://doi.org/10.1021/jp0636468>.
- (28) Liggieri, L.; Santini, E.; Guzmán, E.; Maestro, A.; Ravera, F. Wide-Frequency Dilational Rheology Investigation of Mixed Silica Nanoparticle–CTAB Interfacial Layers. *Soft Matter* **2011**, *7* (17), 7699. <https://doi.org/10.1039/c1sm05257h>.
- (29) Eliceiri, K.; Schneider, C. A.; Rasband, W. S.; Eliceiri, K. W. NIH Image to ImageJ : 25 Years of Image Analysis. *Nat. Methods* **2012**, *9* (7), 671–675. <https://doi.org/10.1038/nmeth.2089>.
- (30) Kimoto, S.; Dick, W. D.; Hunt, B.; Szymanski, W. W.; Mcmurry, H.; Roberts, D. L.; Pui, D. Y. H.; Kimoto, S.; Dick, W. D.; Hunt, B.; et al. Characterization of Nanosized Silica Size Standards. *Aerosol Sci. Technol.* **2017**, *51* (8), 936–945. <https://doi.org/10.1080/02786826.2017.1335388>.
- (31) Anna, S. L. Droplets and Bubbles in Microfluidic Devices. *Annu. Rev. Fluid Mech.* **2016**, *48* (1), 285–309. <https://doi.org/10.1146/annurev-fluid-122414-034425>.
- (32) Martinez, C. J.; Kim, J. W.; Ye, C.; Ortiz, I.; Rowat, A. C.; Marquez, M.; Weitz, D. A Microfluidic Approach to Encapsulate Living Cells in Uniform Alginate Hydrogel Microparticles. *Macromol. Biosci.* **2012**, *12* (7), 946–951. <https://doi.org/10.1002/mabi.201100351>.
- (33) Nash, J. J.; Spicer, P. T.; Erk, K. A. Controllable Internal Mixing in Coalescing Droplets Induced by the Solutal Marangoni Convection of Surfactants with Distinct Headgroup Architectures. *J. Colloid Interface Sci.* **2018**, *529*, 224–233. <https://doi.org/10.1016/j.jcis.2018.06.011>.
- (34) Thiel, A. E.; Hartel, R. W.; Spicer, P. T.; Hendrickson, K. J. Coalescence Behavior of Pure and Natural Fat Droplets Characterized via Micromanipulation. *J. Am. Oil Chem. Soc.* **2016**, *93* (11), 1–11. <https://doi.org/10.1007/s11746-016-2896-4>.
- (35) Rotenberg, Y.; Boruvka, L.; Neumann, A. . Determination of Surface Tension and Contact Angle from the Shapes of Axisymmetric Fluid Interfaces. *J. Colloid Interface Sci.* **1983**, *93* (1), 169–183. [https://doi.org/10.1016/0021-9797\(83\)90396-X](https://doi.org/10.1016/0021-9797(83)90396-X).
- (36) Berry, J. D.; Neeson, M. J.; Dagastine, R. R.; Chan, D. Y. C.; Tabor, R. F. Measurement of Surface and Interfacial Tension Using Pendant Drop Tensiometry. *J. Colloid Interface Sci.* **2015**, *454*, 226–237. <https://doi.org/10.1016/j.jcis.2015.05.012>.

- (37) Nash, J. J.; Erk, K. A. Stability and Interfacial Viscoelasticity of Oil-Water Nanoemulsions Stabilized by Soy Lecithin and Tween 20 for the Encapsulation of Bioactive Carvacrol. *Colloids Surfaces A Physicochem. Eng. Asp.* **2017**, *517*, 1–11. <https://doi.org/10.1016/j.colsurfa.2016.12.056>.

## **CHAPTER 5      CONTROLLABLE INTERNAL MIXING BETWEEN COALESCING DROPLETS INDUCED BY THE SOLUTAL MARANGONI CONVECTION OF SURFACTANTS WITH DISTINCT HEADGROUP ARCHITECTURES**

Portions of the following chapter contain text and figures adapted (with permission from **J.J. Nash**, P.T. Spicer, and K.A. Erk) from the article, “Controllable internal mixing in coalescing droplets induced by the solutal Marangoni convection of surfactants with distinct headgroup architectures,” *J. Colloid Interface Sci.*, 529, 224-233, (2018) Copyright 2018 Elsevier Inc., DOI: 10.1016/j.jcis.2018.06.011

### **5.1 Introduction**

The coalescence of two identical droplets, and the corresponding bulk fluid flows that emerge, has been studied at length in the literature.<sup>1-5</sup> However, far less attention has been given to the coalescence of binary droplets with asymmetric physical properties, despite its importance to many industrial and research applications including enhanced oil recovery<sup>6</sup>, emulsification<sup>7</sup>, microfluidic reactors<sup>8</sup>, and functional microparticle fabrication.<sup>9-11</sup>

Many additional examples can be found in the literature of microfluidic applications that utilize the coalescence of droplets as a vital processing step in material fabrication. However, mixing immiscible phases in microfluidic devices often proves difficult because of the low Reynolds number flows encountered within microchannels. Several researchers have shown that the combination of immiscible fluids in microchannels can be improved with modified channel designs<sup>12-14</sup> or, quite often, by modulating the viscosity of one or both of the coalescing fluids to achieve desired bulk convective mixing.<sup>15,16</sup> While several detailed coalescence studies have investigated the effects of variable external oil phase viscosity on the generation of bulk flows in

coalescing water droplets,<sup>17,18</sup> little attention was given to the potential influence of polar surfactant headgroup architecture in the generation of the observed opposing interfacial and bulk flows. Moreover, altering the viscosities of the bulk fluids is not always a viable option in microfluidic applications (for example, when high throughput is a processing requirement, or when a system is restricted to fluids with predetermined viscosities). Thus, additional routes for inducing a similar degree of internal mixing under these restrictions are necessary, and currently, no experimental studies in the literature have sought to provide insight into how appropriate surfactant selection can influence this phenomenon.

Utilizing solutal Marangoni convection, also known as the Gibbs-Marangoni effect,<sup>19,20</sup> provides a compelling avenue for inducing desired bulk flows in coalescing binary fluid systems, without the need for modulating bulk fluid viscosity. The Gibbs-Marangoni effect can be induced simply by adding a dilute concentration of a highly surface-active solute to one of the fluid droplets, while keeping the second drop initially free of any surfactant, then bringing the droplets into contact. When the two fluid droplets coalesce, a highly curved connective liquid bridge forms between them and expands rapidly due to interfacial stresses. In the inertial regime, a scaling relation derived from a simple physical argument can be used to describe the expansion of the coalescence bridge.<sup>4</sup> This scaling law predicts linear proportionality between the radius of the connective liquid bridge,  $r_b$  ( $= D_b/2$ ), and the square root of the coalescence time,  $t^{1/2}$ , given by the equation,  $D_b/2 \propto (R\gamma/\rho_{out})^{1/4}t^{1/2}$ , where  $R$  is the initial drop radius,  $\gamma$  is the interfacial tension, and  $\rho_{out}$  is the density of the outer fluid.

As bridge expansion proceeds, the resulting fluid motion acts to pull the droplets together to form a single, larger drop. However, in the presence of an induced surface tension (i.e., surfactant concentration) gradient between the droplets, opposing interfacial and bulk flows can emerge. This

is because surfactant molecules become nonuniformly distributed at the interface along the highly curved, connective liquid bridge separating the surfactant-laden and surfactant-free drops.<sup>21</sup> Relaxation to a homogenous surfactant coverage does not proceed primarily by diffusion, but by a far more rapid process (i.e., the Gibbs-Marangoni effect) where the surfactant molecules at the interface swiftly migrate toward regions of highest local interfacial tension. This in turn generates interfacial motion in the direction of the surfactant concentration gradient that acts tangentially to the merging droplets, which is accompanied by bulk motion in the adjacent fluid layers. Consequently, bulk flows which drive the droplets together under the influence of a favorable reduction in capillary pressure,  $\Delta P = 2\gamma/R$ , become unbalanced with interfacial flows. This ultimately results in opposing interfacial and bulk convective motion and can lead to pronounced bulk fluid mixing.

It has been shown that the mobility<sup>22</sup>, as well as the degree of equilibrium interfacial adsorption of low molecular weight surfactants<sup>23,24</sup>, can vary substantially depending on the nature of the surfactant's polar headgroup in a polar solvent such as water (i.e., whether it is anionic, cationic, nonionic, or zwitterionic). These interfacial characteristics are also well-known to have demonstrated importance in the occurrence of film rupture and coalescence for surfactant-laden fluid interfaces.<sup>25,26</sup> Therefore, it would stand to reason that strategically modulating the interfacial mobility, equilibrium saturation adsorption, and adsorption-desorption kinetics of the added surfactant would enable interested parties to control coalescence related phenomena, such as passively-induced internal mixing between emulsion droplets in the presence of a surfactant concentration gradient. Optimized design of such small-scale processes will require the ability to identify appropriate surfactants based on their physicochemical properties and performance in applications like diagnostic chips and other microfluidics systems. Thus, this work seeks to

demonstrate several key mechanisms relating the adsorption of two oppositely charged ionic surfactants and the manifested solutal Marangoni flows that drive bulk mixing between coalescing aqueous droplets in a viscous surrounding oil. Generalized relationships between the interfacial properties of low molecular weight surfactant and their potential influence on bulk coalescing phenomena are also provided.

Many detailed experimental and theoretical analyses have been performed which elucidate early-stage coalescence phenomena of uniform liquid droplets both in air and an external liquid.<sup>1-5</sup> However, fully developed mixing behaviors in the later stages of coalescence (i.e., several milliseconds following the onset of coalescence) are often a primary concern in microfluidic reactor applications.<sup>8,27</sup> Therefore, to aid in the design of such systems, the specific aims of this work were to (1) investigate the late-stage coalescence behavior of binary liquid droplets with an induced surfactant concentration gradient along the connective liquid bridge, and (2) illustrate how controlling equilibrium adsorption and solutal Marangoni motion through appropriate surfactant selection can encourage varying degrees of bulk fluid mixing. Through several complementary experiments, including equilibrium surfactant adsorption measurements, high-speed image processing, and concentration gradient-induced interfacial velocity measurements via particle tracking, we provide new insights into the fundamental relationships between optimized surfactant selection and bulk fluid mixing. Considering that the adsorption and interfacial spreading behavior of surfactants can vary dramatically depending on the electrostatic interactions of the surfactant present at the fluid interface in the bulk aqueous solution<sup>28</sup>, detailed investigations which further elucidate the role of surfactant selection in the development of varying degrees of opposing flows within coalescing binary droplets are essential.

## 5.2 Materials and Experimental Methods

### 5.2.1 Materials

The external liquid phase used during drop coalescence measurements was a triglyceride oil (Stepan Company, CAS Registry No. 73398-61-5) with a reported viscosity of 25 mPa·s and density of 0.95 g cm<sup>-3</sup>, both at 25 °C. The oil was double-filtered through a chromatography column containing alumina (Fisher, CAS Registry No. 1344-28-1) to remove trace surface-active impurities prior to use. The droplets consisted of aqueous solutions prepared with water passed through a Filmtec™ reverse osmosis membrane (total dissolved solids ≤ 15 ppm, Dow Chemical Company). The two commercially available surfactants used in this study, ammonium lauryl sulfate, ALS (anionic surfactant, 30% in water, CAS Registry No. 2235-54-3) and cetyltrimethylammonium bromide, CTAB (cationic, ≥ 99%, CAS Registry No. 57-09-0), were obtained from Sigma-Aldrich and used without further purification. The blue dye added to the surfactant-free droplet in each droplet coalescence measurement used as an aid for visualizing bulk motion was purchased from Queen Fine Foods Pty Ltd. The flat metal capillaries (18-gauge x 1.0” blunt tip dispensing needles) used in coalescence experiments were obtained from CML Supply.

### 5.2.2 Visualizing Rapid Binary Drop Coalescence

A schematic of the experimental setup used for visualizing binary liquid droplet coalescence is shown in Figure 5-1. Experiments were performed using a pair of three-axis micromanipulators (Sensapex) secured to z-axis translational stages (THORLABS) flanking an inverted optical microscope (AE31, Motic Microscopes). Two water droplets with asymmetric compositional properties, each having an initial diameter of 2 mm (unless otherwise specified) were formed at the tips of 18-gauge metal capillaries and were made to contact at negligible approach velocities (~0.01 mm s<sup>-1</sup>) in a clear petri dish containing the low viscosity triglyceride

oil (5 mL working volume). Coalescence of the binary droplets was captured with a high-speed camera (Phantom v7.3) at 11000 frames per second. Measurements of the bridge expansion kinetics were performed via image processing using open-source ImageJ software.<sup>29</sup>

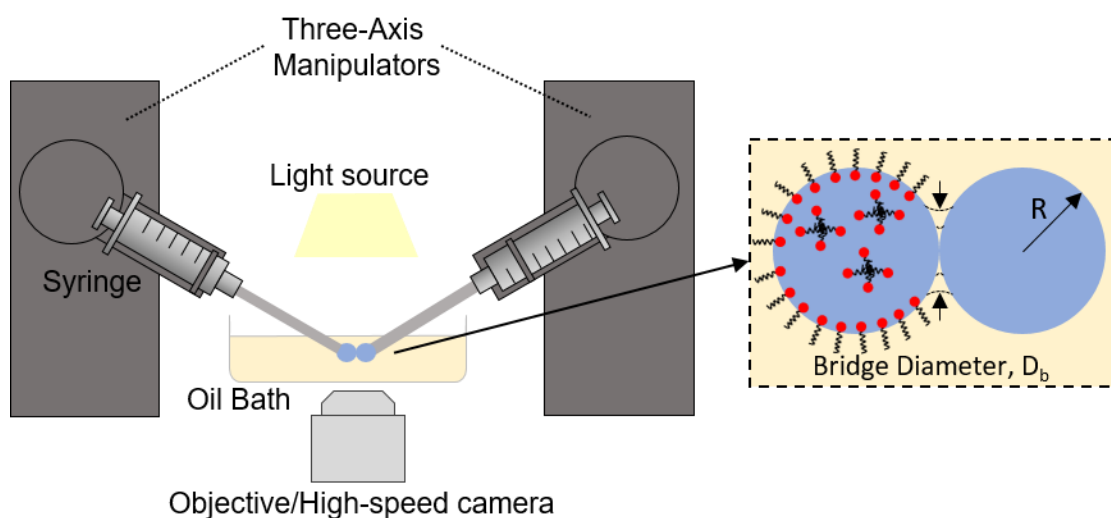


**Figure 5-1** An illustration of the experimental setup used to study coalescence between binary aqueous droplets in a surrounding oil. The leftmost aqueous droplet was laden with surfactant and the rightmost droplet was surfactant-free, yet contained a small concentration of dye to aid in flow visualization.

A concentration gradient along the connective liquid between the two merging water drops was generated by adding the surfactant of interest to the leftmost coalescing droplet (Figure 5-1), while keeping the rightmost droplet surfactant-free. The surfactant-loaded droplet in each experiment contained either ALS or CTAB at a concentration of  $2.5 \times 10^{-3} \text{ mol L}^{-1}$ , which was near the experimentally determined critical micelle concentration (CMC) for each surfactant type. The relevant data used in determining the CMC for each surfactant is provided in Chapter 5.2.3. This initial bulk surfactant concentration was chosen because near and above the CMC, the chemical potential of the surfactant negligibly changes and as a result conditions at the interface do not change.<sup>30</sup> Thus, the surfactant-laden droplet interface in this experimental setup represents an

interfacial monolayer near saturation equilibrium. At the chosen bulk concentration, the equilibrium interfacial tension of the oil-water interface was  $3.40 \pm 0.48 \text{ mN m}^{-1}$  for ALS and  $3.01 \pm 0.41 \text{ mN m}^{-1}$  for CTAB, as determined by the drop shape analysis technique (Chapter 5.2.3).

To help visualize the emergent bulk fluid motion during droplet coalescence, dye was added to the surfactant-free droplet at a concentration of  $0.1 \text{ g L}^{-1}$ . The addition of dye did not substantially affect the oil-water interfacial tension (surfactant-free, pure droplet:  $\gamma = 23.67 \pm 0.13 \text{ mN m}^{-1}$ ; surfactant-free, dyed droplet:  $\gamma = 21.42 \pm 0.27 \text{ mN m}^{-1}$ ), and thus its contribution to the emergent coalescence flows was presumed to be negligible in comparison to the presence of the highly surface-active molecules, ALS and CTAB.

### 5.2.3 Determination of Interfacial Adsorptive Properties at the Oil-Water Interface

Interpreting the relationship between the induced bulk flows and the contributing interfacial Marangoni stresses of coalescing binary droplets requires knowledge of the equilibrated interfacial adsorption for each surfactant-laden droplet prior to merging. The effective interfacial tension values for pure and surfactant-laden oil-water interfaces were obtained using axisymmetric drop shape analysis with a contact angle goniometer/tensiometer (Ramé-Hart) following experimental procedures established in previous work by Nash and Erk.<sup>31</sup> The theory underpinning this technique and its corresponding application to study the effective interfacial tensions for air-liquid and liquid-liquid monolayers have been previously discussed in the literature.<sup>32,33</sup> In brief, the interfacial tension of each oil-water interface was determined by fitting the shape profile of an aqueous pendant drop suspended from the tip of a flat 12-gauge PTFE capillary immersed in oil to the theoretical profile prescribed by the Young-Laplace equation,  $\Delta P = \gamma \left( \frac{1}{R_1} + \frac{1}{R_2} \right)$ . This force balance relates the differential in pressure,  $\Delta P$ , across a curved interface to its principle radii of curvature  $R_1$  and  $R_2$ , and interfacial tension,  $\gamma$ . As surface active solutes become adsorbed to the

interface, there is a demonstrable reduction in the capillary pressure. For a known pressure and interfacial curvature, the effective interfacial tension of the surfactant-laden interface can be directly measured.

The equilibrium interfacial adsorption isotherms for dilute aqueous solutions of ALS or CTAB in contact with triglyceride oil are provided in Figure 5-2. In each adsorption experiment, the interfacial tension was measured over time for at least 45 minutes, or until a constant interfacial tension value was reached. The critical micelle concentration (CMC's) for each surfactant was determined graphically from Figure 5-2 as the intersection of the linear fits to the low and high concentration regimes for each surfactant. Experimental CMC values for ALS and CTAB at 23 °C were ca.  $5.5 \times 10^{-3} \text{ mol L}^{-1}$  and  $0.95 \times 10^{-3} \text{ mol L}^{-1}$ , respectively. The CMC value obtained here for ALS closely corresponded to the value found in the literature,  $6.25 \times 10^{-3} \text{ mol L}^{-1}$ .<sup>34</sup> Likewise, the CMC value obtained here for CTAB agreed well with previous observations in the literature of  $0.9 \times 10^{-3} \text{ mol L}^{-1}$ <sup>35</sup> and  $1 \times 10^{-3} \text{ mol L}^{-1}$ .<sup>36</sup>

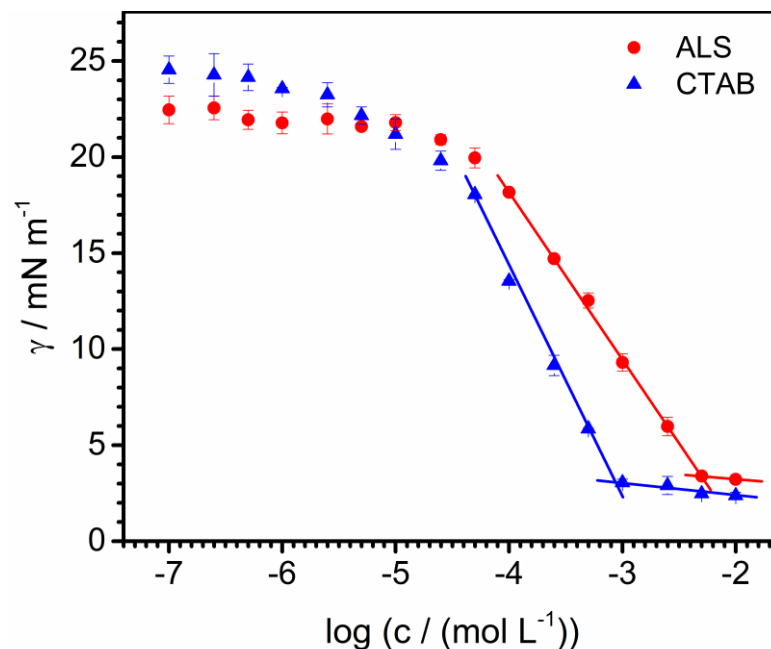


**Figure 5-2** Interfacial tension,  $\gamma$ , versus log of surfactant concentration,  $c$ , in aqueous solution at 23 °C at the triglyceride oil-water interface measured by the drop shape analysis technique. Lines represent best-fitting straight lines of the data in the low and high surfactant concentration regimes for each surfactant. The slope value of the best-fitting line in the low surfactant concentration regime was used in the determination of the surface excess concentration,  $\Gamma_m$ , for ALS and CTAB.

The surface excess concentration,  $\Gamma_m$ , corresponds to the maximum concentration of surfactant adsorbed to the oil-water interface of the surfactant-laden droplet at equilibrium and was approximated for each surfactant using the Gibbs adsorption equation,  $\Gamma_m = -\frac{1}{mRT} \left( \frac{d\gamma}{d \log c} \right)_{T,P}$ , where  $\gamma$  is the interfacial tension ( $\text{mN m}^{-1}$ ),  $c$  is the bulk surfactant concentration ( $\text{mol L}^{-1}$ ),  $R$  is the gas constant,  $T$  is the temperature (K), and the integer,  $m$ , accounts for the charge interactions within the polar head group of the surfactant. For dilute aqueous solutions containing a single, 1:1 ionic surfactant in the absence of excess salt,  $m = 4.606$ , which was taken for both anionic ALS and cationic CTAB.<sup>37,38</sup> Substituting the slope value of the best-fitting straight line in the low surfactant concentration regime from the interfacial tension versus log of surfactant concentration curve for  $\frac{d\gamma}{d \log c}$  in the Gibbs adsorption equation,  $\Gamma_m$  was calculated for ALS and CTAB at the

triglyceride oil-water interface. The minimum molecular area,  $A_{\min}$  ( $\text{\AA}^2 \text{ molecule}^{-1}$ ), was then determined from the equation,  $A_{\min} = \frac{1 \times 10^{20}}{\Gamma_m N_A}$ , where  $N_A$  is Avogadro's number. (Table 5-1).

**Table 5-1** Surface excess concentrations and minimum molecular areas calculated for ALS and CTAB at 23 °C at the triglyceride oil-water interface.

Surfactant	Surface Excess Concentration, $\Gamma_m / (10^{-6} \text{ mol m}^{-2})$	Minimum Molecular Area, $A_{\min} / (\text{\AA}^2 \text{ molecule}^{-1})$
Ammonium Lauryl Sulfate (ALS)	0.76	218
Cetyltrimethylammonium bromide (CTAB)	1.07	156

#### Determination of Surfactant-Induced Interfacial Spreading Velocity, $U_s$

The experimental setup used to study the interfacial spreading velocity,  $U_s$ , of each surfactant when introduced into the pure triacylglyceride oil-water interface is shown in Figure 5-3. The displacement of tracer particles (hollow glass spheres, 9-13  $\mu\text{m}$  diameter, Sigma-Aldrich, CAS Registry No. 65997-17-3) seeded at the pure oil-water interface initiated by the introduction of a surfactant-loaded water droplet to the pure oil-water interface and driven by solutal Marangoni flow was measured.

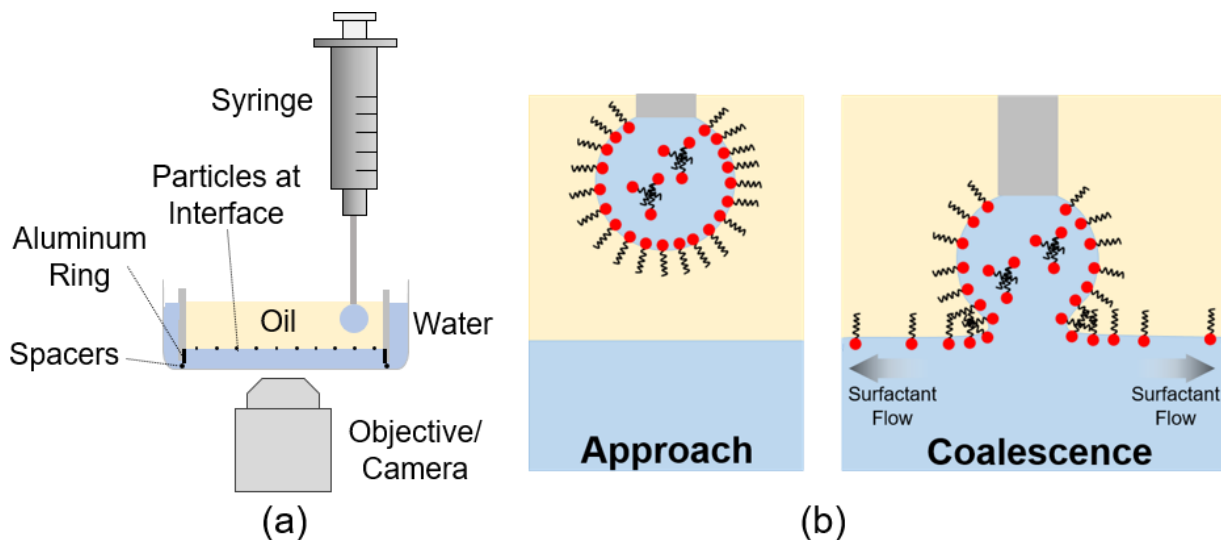


**Figure 5-3** Schematic representation of the experimental setup used to quantify interfacial spreading velocities,  $U_s$ , under an induced interfacial tension gradient at the triglyceride oil-water interface. A side view depicting the introduction of a surfactant loaded water droplet at the surfactant-free, oil-water interface (containing tracer particles) is shown in (a) and an illustration of the surfactant diffusion mechanism, quantified by measuring the rate of displacement for tracer particles attached to the interface, is shown in (b).

The motion of tracer particles was measured at a planar oil-water interface because this experimental scheme specifically enabled the measurement of Marangoni-induced flow rates under the effect of a surfactant concentration gradient at the oil-water interface. Ensuring that the measured flow rates were obtained for tracer particles located specifically at the oil-water interface and not within one of the subphases was most directly accomplished with a droplet coalescing with a planar oil-water interface.

Preparation of a planar triglyceride oil-water interface containing the seeded glass spheres was performed using a modified optical microscopy cell and methodology adapted from the work of Park et al.<sup>39</sup> The cell used here consisted of a polystyrene petri dish (height 1 cm, outer diameter of 40 mm) and a concentric polystyrene cylinder (height 1 cm, outer diameters of 30 mm). An aluminum ring was inserted into the bottom of the inner polystyrene cylinder to pin the contact line of the oil-water interface. The inner cylinder was secured to the polystyrene petri dish using a

fast curing epoxy and 0.1 mm glass spacers. This allowed for the oil-water system to achieve hydrostatic equilibrium, ensuring that a planar oil-water interface could be attained via the addition or removal of water from the outer portion of the sample cell.

After forming a planar oil-water interface free of any solutes, an oil droplet containing tracer particles was directly added to the upper oil phase of the sample cell. This yielded a seeded tracer concentration of  $\sim 4 \times 10^6$  particles- $\text{cm}^{-2}$  at the interface, a concentration which was necessary for accurate particle tracking measurements and quantifying the interfacial spreading velocities resulting from the introduction of surfactant. It should be noted that at this concentration, seeded tracer particles displayed slight aggregation. Very large aggregates would be expected to display lower interfacial spreading velocities in comparison to unaggregated primary particles due to their larger mass and could therefore introduce some degree of uncertainty into the measured interfacial spreading velocities in this experimental setup. However, the largest aggregates observed in this study consisted of 2-3 primary particles, and measurements of the steady-state, fully developed displacement rates for these aggregates were indistinguishable from the measured displacement rates of unaggregated, interfacially adsorbed primary particles.

Following the seeding of tracer particles, the experimental cell was stabilized for 15 minutes, then a 10  $\mu\text{L}$  droplet of either surfactant solution was formed at the tip of a metal capillary within the oil layer. The droplet was equilibrated for an additional 30 minutes within the upper oil layer prior to contact with the planar oil-water interface to allow for saturated interfacial adsorption of the surfactant. Finally, the droplet was lowered slowly ( $\sim 0.01$  mm  $\text{s}^{-1}$ ) to contact the planar oil-water interface and the resulting isotropic tracer particle motion was captured using an inverted microscope and high-speed camera (Photron Mini UX) at 2000 frames per second. Due to the remarkably high energy of attachment for micrometer-scale particles at the oil-water interface,<sup>40</sup>

particle motion was presumed to be approximately two-dimensional for the duration of particle spreading. Care was taken to quantify the displacement of at least five tracer particles from two separate experiments for each oil-water-surfactant system, measured manually using ImageJ software.

## 5.3 Results and Discussion

### 5.3.1 Effect of Surfactant Type on Bridge Expansion and Internal Mixing

Our investigation of surfactant contributions in the generation of opposing flows within coalescing binary droplets begins with the consideration of two surfactant-free droplets sharing an equivalent initial diameter,  $2R$  ( $= 2$  mm), and approximately equal oil-water interfacial tensions (surfactant-free, undyed droplet:  $\gamma_1 = 23.67 \pm 0.13$  mN m<sup>-1</sup>; surfactant-free, dyed droplet:  $\gamma_2 = 21.42 \pm 0.27$  mN m<sup>-1</sup>). Analysis of bridge expansion for the two, equally sized coalescing droplets with no added surfactant revealed that this system closely obeyed the  $D_b/2 \propto (R\gamma/\rho_{out})^{1/4}t^{1/2}$  scaling relation over the entire duration of droplet merging (Figure 5-4), agreeing well with the experimental observations of previous researchers.<sup>17,18</sup>

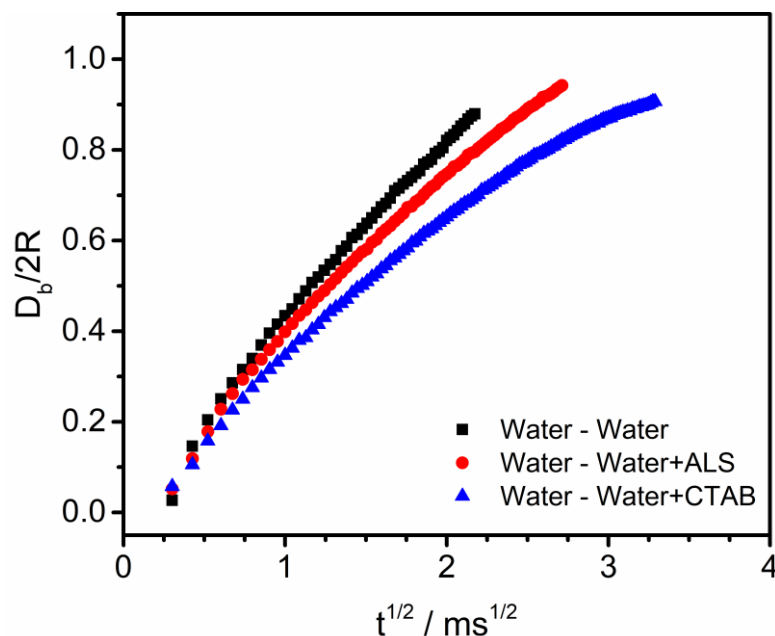


**Figure 5-4** Kinetics of expansion for the connective bridge separating spherical droplets with an equivalent initial diameter,  $2R$  ( $= 2$  mm). The data represent the increase in the connective bridge diameter,  $D_b$ , relative to  $2R$ , as a function of the square-root-of-time,  $t^{1/2}$ , succeeding the onset of droplet coalescence.

For equally sized coalescing droplets, where one of the drops contained  $2.5 \times 10^{-3} \text{ mol L}^{-1}$  ALS, the  $D_b/2 \propto t^{1/2}$  scaling relation was also closely obeyed, but a slightly reduced slope in the experimental data was observed. This indicates that the value of the prefactor,  $(R\gamma/\rho_{\text{out}})^{1/4}$ , in the coalescence scaling relation was influenced by the presence of ALS. Likewise, an even more pronounced decrease in the slope of this scaling relationship became apparent at longer times for systems containing  $2.5 \times 10^{-3} \text{ mol L}^{-1}$  CTAB. This further suggests that the gradient in interfacial tension and timescale of solutal Marangoni flow of the chosen surfactant along the interface of expanding liquid bridge has a demonstrable influence on the value of the prefactor in the scaling relation, which was not explicitly accounted for or discussed in the derivation of this scaling relation.

The characteristic time scale for coalescence of two equally sized drops with equal interfacial tensions in inviscid flow is set by  $\tau_c = \sqrt{(\rho R^3)/\gamma}$ .<sup>41</sup> For the merging of two 0.75-mm

radius water drops in the inertial regime, with  $\gamma = 23 \text{ mN m}^{-1}$ ,  $\tau_C$  is  $\sim 4.2 \text{ ms}$ . This characteristic relaxation time closely approximates the experimentally measured time required for the expanding bridge between the surfactant-free water droplets to become equal to the initial drop diameter for the system shown in Figure 5-5a. This approximation is less representative in the presence of a surfactant concentration gradient, which can be seen from the data in Figure 5-5b and 5c, for ALS and CTAB, respectively. Each of these systems require a longer duration for the diameter of the expanding bridge to be equal to the initial diameter of the drops. The observed increase in  $\tau_C$  for systems containing ALS or CTAB, as well as the clear difference between their corresponding  $\tau_C$  values, suggests that interfacial adsorptive and convective properties of the surfactant contribute to the decrease in the value of the prefactor in the coalescence scaling relation. This observation is discussed in greater detail in Chapter 5.3.3.

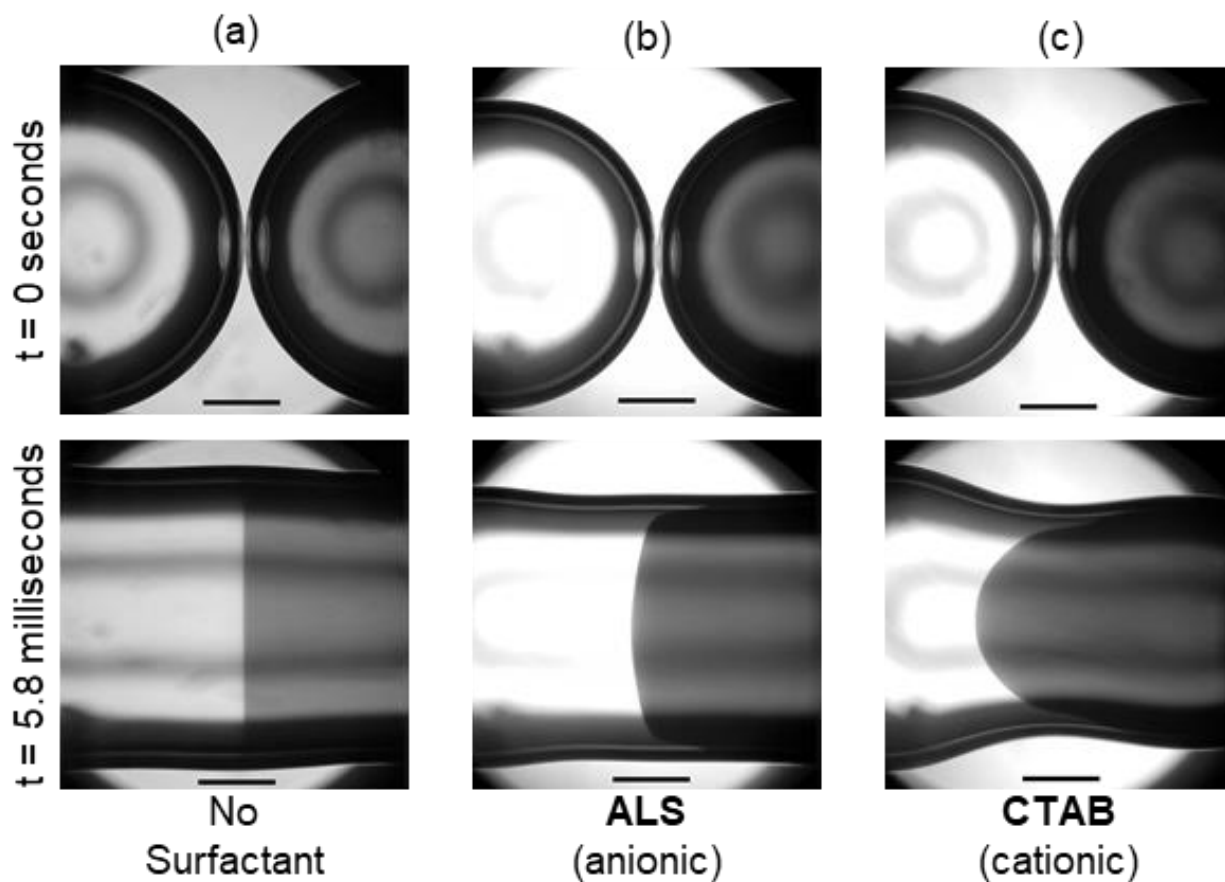


**Figure 5-5** Temporal shape profiles of equally sized water droplets coalescing in triglyceride oil. The leftmost droplet in each image contained either (a) no surfactant, (b)  $2.5 \times 10^{-3} \text{ mol L}^{-1}$  ALS, or (c)  $2.5 \times 10^{-3} \text{ mol L}^{-1}$  CTAB, while the rightmost droplet in each image was surfactant-free, with dye added for flow visualization. The absence or presence of opposing flows at the interface and within the bulk of the merging droplets illustrate the effect of interfacially adsorbed surfactant molecules. Differences in the curvature of the jetted fluid following coalescence in (b) and (c) demonstrate the influence of surfactant headgroup architecture on the relative magnitude of these induced flows. The scale bars in each image are 0.5 mm in length.

Figure 5-5a illustrates that negligible internal mixing occurred during the merging of surfactant-free droplets due to the generation of two balanced, plug-flow water jets which converged at the propagating coalescence neck. In this instance, the interfacial tensions of the converging droplets are balanced and thus no tangential stress was competing with the bulk fluid motion of the merging drops. This behavior agreed well with experimental observations of previous researchers.<sup>17,18</sup> Contrarily, coalescence of binary droplets with non-uniform

compositions of a surface-active species displayed pronounced internal convective mixing during coalescence, the degrees of which strongly depended on the surfactant present at the oil-water interface of the surfactant-laden droplet.

Distinct bulk fluid motion was observed in the presence of either anionic ALS or cationic surfactant CTAB for equally sized droplet with a capillary pressure ratio of  $\Delta P_2/\Delta P_1 \approx 5$  (where  $\Delta P_1$  and  $\Delta P_2$  are the capillary pressures of the leftmost droplet and the rightmost droplet, respectively) and are shown in Figures 5-5b and 5-5c. The presence of surfactant in the undyed, leftmost drop led to the formation of a fluid jet which propagated from the bulk of dyed, surfactant-free drop as direct result of this droplet's higher capillary pressure. For the binary droplets system containing  $2.5 \times 10^{-3} \text{ mol L}^{-1}$  ALS, the motion of the jetted fluid appeared to occur under near plug flow conditions, with some discernable curvature of the jetting dyed fluid at later times. However, the internal mixing for the binary systems containing  $2.5 \times 10^{-3} \text{ mol L}^{-1}$  CTAB was demonstrably more pronounced, displaying a much higher curvature of the jetted fluid at later stages of coalescence (i.e., after 5.8 milliseconds).

### **5.3.2 Influence of Surfactant Type on the Development of Bulk Fluid Jetting**

To further aid in illustrating the marked influence of surfactant in the jetting behavior observed for binary droplet systems, the initial diameters of the two merging droplets were modulated by increasing the initial diameter of the leftmost droplet to 2.2 mm and decreasing the initial diameter of the rightmost droplet to 1.0 mm. Figure 5-6a shows that for asymmetrically sized droplets, both free of any added surfactant and of approximately equal interfacial tension, droplet merging led to only slight jetting of the fluid within the smaller diameter, surfactant-free droplet into the larger droplet as a direct result of the relatively small capillary pressure gradient

( $\Delta P_2/\Delta P_1 \approx 2$ ) originating from the difference in initial droplet sizes. However, the magnitude of the capillary pressure gradient was insufficient to induce a great deal of internal mixing.

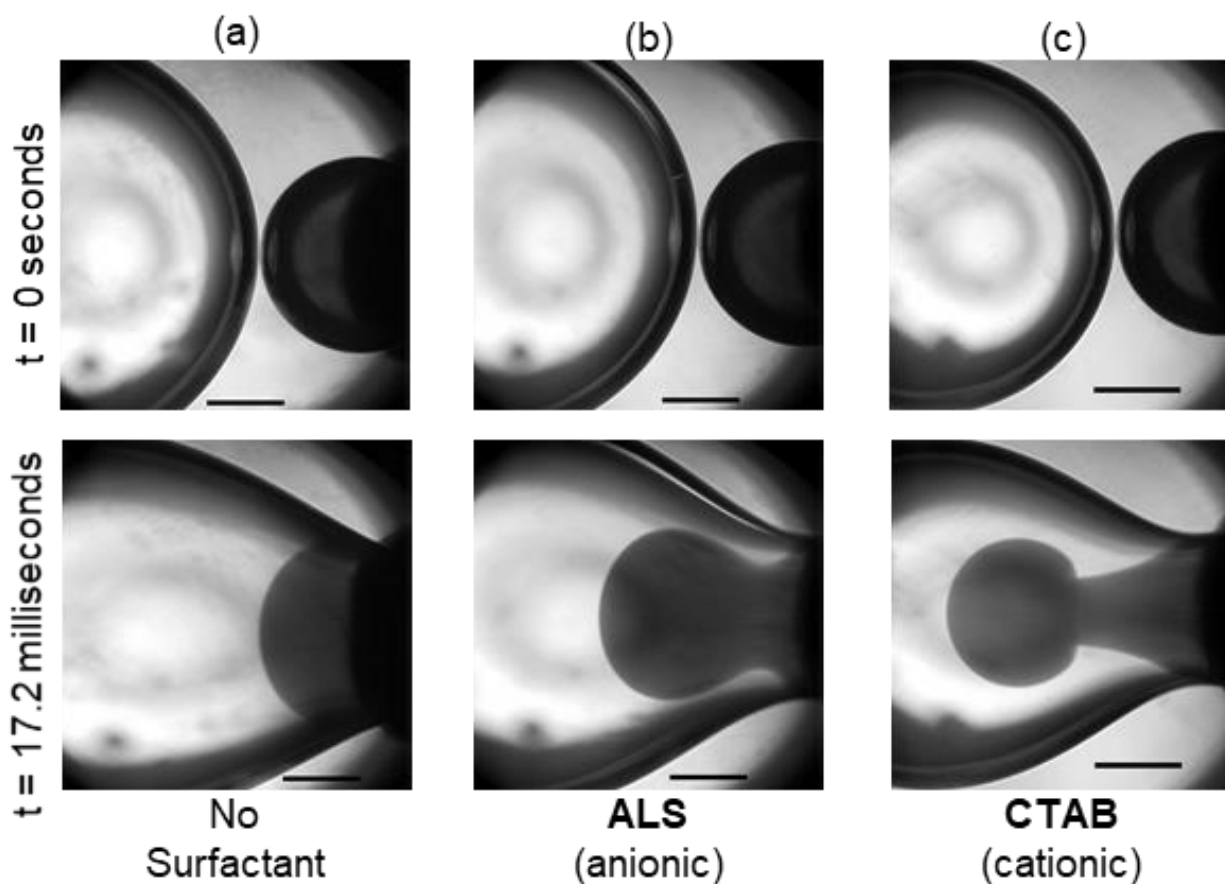


**Figure 5-6** Flow profiles depicting the formation of fluid jets of different sizes for asymmetrically sized water droplets coalescing in triglyceride oil. The leftmost droplet in each image contained either (a) no surfactant, (b)  $2.5 \times 10^{-3} \text{ mol L}^{-1}$  ALS, or (c)  $2.5 \times 10^{-3} \text{ mol L}^{-1}$  CTAB, while the rightmost droplet in each image was surfactant-free, with dye added for flow visualization. The scale bars in each image are 0.5 mm in length.

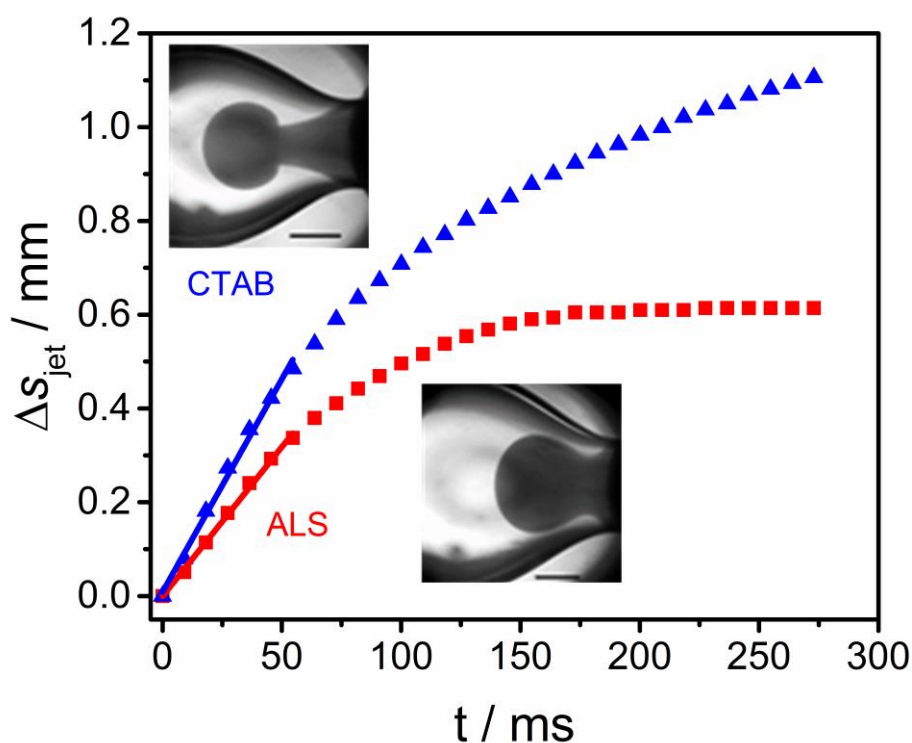
In the case of binary droplet systems that contained a concentration gradient of either ALS or CTAB, the difference in diameter and interfacial tension between the binary droplets provided a much larger capillary pressure ratio ( $\Delta P_2/\Delta P_1 \approx 11.5$ ) and thus a greater driving energy for jetting of the fluid from the smaller droplet into the larger droplet containing surfactant during coalescence. The late-stage flows that emerged under these experimental conditions are shown in

Figure 5-6b and 5-6c, respectively. For the binary droplet system with  $2.5 \times 10^{-3}$  mol L<sup>-1</sup> ALS present in the surfactant-laden droplet, the profile of the fluid jetted from the smaller, surfactant-free droplet took the shape of a bulb-like plume with a relatively large diameter forming near the apex of the jetted fluid and slightly narrower base. Similarly, for the binary droplet system containing  $2.5 \times 10^{-3}$  mol L<sup>-1</sup> CTAB, the late-stage internal flow also resulted in the formation of a fluid jet with a large bulb and narrow base. However, the jetting that occurred in this case was demonstrably stronger, with the formation of a mushroom-shaped plume of dyed water and a far narrower base.

The difference in the shape of the jetted fluid that emerged in systems containing ALS or CTAB stemmed from the magnitudes of the convective mixing generated by the opposing bulk and Marangoni interfacial flows upon droplet coalescence. As the fluid from the dyed droplet flowed through the propagating coalescence neck, an interfacial diffusional flux developed in the opposite direction, as interfacially adsorbed surfactant molecules in the surfactant-laden droplet migrated from regions of high concentration to low concentration. This in turn generated eddy currents within the bulk of the merging droplets, just beneath the interface. In the case of CTAB, the driving energy for interfacial flux appeared to be sustained for a longer time than in the case of ALS, which led to more pronounced eddy currents and thus the observed jetting behavior.

Furthermore, assessment of the displacement of the jetted fluid apex as a function of time for asymmetrically sized binary droplet systems, containing either ALS or CTAB (Figure 5-7), indicates a clear difference in the induced fluid motion. The rate of fluid jetting during the initial stages of coalescence was roughly 30% faster for the droplet system containing cationic CTAB compared to the analogous system containing anionic ALS ( $9.08 \text{ mm s}^{-1}$  and  $6.37 \text{ mm s}^{-1}$ , respectively, from a linear regression fit to the initial data in Figure 5-7). In Chapter 5.3.3, we

discuss in detail our experimental basis for attributing differences in the emerged jetting phenomena to differences in the magnitudes of the induced interfacial Marangoni flows accompanying each surfactant. The jetting phenomena observed between merging drops with an induced surfactant concentration gradient can also be explained by the induction of Marangoni convection, where low interfacial tension liquid along the oil-water interface of the coalescing neck is carried toward the higher interfacial tension regions in the surfactant-free droplet and accumulates. A localized increase in the hydrostatic pressure of this region follows and the development of a bulk flow of liquid from the surfactant-free droplet in the opposite direction of the Marangoni flow.



**Figure 5-7** Displacement of the jetted fluid apex,  $\Delta s_{\text{jet}}$ , originating from the surfactant-free droplet into the surfactant-laden droplet as a function of time,  $t$ , succeeding droplet contact for asymmetrically sized droplet systems. Micrograph insets depict the position of the fluid jets 17.2 ms after the onset of coalescence. The scale bars in each image are 0.5 mm in length.

### 5.3.3 Comparison of ALS and CTAB Adsorption at the Oil-Water Interface

Values for the surface excess concentration,  $\Gamma_m$ , in Table 5-1 indicate that CTAB molecules pack more densely at the triglyceride oil-water interface than ALS molecules, which is in line with previous experimental observations for the same or similar ionic surfactants at the oil-water interface.<sup>42,43</sup> The negatively charged moiety of 1:1 anionic surfactants leads these molecules to have a relatively large hydrodynamic diameter in comparison to cationic surfactants, which have a comparably small hydrodynamic diameter surrounding their positively charged headgroups.<sup>44</sup> These differences in the hydrodynamic volume surrounding the hydrophilic portions of each surfactant molecule lead to differences in their corresponding equilibrium adsorptive capabilities at immiscible fluid interfaces. As a direct result, anionic surfactants tend to pack less efficiently at fluid interfaces than their cationic counterparts.

Each of the experimental observations of the differences in the magnitudes of solutal Marangoni convection for ALS and CTAB would also suggest that  $\Gamma_m$  has a pivotal role in the timescale of Marangoni interfacial flow. A more densely packed interfacial layer laden with surfactant would be expected to behave more rigidly in response to interfacial tension and surfactant concentration perturbations. This rigidity restricts lateral surface movements and solutal Marangoni convection. Thus, the timescale for solutal Marangoni flow would increase, as the interface overall would take longer to relax to a homogenous state (i.e., regions of high interfacial tension and regions of low interfacial tension would exist longer for more densely packed interfaces). Under these conditions, the high interfacial tension regions would apply a high tangential surface stress over a longer duration.

Likewise, considering that both ALS and CTAB are soluble in the aqueous phase, and can therefore adsorb and desorb from the bulk aqueous phase during droplet coalescence, both the surfactant's diffusion coefficient,  $D$ , and bulk surfactant concentration,  $c$ , would be expected to

decrease the timescale of solutal Marangoni flow. A surfactant that can diffuse swiftly to the interface from the bulk would be expected to decrease the lifetime of interfacial tension gradient, (i.e., higher diffusion coefficients will favor a small concentration difference). Similarly, high concentrations of surfactant in the bulk would be expected to increase the overall adsorption rate of molecules near the interface, thus favoring small concentration gradients and reducing the timescale of solutal Marangoni convection.

The timescale of solutal Marangoni convection,  $\tau_M$ , was approximated using these parameters in the equation,  $\tau_M = \frac{\Gamma_m^2}{Dc^2}$ . Incorporating the experimentally determined saturation adsorption values from Table 5-1, a bulk surfactant concentration of  $2.5 \times 10^{-3}$  mol L<sup>-1</sup>, and diffusion coefficients of  $5 \times 10^{-10}$  m<sup>2</sup> s<sup>-1</sup> for ALS,<sup>45</sup> and  $1 \times 10^{-10}$  m<sup>2</sup> s<sup>-1</sup><sup>46</sup> for CTAB, the characteristic timescale of solutal Marangoni becomes ~0.2 ms for ALS and ~2 ms for CTAB. The order of magnitude difference in  $\tau_M$  implies that the time required for interfacially adsorbed ALS molecules to respond and dampen interfacial tension fluctuation is far faster than that of CTAB molecules.

Regarding the flows observed in the coalescence of binary droplets with asymmetric compositions, the differences in interfacial motion between surfactants can be directly attributed to the magnitudes of the surfactant molecule's corresponding  $\tau_M$  values. The timescale of solutal Marangoni convection is shorter than the characteristic coalescence timescale for two water droplets of equal diameters and interfacial tensions in the inertial regime for ALS (i.e.,  $\tau_M < \tau_C$ ). The driving energy for solutal Marangoni-driven convection is therefore relatively low because interfacial relaxation toward a homogenous interfacial tension along the coalescing bridge occurs faster than the time required for droplets to completely merge. In contrast, these timescales are very close in magnitude for systems containing CTAB (i.e.,  $\tau_M \approx \tau_C$ ). Thus, for CTAB molecules,

relaxation toward homogenous interfacial tension takes much longer and is on the order of the time required for droplets to merge, which leads to the development of strong Marangoni-driven convection and competing bulk and interfacial flows.

### 5.3.4 Surfactant Interfacial Spreading Under an Induced Concentration Gradient

Figure 5-8 shows the distance tracer particles travel as a function of time at the (initially) pure triglyceride oil-water interface following the introduction of a  $2.5 \times 10^{-3} \text{ mol L}^{-1}$  aqueous droplet solution of either anionic ALS or cationic CTAB. These data represent the fully-developed motion of the particles, starting 6.5 ms after the introduction of surfactant into the pure oil-water interface.

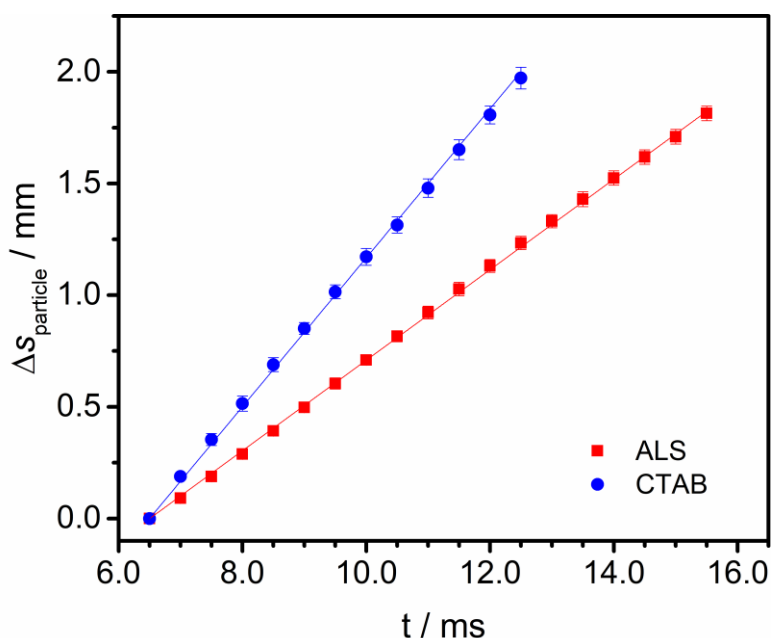


**Figure 5-8** Seeded tracer particle displacement,  $\Delta S_{\text{particle}}$ , versus time,  $t$ , following the introduction of a  $2.5 \times 10^{-3} \text{ mol L}^{-1}$  aqueous droplet solution of anionic ALS or cationic CTAB surfactant at a planar triglyceride oil-water interface. Motion of the interfacially seeded tracer particles resulted directly from the induced surfactant concentration gradient of either ALS or CTAB. Data are shown for fully developed particle displacement rates, 6.5 milliseconds after initial contact between the surfactant-laden drop and the planar oil water interface.

These data show a clear difference in the steady-state spreading velocities,  $U_s$ , of seeded glass spheres under the induced concentration gradient (i.e. for ALS:  $U_s = 0.202 \text{ m s}^{-1}$ ; for CTAB,  $U_s = 0.333 \text{ m s}^{-1}$ ) which implies that the surface motion driven by unbalanced interfacial tensions in the presence of cationic CTAB molecules exceeds that of ALS molecules. Taking the initial droplet diameter,  $2R$  ( $= 2 \text{ mm}$ ), as the characteristic length scale, an estimation of the characteristic timescale for the oil-water interface to deform under the induced surfactant concentration gradient can be obtained from  $\tau_D = 2R/U_s$ . Approximations of  $\tau_D$  yield 10 ms for ALS, and 6 ms for CTAB. These calculations for the characteristic timescales of interfacial deformation under and induced surfactant concentration gradient provide additional evidence that ALS molecules express a lower driving energy for solutal Marangoni-driven convection in comparison to CTAB molecules. As the driving energy for solutal Marangoni convection is lower for ALS, the overall motion of solutes attached to an oil-water interface when subjected to a concentration gradient would be expected to be influenced less by gradients in surfactant concentration because such gradients are short-lived.

The primary difference between the between measuring the interfacial spreading properties that develop in a droplet-planar coalescence system as opposed to a droplet-droplet system is the direction of the generated bulk flow between the aqueous droplet and planar water reservoir upon coalescence. In the case of the droplet-planar interface arrangement, the capillary pressure ratio,  $\Delta P_2/\Delta P_1$  (where  $\Delta P_1$  and  $\Delta P_2$  are the capillary pressures for the surfactant-laden droplet and planar water reservoir, respectively), would approach zero because of the approximately infinite radius of curvature of the planar water reservoir. This would in turn produce a driving energy for bulk fluid motion to propagate from the surfactant-laden droplet into the surfactant-free, planar reservoir. This bulk fluid behavior stands in contrast to the bulk flows observed and quantified in Chapter 5.3.3, where bulk fluid motion was driven from the surfactant-free droplet into the

surfactant-laden droplet due to the capillary pressure gradient. However, Marangoni-induced interfacial flows always act in the direction of the interfacial solute concentration gradient<sup>19</sup> and occur on a shorter timescale than bulk flows. Thus, the measured values for the interfacial spreading velocities (i.e. the Marangoni-induced interfacial flowrates) would presumably be minimally influenced by the experimental arrangement.

It is worth noting once again that this difference in interfacial spreading was observed for two surfactants with distinct chemical architectures, which both reduced the interfacial tension of the pure triglyceride oil-water interface to approximately  $3 \text{ mN m}^{-1}$  at a high bulk concentration. The observed differences in interfacial spreading and jetting behavior during the coalescence of binary droplets with nonuniform compositional properties must be explained by additional interfacial relaxation mechanisms, which have not previously been studied in detail by the recent literature.

#### **5.4 Summary**

Direct observation of the bulk flows generated during the coalescence of binary water-in-oil droplets with non-uniform physical properties and characterization of the contributive surfactant-induced interfacial phenomenon was performed. Mechanisms responsible for the observed opposing interfacial and bulk flows between merging surfactant-laden and surfactant-free droplets were also described. Fluid jets that developed during binary droplet coalescence were a direct result of convection driven solutal Marangoni flows which generated a rapid redistribution of low interfacial tension bulk fluid around the perimeter of the high interfacial tension bulk fluid. The degree of interfacial spreading and bulk fluid redistribution was greater for cationic CTAB molecules compared to ALS molecules due to stark differences in their equilibrium adsorption

values, kinetic re-adsorptive rates during droplet coalescence, and overall tendency for expressing solutal Marangoni convection.

This work stands in contrast to work of previous researchers in that control over bulk flows during the coalescence of binary water droplets was induced entirely through optimized surfactant selection, with no need for modulation of the bulk viscosities of the outer or inner liquid phases. Our experimental results provide additional experimental confirmation that the governing power-law relationship for coalescing droplets in the inertial regime is obeyed in the presence of an induced surfactant concentration gradient, but the prefactor in this relationship is strongly dependent upon the interfacial properties of the added surfactant.

The analyses and relationships outlined in this work can be generalized for many different surfactant types, including anionic or cationic surfactants with longer alkyl chains than those investigated here, nonionic surfactants with various alkyl tail lengths, and zwitterionic surfactants. The parameters which are expected to shorten the timescale of solutal Marangoni-convection (while decreasing its driving energy) include the surfactant's diffusion coefficient and bulk concentration, while equilibrium interfacial saturation adsorption is the primary contributor in extending the timescale of solutal Marangoni convection. Thus, enhancing the bulk mixing of binary drops with an induced concentration gradient can be done by selecting a surfactant that packs densely at the immiscible fluid interface and adsorbs to the interface strongly. Zwitterionic and polymeric surfactant would likely be ideal candidates for such applications due to their relatively small diffusion coefficients and dense interfacial organization capabilities.<sup>47</sup>

One of the most advantageous applications of using the controlled coalescence of droplets with asymmetric properties is in the synthesis of functional nanoparticles. Recently, Frenz et al.<sup>27</sup> demonstrated that magnetic iron oxide nanoparticles could be precipitated in a highly reproducible

reaction following the fusion of droplet pairs consisting of different reagents in a hydrodynamically coupled, single-nozzle microfluidic device. Controlled pairwise mixing of aqueous droplets in oil was produced by electrocoalescence<sup>48</sup> and the droplets were prevented from fusing prematurely by using a uniformly distributed surfactant at the interfaces of both droplets. The methodology developed by these researchers could be readily adapted to incorporate the findings of the present manuscript by isolating the surfactant to one of the inlet droplet flows, while leaving the other surfactant-free. Upon merging, Marangoni-induced flows would produce pronounced bulk mixing between the drops, like those explored here. Moreover, enhanced control over the degree of mixing obtained between the drops at different timescales could be explored with the previously discussed surfactant selection criteria.

In this study, we proposed a simple, yet robust experimental methodology for directly quantifying the solutal Marangoni timescales of surface-active compounds at the oil-water interface under an induced concentration gradient. With this method, the spreading efficiencies and encouragement of bulk fluid mixing for potentially any surfactant type at the oil water interface can be economically measured. The insights garnered from this work provide a compelling alternative route for inducing bulk flows in microfluidic devices without the need for modulating bulk phase viscosities.

## 5.5 References

- (1) Paulsen, J. D. Approach and Coalescence of Liquid Drops in Air. *Phys. Rev. E - Stat. Nonlinear, Soft Matter Phys.* **2013**, *88* (6), 1–13. <https://doi.org/10.1103/PhysRevE.88.063010>.
- (2) Qian, J.; Law, C. K. Regimes of Coalescence and Separation in Droplet Collision. *J. Fluid Mech.* **1997**, *331*, 59–80.
- (3) Paulsen, J. D.; Carmigniani, R.; Kannan, A.; Burton, J. C.; Nagel, S. R. Coalescence of Bubbles and Drops in an Outer Fluid. *Nat. Commun.* **2014**, *5*, 3182. <https://doi.org/10.1038/ncomms4182>.
- (4) Eggers, J.; Lister, J. R.; Stone, H. A. Coalescence of Liquid Drops. *J. Fluid Mech.* **1999**, *401*, 293–310. <https://doi.org/10.1017/S002211209900662X>.
- (5) Duchemin, L.; Eggers, J.; Josserand, C. Inviscid Coalescence of Drops. *J. Fluid Mech.* **2003**, *487* (487), 167–178. <https://doi.org/10.1017/S0022112003004646>.
- (6) Wasan, D. T. The Role of Coalescence Phenomena and Interfacial Rheological Properties in Enhanced Oil Recovery: An Overview. *J. Rheol. (N. Y. N. Y.)* **1979**, *23* (2), 181. <https://doi.org/10.1122/1.549524>.
- (7) Tcholakova, S.; Denkov, N. D.; Banner, T. Role of Surfactant Type and Concentration for the Mean Drop Size during Emulsification in Turbulent Flow. *Langmuir* **2004**, *20* (18), 7444–7458. <https://doi.org/10.1021/la049335a>.
- (8) Huebner, A. M.; Abell, C.; Huck, W. T. S.; Baroud, C. N.; Hollfelder, F. Monitoring a Reaction at Submillisecond Resolution in Picoliter Volumes. *Anal. Chem.* **2011**, *83* (4), 1462–1468. <https://doi.org/10.1021/ac103234a>.
- (9) Kim, J. H.; Jeon, T. Y.; Choi, T. M.; Shim, T. S.; Kim, S. H.; Yang, S. M. Droplet Microfluidics for Producing Functional Microparticles. *Langmuir* **2014**, *30* (6), 1473–1488. <https://doi.org/10.1021/la403220p>.
- (10) Pawar, A. B.; Caggioni, M.; Ergun, R.; Hartel, R. W.; Spicer, P. T. Arrested Coalescence in Pickering Emulsions. *Soft Matter* **2011**, *7* (17), 7710. <https://doi.org/10.1039/c1sm05457k>.
- (11) Dahiya, P.; Caggioni, M.; Spicer, P. T. Arrested Coalescence of Viscoelastic Droplets: Polydisperse Doublets. *Philos. Trans. R. Soc. A Math. Phys. Eng. Sci.* **2016**, *374* (2072), 1–13. <https://doi.org/10.1098/rsta.2015.0132>.
- (12) Ward, K.; Fan, Z. H. Mixing in Microfluidic Devices and Enhancement Methods. *J. Micromechanics Microengineering* **2015**, *25* (9), 094001. <https://doi.org/10.1088/0960-1317/25/9/094001>.

- (13) Tofteberg, T.; Skolimowski, M.; Andreassen, E.; Geschke, O. A Novel Passive Micromixer: Lamination in a Planar Channel System. *Microfluid. Nanofluidics* **2010**, *8* (2), 209–215. <https://doi.org/10.1007/s10404-009-0456-z>.
- (14) Johnson, T. J.; Ross, D.; Locascio, L. E. Rapid Microfluidic Mixing. *Anal. Chem.* **2002**, *74* (1), 45–51. <https://doi.org/10.1021/ac010895d>.
- (15) Krebs, T.; Schroën, C. G. P. H.; Boom, R. M. Coalescence Kinetics of Oil-in-Water Emulsions Studied with Microfluidics. *Fuel* **2013**, *106*, 327–334. <https://doi.org/10.1016/j.fuel.2012.10.067>.
- (16) Arbor, A.; Tryggvason, G. The Flow Induced by the Coalescence of Two Initially Stationary Drops. *Nasa Tech. Memo.* **1994**, No. October 1994.
- (17) Nowak, E.; Kovalchuk, N. M.; Che, Z.; Simmons, M. J. H. Effect of Surfactant Concentration and Viscosity of Outer Phase during the Coalescence of a Surfactant-Laden Drop with a Surfactant-Free Drop. *Colloids Surfaces A Physicochem. Eng. Asp.* **2016**, *505*, 124–131. <https://doi.org/10.1016/j.colsurfa.2016.02.016>.
- (18) Nowak, E.; Xie, Z.; Kovalchuk, N. M.; Matar, O. K.; Simmons, M. J. H. Bulk Advection and Interfacial Flows in the Binary Coalescence of Surfactant-Laden and Surfactant-Free Drops. *Soft Matter* **2017**, *13* (26), 4616–4628. <https://doi.org/10.1039/C7SM00328E>.
- (19) Sternling, C. V.; Scriven, L. E. Interfacial Turbulence: Hydrodynamic Instability and the Marangoni Effect. *AIChE J.* **1959**, *5* (4), 514–523. <https://doi.org/10.1002/aic.690050421>.
- (20) Scriven, L. E.; Sternling, C. V. The Marangoni Effects. *Nature* **1960**, *187* (4733), 186–188. <https://doi.org/10.1038/187186a0>.
- (21) Wasan, D. T. Destabilization of Water-in-Oil Emulsions. In *Emulsions - A Fundamental and Practical Approach*; 1992; pp 283–295.
- (22) Saad Bhamla, M.; Chai, C.; Álvarez-Valenzuela, M. A.; Tajuelo, J.; Fuller, G. G. Interfacial Mechanisms for Stability of Surfactant-Laden Films. *PLoS One* **2017**, *12* (5), 1–14. <https://doi.org/10.1371/journal.pone.0175753>.
- (23) Szymczyk, K.; Jańczuk, B. The Adsorption at Solution-Air Interface and Volumetric Properties of Mixtures of Cationic and Nonionic Surfactants. *Colloids Surfaces A Physicochem. Eng. Asp.* **2007**, *293* (1–3), 39–50. <https://doi.org/10.1016/j.colsurfa.2006.07.006>.
- (24) Jańczuk, B.; Zdziennicka, A.; Wójcik, W. The Properties of Mixtures of Two Anionic Surfactants in Water at the Water | Air Interface. *Colloids Surfaces A Physicochem. Eng. Asp.* **2003**, *220* (1–3), 61–68. [https://doi.org/10.1016/S0927-7757\(03\)00060-8](https://doi.org/10.1016/S0927-7757(03)00060-8).
- (25) Hudson, S. D.; Jamieson, A. M.; Burkhart, B. E. The Effect of Surfactant on the Efficiency of Shear-Induced Drop Coalescence. *J. Colloid Interface Sci.* **2003**, *265* (2), 409–421. [https://doi.org/10.1016/S0021-9797\(03\)00396-5](https://doi.org/10.1016/S0021-9797(03)00396-5).

- (26) Weheliye, W. H.; Dong, T.; Angeli, P. On the Effect of Surfactants on Drop Coalescence at Liquid/Liquid Interfaces. *Chem. Eng. Sci.* **2017**, *161*, 215–227. <https://doi.org/10.1016/j.ces.2016.12.009>.
- (27) Frenz, L.; El Harrak, A.; Pauly, M.; Bégin-Colin, S.; Griffiths, A. D.; Baret, J. C. Droplet-Based Microreactors for the Synthesis of Magnetic Iron Oxide Nanoparticles. *Angew. Chemie - Int. Ed.* **2008**, *47* (36), 6817–6820. <https://doi.org/10.1002/anie.200801360>.
- (28) Diamant, H.; Andelman, D. Kinetics of Surfactant Adsorption at Fluid-Fluid Interfaces. *J. Phys. Chem.* **1996**, *100* (32), 13732–13742. <https://doi.org/10.1021/jp960377k>.
- (29) Eliceiri, K.; Schneider, C. A.; Rasband, W. S.; Eliceiri, K. W. NIH Image to ImageJ : 25 Years of Image Analysis. *Nat. Methods* **2012**, *9* (7), 671–675. <https://doi.org/10.1038/nmeth.2089>.
- (30) Evans, D. F.; Wennerström, H. *The Colloidal Domain: Where Physics, Chemistry, Biology, and Technology Meet*, 2nd ed.; 1999.
- (31) Nash, J. J.; Erk, K. A. Stability and Interfacial Viscoelasticity of Oil-Water Nanoemulsions Stabilized by Soy Lecithin and Tween 20 for the Encapsulation of Bioactive Carvacrol. *Colloids Surfaces A Physicochem. Eng. Asp.* **2017**, *517*, 1–11. <https://doi.org/10.1016/j.colsurfa.2016.12.056>.
- (32) Berry, J. D.; Neeson, M. J.; Dagastine, R. R.; Chan, D. Y. C.; Tabor, R. F. Measurement of Surface and Interfacial Tension Using Pendant Drop Tensiometry. *J. Colloid Interface Sci.* **2015**, *454*, 226–237. <https://doi.org/10.1016/j.jcis.2015.05.012>.
- (33) Loglio, G.; Pandolfini, P.; Miller, R.; Makievski, A. V.; Ravera, F.; Ferrari, M.; Liggieri, L. Drop and Bubble Shape Analysis as a Tool for Dilational Rheological Studies of Interfacial Layers. In *Novel Methods to Study Interfacial Layers*; Möbius, D., Miller, R., Eds.; Elsevier, 2001; Vol. 11, pp 439–483. [https://doi.org/10.1016/S1383-7303\(01\)80038-7](https://doi.org/10.1016/S1383-7303(01)80038-7).
- (34) Kang, K. H.; Kim, H. U.; Lim, K. H. Effect of Temperature on Critical Micelle Concentration and Thermodynamic Potentials of Micellization of Anionic Ammonium Dodecyl Sulfate and Cationic Octadecyl Trimethyl Ammonium Chloride. *Colloids Surfaces A Physicochem. Eng. Asp.* **2001**, *189* (1–3), 113–121. [https://doi.org/10.1016/S0927-7757\(01\)00577-5](https://doi.org/10.1016/S0927-7757(01)00577-5).
- (35) Mosquera, V.; Del Río, J. M.; Attwood, D.; García, M.; Jones, M. N.; Prieto, G.; Suarez, M. J.; Sarmiento, F. A Study of the Aggregation Behavior of Hexyltrimethylammonium Bromide in Aqueous Solution. *J. Colloid Interface Sci.* **1998**, *206* (1), 66–76. <https://doi.org/10.1006/jcis.1998.5708>.
- (36) Movchan, T. G.; Rusanov, A. I.; Soboleva, I. V.; Khlebunova, N. R.; Plotnikova, E. V.; Shchekin, A. K. Diffusion Coefficients of Ionic Surfactants. *Colloid J.* **2015**, *77* (4), 492–499. <https://doi.org/10.1134/S1061933X15040146>.

- (37) Rosen, M. J. *Surfactants and Interfacial Phenomena, 3rd Ed.*; John Wiley & Sons, Inc., 2004.
- (38) Eastoe, J.; Nave, S.; Downer, A.; Paul, A.; Rankin, A.; Penfold, J. Adsorption of Ionic Surfactants at the Air - Solution Interface. *Langmuir* **2000**, *16* (25), 4511–4518. <https://doi.org/10.1021/la991564n>.
- (39) Park, B. J.; Pantina, J.; Furst, E. M.; Oettel, M.; Reynaert, S. Direct Measurements of the Effects of Salt and Surfactant on Interaction Forces between Colloidal Particles at Water–Oil Interfaces. *Langmuir* **2008**, *24* (17), 1686–1694. <https://doi.org/10.1021/la7008804>.
- (40) Binks, B. P. Particles as Surfactants - Similarities and Differences. *Curr. Opin. Colloid Interface Sci.* **2002**, *7* (1–2), 21–41. [https://doi.org/10.1016/S1359-0294\(02\)00008-0](https://doi.org/10.1016/S1359-0294(02)00008-0).
- (41) Wu, M.; Cubaud, T.; Ho, C. Scaling Law in Liquid Drop Coalescence Driven by Surface Tension. *Phys. Fluids* **2004**, *16* (7), 51–54. <https://doi.org/10.1063/1.1756928>.
- (42) Rehfeld, S. J. Adsorption of Sodium Dodecyl Sulfate at Various Hydrocarbon-Water Interfaces. *J. Phys. Chem.* **1967**, *71*, 738–745. <https://doi.org/10.1021/j100862a039>.
- (43) Fainerman, V. B.; Aksenenko, E. V.; Mucic, N.; Javadi, A.; Miller, R. Thermodynamics of Adsorption of Ionic Surfactants at Water/Alkane Interfaces. *Soft Matter* **2014**, *10* (36), 6873–6887. <https://doi.org/10.1039/C4SM00463A>.
- (44) Prins, A.; Arcuri, C.; Van den Tempel, M. Elasticity of Thin Liquid Films. *J. Colloid Interface Sci.* **1967**, *24*, 84–90. [https://doi.org/10.1016/0021-9797\(67\)90281-0](https://doi.org/10.1016/0021-9797(67)90281-0).
- (45) Javadi, A.; Mucic, N.; Vollhardt, D.; Fainerman, V. B.; Miller, R. Effects of Dodecanol on the Adsorption Kinetics of SDS at the Water–hexane Interface. *J. Colloid Interface Sci.* **2010**, *351*, 537–541. <https://doi.org/10.1016/j.jcis.2010.07.033>.
- (46) Stubenrauch, C.; Fainerman, V. B.; Aksenenko, E. V.; Miller, R. Adsorption Behavior and Dilational Rheology of the Cationic Alkyl Trimethylammonium Bromides at the Water/Air Interface. *J. Phys. Chem. B* **2005**, *109* (4), 1505–1509. <https://doi.org/10.1021/jp0465251>.
- (47) Seredyuk, V.; Alami, E.; Nydén, M.; Holmberg, K.; Peresykin, A. V.; Menger, F. M. Adsorption of Zwitterionic Gemini Surfactants at the Air-Water and Solid-Water Interfaces. *Colloids Surfaces A Physicochem. Eng. Asp.* **2002**, *203* (1–3), 245–258. [https://doi.org/10.1016/S0927-7757\(01\)01106-2](https://doi.org/10.1016/S0927-7757(01)01106-2).
- (48) Ahn, K.; Agresti, J.; Chong, H.; Marquez, M.; Weitz, D. A. Electrocoalescence of Drops Synchronized by Size-Dependent Flow in Microfluidic Channels. *Appl. Phys. Lett.* **2006**, *88* (26). <https://doi.org/10.1063/1.2218058>.

## CHAPTER 6 CONCLUSIONS

### 6.1 Summary of Projects

The two main objectives of this thesis were to (1) elucidate fundamental relationships between the mechanics of complex fluid interfaces and the anticipated stability of bulk emulsions they comprise through interfacial rheological measurements, and (2) to present innovative methodologies for modulating the kinetic stability of model oil-in-water emulsions via physical chemistry principles.

The first two projects of this work provided experimental evidence toward addressing Objective (1). The first project in this thesis focused on how interfacial rheology influences an oil-in-water emulsion's susceptibility to coalescence and, by extension, its extended kinetic stability. This analysis was carried out by measuring the dilatational rheology of conventional oil-in-water nanoemulsions stabilized by one of two emulsifiers; one of which displayed highly viscoelastic interfacial characteristics and one that did not. The results of this study illustrated that greater dilatational viscoelasticity positively correlates to a nanoemulsion's resistance to coalescence. This correlation was demonstrated by dynamic light scattering measurements which revealed smaller increases in the average droplet diameter and size distribution of dispersed oil droplets over time for systems with highly viscoelastic interfaces (i.e., those stabilized by lecithin).

The second project in this thesis built upon the premise that enhanced dilatational viscoelasticity contributes to an emulsion's resistance to destabilization via coalescence. In this study, oil-in-water Pickering emulsions stabilized by SiO<sub>2</sub>-surfactant complexes were created. The interfacial mechanics of the SiO<sub>2</sub>-surfactant complexes were compared to the those of both the SiO<sub>2</sub> and surfactant alone. The SiO<sub>2</sub>-surfactant complexes were shown to have a synergistic effect on the magnitude of the dilatational viscoelasticity of the multicomponent oil-water interface.

Moreover, the dilatational elastic modulus for uncompressed SiO<sub>2</sub>-DPPC surfactant complexes ( $\sim 50 \text{ mN m}^{-1}$ ) was also an order of magnitude higher than previous observations. The increase in interfacial viscoelasticity provided by the SiO<sub>2</sub>-surfactant complexes at the oil-water interface was positively correlated to the coalescence resistance of the dispersed oil droplets within the emulsion.

The last two projects of this work provided experimental evidence toward addressing Objective (2). The third project utilized a complex coacervation mechanism to neutralize the surface charge of electrostatically stabilized oil droplets and induce rapid oil-water phase separation. Negatively-charged oil droplets stabilized by one of the most common industrial surfactants, SLES, were made to flocculate and gravitationally phase separate by positively-charged SiO<sub>2</sub> nanoparticles. A simple mass balance was developed which enabled the prediction of the required charged-nanoparticle concentration necessary be added to an electrostatically-stabilized emulsion to produce the desired destabilization effects.

The forth project of this thesis demonstrated how coalescence could be used to produce tightly controlled internal mixing between two merging droplets. It was found that asymmetric surfactant concentrations within the merging droplets produced pronounced fluid jets that propagated from the droplet of higher capillary pressure into the droplet of lower capillary pressure. Moreover, it was found that the rate of displacement for the jetted fluid could be modulated through appropriate surfactant selection. Surfactants with different headgroup architectures (i.e., anionic versus cationic) were found to produce different jetting rates due to differences in their adsorptive and interfacial dilatational rheological characteristics.

## 6.2 Future Work and Outlook

The relationship between interfacial rheology and coalescence was studied extensively in Chapter 2 and Chapter 3, with some suggestions toward its role in inhibiting other destabilization

mechanisms (e.g., Ostwald ripening). Future work on this topic could focus on how interfacial viscoelasticity influences the dissolution rates of partially water-soluble lipophilic compounds encapsulated within oil-in-water emulsions. Dissolution rates could be probed experimentally using dynamic light scattering, visual observation, optical microscopy, and differential scanning calorimetry methods.

Gravitational phase separation of dilute, electrostatically stabilized emulsions by a charge neutralization and flocculation mechanism was the emphasis of Chapter 4. Future work on this topic could focus on how different particulate chemistries can produce the same rapid phase separation behavior observed in this study. Specifically, polymer latexes may act as a suitable alternative to SiO<sub>2</sub> nanoparticles due to their inexpensive fabrication, ease of surface chemistry modification, and closely matched density ( $\sim 1.1 \text{ g cm}^{-3}$ ) to that of water. Each of these characteristics make these materials worthy of further investigation in oil-in-water emulsion destabilization studies.

In conclusion, interfacial rheology has been shown to be an invaluable characterization tool in predicting the stabilization behavior oil-in-water emulsions. The connection between interfacial dilatational rheology and bulk emulsion stability remains elusive. However, this body of work further elucidates its intimate connection with the susceptibility to coalescence of dispersed oil droplets.

## VITA

Jerome Nash is from Indianapolis, IN. He graduated with his Bachelor of Science in Materials Science and Engineering from Purdue University in 2015. As a graduate student, his research interests included investigations related to the development of nanoscale therapeutic delivery systems, colloidal phenomena, and probing the mechanical behavior of multi-component fluid-fluid interfaces. Jerome's honors include the NSF East Asia and Pacific Summer Institutes (EAPSI) Fellowship, the Bilsland Dissertation Fellowship, and the Estus H. and Vashti L. Magoon Award for Excellence in Teaching. Jerome was a Purdue Alliance for Graduate Education and the Professoriate (AGEP) Scholar, an active member of the Purdue Chapter of the National Society of Black Engineers (NSBE), and a dedicated mentor for graduate and undergraduate students from historically underrepresented backgrounds in STEM disciplines. During his time at Purdue, Jerome was also actively involved in community STEM outreach efforts, through his roles as a teaching assistant for the Purdue EPICS Program and through his role as the Purdue MSE Graduate Student Association Outreach Chair from August 2015 – August 2016.